# Development of a Microfabricated Turbine-Driven Air Bearing Rig

by

Chuang-Chia Lin

**B.S., National Taiwan University (1990)**
**S.M., Massachusetts Institute of Technology (1995)**

Submitted to the Department of Mechanical Engineering
in Partial Fulfillment of the Requirements For the Degree Of

**DOCTOR OF PHILOSOPHY**

at the

**MASSACHUSETTS INSTITUTE OF TECHNOLOGY**

June 1999

© Massachusetts Institute of Technology 1999. All rights reserved.

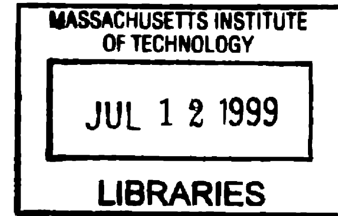


Author.......................................................................................
Department of Mechanical Engineering
April 15, 1999

Certified by.......................................................................................
Martin A. Schmidt
Professor, Department of Electrical Engineering and Computer Science
Thesis Supervisor

Certified by.......................................................................................
Ain A Sonin
Professor, Department of Mechanical Engineering
Committee Chairman

Accepted by.......................................................................................
Ain A. Sonin
Chairman, Department Committee on Graduate Students

# Development of a Microfabricated Turbine-Driven Air Bearing Rig

by

Chuang-Chia Lin

Submitted to the Department of Electrical Engineering and Computer Science on April 15, 1999, in Partial Fulfillment of the Requirement for the Degree of Doctor of Philosophy

## ABSTRACT

A team at MIT has been working to develop the technology for a micro gas turbine generator that is capable of converting chemical energy from fuel into electrical power. Such a MEMS device would represent a big leap in portable power source technology, providing ten times the power and energy density of batteries at competitive costs.

The major fabrication challenge of realizing this miniature gas turbine generator is to demonstrate a baseline fabrication process capable of integrating the radial-inflow turbine rotor, bearings, and gas interconnects into a small package. The rotor is a 300 μm thick, 4 millimeter diameter disk supported by a nominally 10 μm wide air journal bearing. This structure, called the micro-bearing rig, is not only a vehicle for the development of a process methodology for fabrication of freely-rotating high aspect ratio devices, but it is also a vehicle for research into micro-fabricated gas bearings and rotordynamics. The process flow involves the use of 16 masks, 9 aligned deep reactive ion etching (DRIE) steps, aligned fusion bonding of a 5 wafer stack, and laser assisted etching. The device has been successfully fabricated, and the fabrication process will be presented, together with work in instrumentation, and packaging.

In order to determine the necessary tolerances for the micro bearing fabrication and to provide performance parameters, calculations were performed based on a computational fluid dynamics and a semi-empirical model. The calculations are validated through comparison to the experimental measurements. Based on the model, improvements in thrust bearing design are implemented and fabricated. The increasing fabrication accuracy is reflected by constant improvement in device performance. So far, a stable speed of 296,000 rpm has been achieved.

The approach taken to develop the fabrication process flow described can be applied in many areas to build devices with complicated micro-fluidic interconnects and devices with encapsulated free-moving parts. Data from the micro-thrust bearings are useful for miniature fluidic/hydraulic actuators. The micro-rotating machinery will open new opportunities for fabricating micro valves, pumps, micro-coolers, and micro-propulsion devices.

Thesis Supervisor: Martin A. Schmidt
Title: Professor, Department of Electrical Engineering and Computer Science

## *Acknowledgements*

For years I have been dreaming about writing this paragraph....and the day has finally arrived.

The journey towards a Ph.D. is not a short one, and it has not been easy. The six and half years I've lived at MIT will have a significant impact on me for the rest of my life. In this time, I have been fortunate to meet many brilliant people who have inspired me to keep working harder. I have also taken many great courses that have elevated my scientific knowledge to a higher level.

In my Ph.D. work, I have been extremely privileged to have Prof. Martin Schmidt as my thesis advisor. For a person who is seeking a boss who can also be his friend, Marty is the perfect advisor. Although I have not yet found any professor who is busier than him, he always allocates time to listen to his students when there is a need. Frankly, we have very different personalities; however, I feel that I could tell him anything, and he is willing to share with me his insight on many things even if there is a conflict of interest. As a foreign student working here alone, I really appreciate that input.

Working on a huge project like the micro engine project, I have had a rare opportunity to work with many professors directly and learn from their different styles. Professor Alan Epstein, besides being very sharp and often providing a different perspective on things, is a great manager who has successfully guided the whole project. Professor Kenneth Breuer is very careful about details and is also creative. I will always be grateful to Professor Senturia, who helped me get in the project and with many other requests. Professor Lang taught a great course on eletromechanics to me and has been very kind to me since our first meeting. I also appreciate Professor Lallit Anand, my masters thesis advisor, for giving me a solid training on the fundamentals. I would also like to thank Prof. Ain Sonin for giving me guidance when I was occasionally confused in this journey, and for his kindness of agreeing to chair my committee. I am grateful for sponsorship from the Army Research Office MURI grant (DAAH04-95-1-0093), and the director Dr. Richard Paur.

I also have had the benefit of having an excellent group of people working with me. Dr. Arturo Ayon has had a big impact on my thesis in assisting with the ICP and bonder operations. Both Dr. Reza Ghodssi and Dr. Ravi Khanna have helped me with the device fabrication. Dye-Zone Chen and Dr. Ted Bloomstein has helped me with the laser etching. Dr. Stuart Jacobson, one of

the most important people in both the microengine project and my micro bearing rig project, has helped me tremendously in the fluidic modeling and testing. Dr. Steve Umans helped me with the speed sensor circuits. Dr. Fredric Ehrich helped me design the testing system, and showed me the working spirit. And Victor Dubrowski and James Letendre have done great jobs in assisting me with the hardware machining. Holly Anderson has helped me with many purchasing issues. Interactions with other people in the micro engine project have also sparked many ideas, and I am very grateful.

For years at MIT, I shared my happiness and sorrow with my former girlfriend, Liping Li. Although things did not work out, I sincerely hope that she found a great guy and has a wonderful family for the rest of her life.

The Schmidt Group has also treated me nicely. For the ones not in the microengine project: Dr. Lalitha Parameswaran was my mentor for the micro fabrication. She taught me many things when I joined the group and was a great listener when I was down. Joey Wong was my high school classmate, and he gave me the information about the microengine project so that I had a chance to join. Without him and my other ROCSA friends such as Kuo-Chiang Chen Kuo-Chun Wu, and Kwan-Han Chen, my life at MIT would be really just working and unbearable. Samara Firebaugh and Rebecca Braff, my two dear officemates, are nice and caring and listen to all my troubles. Joel Voldman is the fun guy who makes a lot of noises, but always there when I need a hand. Charles Hsu, Errol Arkilic, Mark Sheplak, Chi-Fan Yung, Christine Tsao, Albert Folch, and Kei Ichihara are all friends who enriched my life at MIT.

The members of Microsystems Technology Labs have always treated my well. May Lu and Octavio Hurtado were twoof my micro-fabrication mentors. Joe Walsh, Paul Tierney, and Pat Burkhart always responded quickly to my requests. Joe DiMaria, Chi Hoang, Brian Foley, Dan Adams and all others are friends never hesitate to give a helping hand.

My fiancée, Shen-Hsiu, have filled me with encouragement and love with her countless phone calls, faxes, and emails. I will forever remember her company in these tough final hours in Cambridge, sharing my pain and helping me keep my sanity. Last, I'd like to thank my father, my mother, and my sisters, who are always there for me unconditionally. Just like they would do for me, I would do anything to assure that they have good health and happy lives, and tell them, " I love you very very much."

# Contents

**CHAPTER 1 INTRODUCTION** ..... **19**

SECTION 1.1 MOTIVATION AND OVERVIEW ..... 19

SECTION 1.2 THESIS GOALS ..... 22

SECTION 1.3 THESIS LAYOUT ..... 23

SECTION 1.4 REFERENCE ..... 23

**CHAPTER 2 MICRO BEARING RIG DESIGN** ..... **25**

SECTION 2.1 TURBINE DESIGN ..... 28

SECTION 2.2 THRUST BEARING DESIGN ..... 30

SECTION 2.3 JOURNAL BEARING DESIGN ..... 36

*2.3.1 Rotor tilting balance* ..... *43*

*2.3.2 Journal bearing side loading and rotor axial balance* ..... *43*

*2.3.3 Jacking ports* ..... *44*

SECTION 2.4 SUMMARY ..... 45

SECTION 2.5 REFERENCES ..... 45

**CHAPTER 3 FABRICATION PROCESS** ..... **47**

SECTION 3.1 FABRICATION PROCESS FLOW ..... 47

*3.1.1 Full wafer-level process* ..... *48*

SECTION 3.2 FABRICATION TECHNIQUES AND CHALLENGES ..... 54

*3.2.1 Deep RIE optimization:* ..... *54*

*3.2.2 Multiple wafers aligned silicon fusion bonding* ..... *70*

*3.2.3 Laser-assisted silicon etch and free-moving part fabrication* ..... *75*

SECTION 3.3 REFERENCE ..... 79

**CHAPTER 4 PACKAGING AND INSTRUMENTATION** ..... **83**

SECTION 4.1 PACKAGING ..... 83

SECTION 4.2 INSTRUMENTATION ..... 87

*4.2.1 Fluidic control/measurement system* ..... *87*

*4.2.2 Speed sensor* ..... *89*

*4.2.3 Axial position sensor* ..... *93*

SECTION 4.3 REFERENCE ..... 95

**CHAPTER 5 STATIC FLOW CHARACTERIZATION** ..... **97**

SECTION 5.1 FLUIDIC MODELING ..... 97

*5.1.1 Baseline model* ..... *98*

*5.1.2 Computational Fluid Dynamics (CFD) model* ........ *102*

SECTION 5.2 PRESSURE-FLOW CHARACTERISTICS ........ 111

SECTION 5.3 BONDING YIELD CHARACTERIZATION AND DIMENSIONAL DEDUCTION ........ 116

*5.3.1 Bonding yield characterization* ........ *116*

*5.3.2 Thrust bearing dimensional deduction* ........ *118*

*5.3.3 Journal bearing axial flow measurement* ........ *119*

SECTION 5.4 ROTOR AXIAL POSITION TEST ........ 124

SECTION 5.5 SUMMARY ........ 131

**CHAPTER 6 ROTOR SPIN TEST ........ 133**

SECTION 6.1 HYDROSTATIC AND HYDRODYNAMIC SETUP ........ 133

SECTION 6.2 HYDROSTATIC TESTING RESULTS ........ 134

SECTION 6.3 HYDRODYNAMIC TESTING RESULTS ........ 138

SECTION 6.4 SUMMARY ........ 142

SECTION 6.5 REFERENCE: ........ 143

**CHAPTER 7 CONCLUSION ........ 145**

SECTION 7.1 THESIS CONTRIBUTIONS ........ 145

SECTION 7.2 LESSONS LEARNED ........ 146

SECTION 7.3 FUTURE WORK ........ 147

**APPENDICES ........ 149**

A. PROCESS FLOW ........ 149

*Prototype process flow* ........ *149*

*Full wafer level process steps:* ........ *153*

B. PACKAGING DESIGN ........ 158

C BASELINE THRUST BEARING MODEL ........ 163

REFERENCE ........ 165

# List of Figures

FIGURE 1-1 MIT MICRO GAS TURBINE GENERATOR. IT HAS ABOUT 10 PARTS, WITH INLET DIAMETER OF 2 MILLIMETERS AND WEIGHT OF 1 GRAM WITHOUT FUEL. THE FLOW RATE IS ABOUT 0.1 GM/SEC.......... 21

FIGURE 1-2 ABB GT13 GAS TURBINE. IT HAS ABOUT 10,000 PARTS, WITH INLET DIAMETER OF 2 METERS AND WEIGHT OF 400 TONS. THE AIR FLOW RATE IS OF THE ORDER OF 500 KG/SEC AND IT PRODUCES 150 MW OF POWER. THE TYPICAL PURCHASE COST IS ABOUT $300/KW.................................................. 21

FIGURE 2-2 EXPLODED VIEW OF MICRO BEARING RIG................................................................................ 27

FIGURE 2-3 CLOSE-UP VIEW OF 2ND WAFER........................................................................................ 28

FIGURE 2-4 CROSS-SECTIONAL LAYOUT OF MICRO BEARING RIG................................................................ 28

FIGURE 2-5 MICRO TURBINE BLADES DESIGN. THE ROTOR SPINS COUNTER CLOCKWISE. ............................ 29

FIGURE 2-6 ROTOR TORQUE VS. SPEED FOR THE DESIGNED TURBINE BASED ON MISES RESULT FROM DR. S. JACOBSON. THE TORQUE IS CALCULATED BY DIVIDING THE TURBINE POWER BY THE ROTATION RATE, ASSUMING 9W OF VISCOUS DISSIPATION FROM THE BEARING AT FULL SPEED AND A QUADRATIC RELATIONSHIP BETWEEN ROTOR SPEED AND BEARING DISSIPATION.................................................... 30

FIGURE 2-7 HYDROSTATIC LUBRICATION. PRESSURE DIAGRAMS AND FLUID FILM FORMATION IN AN AXIAL SINGLE-PAD BEARING [4]. ....................................................................................................... 31

FIGURE 2-8 HYDROSTATIC OPPOSED-PAD AXIAL BEARING. .......................................................................... 32

FIGURE 2-9 (A) SPIRAL THRUST BEARING. (B) STEP PAD THRUST BEARING (FIGURE FROM REFERENCE [5]). 32

FIGURE 2-10 FLOW RATE Q (A) AND FILM THICKNESS H (B) VERSUS LOAD W FOR DIFFERENT SUPPLY SYSTEMS; 1 - CONSTANT FLOW SYSTEM; 2- CAPILLARY; 3- ORIFICE; 4- CONSTANT FLOW VALVE; 5- DIAPHRAGM-CONTROLLED RESTRICTOR; 6- INFINITE STIFFNESS (H = CONSTANT) [6]. ......................... 33

FIGURE 2-11 MICRO HYDROSTATIC THRUST BEARING DESIGN. THIS DESIGN INCORPORATES BOTH THE CAPILLARY RESTRICTION AND INHERENT RESTRICTION EFFECT FOR BEARING COMPENSATION. KEY DESIGN PARAMETERS ARE CAPILLARY DIAMETER D, LENGTH *L*, AND BEARING GAP G WHICH IS HALF OF THE TOTAL BEARING GAP BECAUSE THERE IS A PAIR OF OPPOSED BEARINGS. IN THE TEXT, VALUES FOR BEARING GAP ARE GIVEN IN TERMS OF G. ROTOR AXIAL POSITION IS TYPICALLY DEFINED AS AXIAL ECCENTRICITY, WHICH IS AXIAL DISPLACEMENT NORMALIZED BY BEARING GAP. ................................ 35

FIGURE 2-12 PLAIN HYDROSTATIC JOURNAL BEARING. THE DRAWING IS NOT TO SCALE TO HIGHLIGHT THE KEY DIMENSIONS. THE ROTOR HAS A RADIUS R AND THE BEARING RADIUS IS R. THE BEARING GAP IS C, AND BEARING IS LOADED BY W. THE STABLE POSITION IS NOT ALIGNED WITH THE LOADING BUT FORMS AN ANGLE CALLED THE ATTITUDE ANGLE φ. THE MAXIMUM DISPLACEMENT OF THE CENTER OF THE ROTOR IS E. .......................................................................................................................... 37

FIGURE 2-13 VELOCITY PROFILE OF VISCOUSLY DRAGGED FLOW THROUGH A CONVERGING CHANNEL. THE TOP PLATE IS MOVING TO THE RIGHT AT SPEED U, AND PRESSURE IS GENERATED TO SUPPORT THE MOVING PLATE [5]. ........................................................................................................................ 37

FIGURE 2-14 JOURNAL BEARING LOCATION OPTIONS. ..................................................................... 38

FIGURE 2-15 PRESSURE CONTOURS AROUND A PLAIN HYDRODYNAMIC JOURNAL BEARING WITH LOAD VARYING FROM 3 TO 61 LB. [3]. THE BEARING DIAMETER IS 2 INCH, LENGTH IS 4 INCH, AND GAP IS 0.001045 INCH. ........ 39
FIGURE 2-16 THE JOURNAL BEARING SUMP PLENUMS DESIGN. (A) THE ROTOR/EDGE JOURNAL BEARING GAP OVERLAPS WITH THE PLENUMS SUCH THE ROTOR EXPERIENCES THREE DIFFERENT AMBIENT PRESSURES. (IN PRACTICE, THE TWO HIGH SUMPS ARE USUALLY SET TO EQUAL PRESSURE.) THE THICK ARROWS SHOWS THE AXIAL CROSS FLOW PATH THAT GOES THROUGH THE JOURNAL BEARING GAP. THIS FLOW SETS UP A PRESSURE FIELD IN THE JOURNAL BEARING TO PUSH THE ROTOR SIDEWAYS, AS SHOWN IN PART (B). ........ 41
FIGURE 2-17 MINIMUM STABLE RUNNING-GAP VS. BEARING ASPECT RATIO – DERIVED FROM MAXIMUM 'MINIMUM ECCENTRICITY' CHART FROM PIEKOS [10]. THE TRADE-OFF BETWEEN BEARING ETCH, RUNNING GAP, AND BEARING LENGTH L IS CLEARLY SHOWN. THIS CHART ASSUME ROTOR DIAMETER OF 4MM. ........ 43
FIGURE 2-18 ROTOR TILT BALANCE CHANNEL AND BACK-SIDE VENT HOLES. ........ 44
FIGURE 3-1 MICRO RIG FABRICATION PROCESS. ........ 51
FIGURE 3-2 BONDED 2ND-3RD WAFER PAIRS. ........ 52
FIGURE 3-3 CLOSE-UP VIEW OF THRUST BEARING PLENUM. THRUST BEARING ORIFICES ARE ALSO SHOWN. THE DIESAWING PROCESS CHIPS THE EDGE OF THE THRUST BEARING PAD AND MAKES THE 2 μM BEARING GAP MORE VISIBLE. ........ 52
FIGURE 3-4 FABRICATED 4TH/5TH BONDED WAFER PAIR. ........ 53
FIGURE 3-5 CROSS-SECTIONAL VIEW OF MICRO BEARING RIG SHOWING THE DEPTHS MEASUREMENTS OF EACH DEEP ETCH. ........ 53
FIGURE 3-6 CROSS-SECTIONAL SEM OF MICRO BEARING RIG SHOWING THE INTERNAL FLOW PATHS. ........ 54
FIGURE 3-7 BOSCH PROCESS. ........ 55
FIGURE 3-8 TRENCH SIDEWALL SHOWING VERTICAL STRIATION MARKS (SCALLOPING) DUE TO THE PROCESS. THE VERTICAL PERIOD IS A FUNCTION OF CYCLE DURATION AND IS OF THE ORDER 1 μM. ........ 55
FIGURE 3-9 ICP DEEP RIE ETCHER MADE BY SURFACE TECHNOLOGY SYSTEMS (STS). ........ 56
FIGURE 3-10 A HIGH ASPECT RATIO ETCH PERFORMED BY STS ICP, THE GAP WIDTH IS 10 μM. ........ 56
FIGURE 3-11 DAMAGED TURBINE LEADING EDGE DUE TO THE FOOTING EFFECT. THE BLADE IS ATTACKED DURING THE 2ND DEEP ETCHING THAT DEFINES THE JOURNAL BEARING. DURING THIS ETCH THE TURBINE IS BONDED TO AN OXIDIZED HANDLE WAFER. WHEN JOURNAL ETCH BREAKS THROUGH, THE INJECTED IONS ACCUMULATE AT THE OXIDE INTERFACE AND DEFLECT THE IONS SIDEWAYS TO ATTACK THE TURBINE TIP. ........ 57
FIGURE 3-12 SEM SHOWING THE NEEDLE-LIKE RESIDUE AT THE INTERFACE OF TWO OVERLAPPING DEEP ETCHES (ETCHED FROM BOTH SIDES). THESE NEEDLES ARE USUALLY ABOUT 1-2 MICRON WIDE, AND THEIR HEIGHT DEPENDS ON THE LENGTH OF THE OVERLAPPED REGION. THESE NEEDLES COULD BE ELIMINATED BY A SHORT ISOTROPIC ETCH AND REDUCED BY MINIMIZING OVERETCH. ........ 59

FIGURE 3-13 SEM SHOWING THE PITTING EFFECT. AN ACCELERATED ETCH PITS THE ROOT OF SHARP FEATURES AND DIG INTO THE SURFACE. THIS IS VERY UNDESIRABLE BECAUSE OF THE STRESS CONCENTRATION PROBLEMS. THE PICTURE ALSO SHOWS THE PROBLEM OF HAVING A REENTRANT PROFILE THAT GRADUALLY REMOVE THE NARROW FEATURES (LINEWIDTH=10 μM, DEPTH=300 μM). 60
FIGURE 3-14 SEM SHOWING THE ROOT FILLET OF THE TURBINE BLADE LEADING EDGE. ............................ 60
FIGURE 3-15 COMPOSITE RESIST OXIDE MASK ON TOP OF SILICON. A ONE MICRON OXIDE WAS WET PATTERNED USING THE 5.2 μM PHOTORESIST. THIS MASK WAS USED FOR THE ETCHES SHOWN IN FIGURE 3-19 AND FIGURE 3-20. IT WAS CONCLUDED THAT THE EXTRA OXIDE LAYER DID NOT IMPROVE THE TRENCH PROFILE. ............................ 63
FIGURE 3-16 RESIST PROFILE AFTER 30MINUTES HARDBAKE AT 90C. ............................ 65
FIGURE 3-17 TAPERED JOURNAL BEARING ETCH (THE ETCH STARTS FROM THE BOTTOM). WE BELIEVED THAT THE TAPER IS CAUSED BY SIGNIFICANT EROSION OF THE REFLOWED RESIST SIDEWALL WHEN ETCHING BONDED WAFERS. ............................ 65
FIGURE 3-18 MIT 56 3 HOURS. ORIGINAL RESIST MASK OPENING IS 11 μM. ............................ 66
FIGURE 3-19 TRENCH PROFILE AFTER 3 HOURS ETCH OF RECIPE MIT 56. WITH COMPOSITE MASK ORIGINALLY DEFINED AS 9 μM, THE ETCH RATE IMPROVES SIGNIFICANTLY AND THE EROSION PROBLEM IS REDUCED DUE TO THE REDUCTION IN ETCH TIME. ............................ 67
FIGURE 3-20 (A) DEEP ETCHED TRENCH WITH MIT RECIPE 59 FOR 4 HOURS. THE ETCH IS PATTERNED WITH A RESIST/OXIDE COMPOSITE MASK WITH AN ORIGINAL OPENING OF 7 μM. (B) THE MASK PROFILE AFTER ETCHING, IT IS CLEAR THAT THE EDGE HAS BEEN SIGNIFICANT ERODED AND BEARING GAP IS WIDENED. THE SURFACE NEAR THE OPENING IS VERY ROUGH DUE TO MASK EROSION AND ION IMPINGEMENT. .... 68
FIGURE 3-21 MULTIPLE WAFER ALIGNED ETCHING/BONDING PROTOCOL. ............................ 69
FIGURE 3-22 INFRA-RED IMAGE OF A FUSION BONDED PAIR OF SILICON WAFERS. THERE ARE SEVERAL VOIDS CASUED BY EITHER PARTICLES OR SURFACE CONTAMINATION. ............................ 72
FIGURE 3-23 IR IMAGE OF BONDED 5-WAFER STACKS. ............................ 74
FIGURE 3-24 LASER ASSISTED SILICON ETCHING. (T. BLOOMSTEIN, 1995) ............................ 75
FIGURE 3-25 EXTENSION OF ALIGNED MULTIPLE WAFER ETCHING/BONDING PROTOCOL TO CREATE A FREE-MOVING PART. ............................ 76
FIGURE 3-26 SEM SHOWING THE SACRIFICIAL TABS THAT HOLD THE ROTOR SHAFT. (A) THE IMAGE IS TAKEN FROM THE MAIN AIR EXHAUST. (B) CLOSE-UP VIEW OF THE TAB. THE HEIGHT IS 100 μM, WIDTH IS 300 μM, LENGTH 100 μM. (C) FURTHER CLOSE-UP SHOWS THE RECESS CUT INTO THE TAB, THE LEFT HALF IS BONDED, WHILE THE RIGHT HALF HAS A 1 μM GAP. ............................ 77
FIGURE 3-27 SEM SHOWING THE COMPLETELY REMOVED TAB. OVERETCH OF THE ORDER OF A FEW MICRONS THAT CUTS INTO THE ROTOR SHAFT IS ALSO SHOWN. ............................ 78
FIGURE 3-28 THIN FILM SHELLS THAT IMPEDE COMPLETION OF THE TAB REMOVAL. ............................ 78
FIGURE 3-29 THE COLLAPSED THIN FILM SHELL. THE TAB IS STILL REMOVED IN THIS CASE. ............................ 79
FIGURE 4-1 CONCEPT OF MICRO BEARING RIG PACKAGING. ............................ 85

Figure 4-2 Diagram illustrates the flow control and testing system. FTB: forward thrust bearing. ATB: aft thrust bearing. AME: aft main exhaust. A pair of pressure dividers enable the one-knob operation. ........ 88
Figure 4-3 Rotor acceleration rate. ........ 89
Figure 4-4 Fiber optic speed sensor ........ 91
Figure 4-5 Signals from the photo detector and the amplified signal. ........ 92
Figure 4-6 Philtec (D6-A1BMTV+L+H) position sensor output. ........ 94
Figure 5-1 Opposed thrust bearing pair. The load W is supported by a net-force F developed from fluid pressure acting on top and bottom. We define the bearing gap width in each side to be g when the rotor is centered. The total gap will be 2g, which equals to maximum travel of the rotor. The rotor axial displacement is defined as z, and the axial position is typically expressed in a non-dimensional form as z/g, denoted as axial eccentricity ε. The stiffness is defined as the derivative of the net-force F with respect to z. ........ 98
Figure 5-2 Pressure flow relationships for hydrostatic thrust bearing with rotor at different eccentricity. The calculation assumes eight 100 μm long, 12 μm diameter capillaries, and a bearing gap of 2 μm (when ε=0). ........ 99
Figure 5-3 Predicted (a) bearing force with respect to gap and supply pressure for a single thrust bearing, and (b) net bearing force from a pair of opposed bearings. This is calculated based on a design of with eight 12 μm diameter, 100 μm long capillaries. ........ 101
Figure 5-4 Effect of capillary diameter on bearing force for a single thrust bearing, showing results of bearings with eight 100 μm long capillaries. ........ 102
Figure 5-5 Mesh convergence test. 2D CFD calculation results for flow between 2 μm gap parallel plates is compared with the analytical solution. A 7x100 mesh (7 layers across the flow and 100 grids along the flow) yields a good match. ........ 103
Figure 5-6 Static pressure contours (in psig) of fluid in bearings with eight 12 μm diameter capillaries and a (a) 0.5 μm, (b) 3 μm, (c) 4 μm gap. ........ 106
Figure 5-7 Velocity contour of the 12 μm capillary design with 4 μm total gap bearing at zero eccentricity. The velocity unit is m/sec. The inherent restriction effect is clearly shown (high velocity flow near the exit of the capillary). ........ 107
Figure 5-8 Loading - position relationship for a 12 μm capillary bearing with a 2 μm bearing gap. As compared to the next figure, the curves have steeper slopes represent better stiffness of this design. ........ 108
Figure 5-9 Load capacity versus bearing position for a single thrust bearing based on 3D CFD simulations. The design values are: 16 μm diameter and 100 μm long capillary, bearing gap is 1 μm. There are 8 capillary restrictors per thrust bearing. ........ 108

FIGURE 5-10 STATIC PRESSURE CONTOUR OF BEARING WITH (A) 8 CAPILLARY RESTRICTORS, AND (B) 16 CAPILLARY RESTRICTORS. BOTH HAS 2 μM GAP AND 100 PSIG SUPPLY PRESSURE. THE 16 RESITRICTOR MODEL HAS MORE AXISYMMETRIC PRESSURE CONTOURS AND HIGHER AVERAGE PRESSURE. TO SAVE CALCULATION TIME, THE CENTER PORTION OF THE BEARING WAS NOT SIMULATION. THE UNIT OF PRESSURE IS PSIG. ........ 109

FIGURE 5-11 LOADING - POSITION RELATIONSHIP OF THRUST BEARINGS WITH 16 CAPILLARIES, AND 2 μM BEARING GAP. BOTH SHOW FURTHER IMPROVEMENT IN THE MAXIMUM LOADING COMPARED TO 8 CAPILLARY DESIGN. HOWEVER, ONLY FOR THE 10 μM CAPILLARY CASE, THE SLOPE OF THE FORCE-GAP CURVES INCREASES SIGNIFICANTLY OVER THE 12 μM, 8 CAPILLARY DESIGN. ........ 110

FIGURE 5-12 PRESSURE-FLOW RELATIONSHIP OF THRUST BEARINGS FROM BUILD 4 AS COMPARED TO SIMULATIONS ASSUMING EIGHT 16 μM DIAMETER RESTRICTORS. (A) FTB BEFORE LAE. (B) BOTH FTB AND ATB AFTER LAE. BARS ON THE EXPERIMENTAL DATA ARE STANDARD DEVIATION OF MEASUREMENTS AT EACH PRESSURE. ........ 113

FIGURE 5-13 (A) PRE-LAE THRUST BEARING FLOWS FROM BUILD-6. (B) POST LAE FLOW. (8 CAPILLARY DESIGN) THE LEGEND SHOWS THE LABEL OF EACH DEVICE. ........ 114

FIGURE 5-14 THRUST BEARING FLOW FROM BUILD 7, 16 CAPILLARY DESIGN, PRE-LAE. ........ 115

FIGURE 5-15 YIELD CHARACTERIZATON BASED ON THE THRUST BEARING FLOW MEASUREMENT. FLOW MEASUREMENTS ARE TAKEN AT A SOURCE PRESSURE OF 100 PSI. FROM THE FTB DATA, WE CAN EXCLUDE 4-2 AND 4-11 FROM GOOD DIES DUE TO THE USUAL HIGH FLOW RATE, AND EXCLUDE 4-5 DUE TO PLUGGING. ALL ATB FLOW DATA SHOW LOWER FLOW RATES DUE TO BONDING ISSUES AND LARGER SCATTERING DUE TO PACKAGING. WE CAN FURTHER EXCLUDE 4-10 VIEWING ITS LOW FLOW RATE. 117

FIGURE 5-16 CONTOUR PLOT OF FLOW RATES AS RELATED TO BEARING CAPILLARY DIAMETER AND GAP. THESE DATA ARE CALCULATED BY CFD ASSUMING A DESIGN OF 8 CAPILLARIES OF 100 μM LENGTH. ........ 119

FIGURE 5-17 (A) TURBINE ROTOR FLOW PATH AND (B) MAIN FLOW RESISTANCES IN THE MICRO BEARING RIG. ........ 120

FIGURE 5-18 JOURNAL BEARING AXIAL CROSS FLOW. THE FLOW RATE IS MEASURED BEFORE THE LAE WHEN THE JOURNAL BEARING GAP IS FIXED. THE CFD CALCULATIONS ARE SHOWN IN LINES FOR COMPARISON. ........ 121

FIGURE 5-19 EXPERIMENTAL RESULTS OF THE JB AXIAL FLOW FROM BUILD 6 AND BUILD 7. RESULTS ARE BASED ON MEASUREMENTS FROM 4 SAMPLES FROM EACH BUILD AND IT SHOWS AN IMPROVEMENT IN REPEATIBILITY ACROSS SAMPLES FOR THIS LATEST BUILD. THE BARS REPRESENT THE STANDARD DEVIATION OF THE MEASUREMENTS. ........ 122

FIGURE 5-20 JOURNAL BEARING GAP SHOWN BY CROSS-SECTIONAL SEM: (A) BUILD 3, (B) BUILD 6, (C) BUILD 7. ........ 123

FIGURE 5-21 ROTOR AXIAL POSITIONING TEST. ........ 124

FIGURE 5-22 ROTOR AXIAL POSITIONING TEST RESULT FROM SAMPLE 6-3. THE CIRCLES REPRESENT RESULTS FROM A TEST DURING WHICH THE AFT SOURCE PRESSURE ($P_A$) IS FIXED AT 100 PSIG, AND THE TRIANGLES REPRESENT RESULTS WITH FORWARD SOURCE PRESSURE ($P_F$) FIXED AT 100 PSIG. THE X-AXIS REFERS TO THE NON-FIXED SOURCE. ........ 125
FIGURE 5-23 ASYMMETRY RESULTS FROM ROTOR AXIAL POSITION TEST. ........ 126
FIGURE 5-24 ROTOR AXIAL POSITION TEST FROM (A) SAMPLE 4-6, AND (B) 6-7. EACH PAIR OF CURVES REPRESENTS ONE TEST DURING WHICH THE AFT THRUST BEARING PRESSURE IS HELD CONSTANT AND THE FORWARD THRUST-BEARING PRESSURE IS ADJUST TO MOVE THE ROTOR DOWN. FIVE TESTS WERE DONE WITH THE FIXED PRESSURE SET FROM 20 PSIG TO100 PSIG. ........ 127
FIGURE 5-25 EXPERIMENTS (FROM FIGURE 5-22) VS. SIMULATIONS FOR THE ROTOR AXIAL POSITIONING TEST. ........ 128
FIGURE 5-26 BEARING PERFORMANCE IMPROVEMENT IN (A) LOAD CAPACITY (N); (B) STIFFNESS (N/μM) AS INDICATED BY CFD CALCULATIONS FOR A PAIR OF OPPOSED BEARINGS. EFFECTS OF INCREASING THE GAP, THE NUMBER OF CAPILLARIES, AND REDUCING CAPILLARY DIAMETER ARE SHOWN. ........ 130
FIGURE 6-1 HYDROSTATIC JOURNAL BEARING OPERATION BASED ON 'ENTRANCE LENGTH'. ........ 134
FIGURE 6-2 HYDROSTATIC TESTING RESULTS. THE ROTOR SPINS 4 TIMES AND IS CAPTURED BY THE FREQUENCY-TO-VOLTAGE CONVERTER AS SPIKES IN (A). DUE TO THE QUICK CRASH, THE F/V SPEED CONVERSION IS INACCURATE. THE SPEED IS CALCULATED BY POST-PROCESSING THE PULSE DATA AND SPEED VARIATION IN THE FOURTH SPIKE IS RE-PLOTTED IN (B). THE ROTOR ACCELERATES THREE TIMES, REACHING 40,000 RPM BEFORE EACH CRASH. ........ 136
FIGURE 6-3 HYDROSTATIC SPEED RUN OF SAMPLE 6-7, THE ROTOR ACCELERATES TO 110,000 RPM IN THIS RUN, WITH THE SPEED BE PROPORTIONAL TO THE MAIN PRESSURE. THE MAXIMUM MAIN PRESSURE ONLY REACHES 0.8 PSI AND THE THRUST BEARING BALANCE IS UNAFFECTED AT THIS PRESSURE AS SHOWN BY A STEADY FLOW RATE. (COURTESY OF S. JACOBSON) PM, PH1,PH2, AND PL STAND RESPECTIVELY FOR MAIN PRESSURE, HIGH SUMP 1 PRESSURE, HIGH SUMP 2 PRESSURE, AND LOW SUMP PRESSURE. PHILTEC SENSOR IS USED TO MEASURE SPEED IN THIS TEST ........ 137
FIGURE 6-4 MAIN PRESSURE - SPEED RELATIONSHIPS FOR BUILD 6 DIES. (COURTESY OF S. JOCOBSON).... 138
FIGURE 6-5 OPERATING MAP FOR DIFFERENT HYDRODYNAMIC TESTING MODES. THE THICK GRAY LINE IS THE CALCULATED STABILITY BOUNDARY. DASHED LINE IS THE CONSTANT ECCENTRICITY CONTOUR. THREE METHODS OF PLUMBING THE SUMPS ARE SHOWN. EACH METHOD HAS DIFFERENT THRESHOLD SPEED. THE PLUG HI SUMP-VENT LOW SUMP SCHEME (SQUARES) IS A SIMPLE METHOD TO GET BOTH LOW THRESHOLD SPEED (THE SPEED AT WHICH THE OPERATING LINE CROSSES THE STABILITY BOUNDARY) AND LOW ECCENTRICITY. (COURTESY OF S. JACOBSON AND E. PIEKOS) ........ 139
FIGURE 6-6 (A) HYDRODYNAMIC TEST RESULT, THE SPEED DATA IS ESTIMATED BY A FREQUENCY TO VOLTAGE CONVERTER. (B) CLOSE-UP VIEW SHOWING THE SPEED FROM POST-PROCESSING STORED BLADE-PASS DATA. IT SHOWS THE ACCELERATION-CRASH CYCLES OFTEN SEEN IN THE EARLY HYDRODYNAMIC TESTS. ........ 141

FIGURE 6-7 SPECTRUM OF SPEED SENSOR PULSES (BLADE COUNT). MAXIMUM SPEED IS ABOUT 70,000 RPM. TO GET THE SPEED IN RPM, WE NEED TO MULTIPLYING THE BLADE COUNT BY 3 (THERE ARE 20 BLADES ON THE ROTOR). ........ 142
FIGURE 8-1 FIRST PACKAGING DESIGN FOR PROTOTYPE TESTING. ........ 159
FIGURE 8-2 TOP COVER PLATE ........ 160
FIGURE 8-3 MIDDLE PLATE ........ 161
FIGURE 8-4 BOTTOM PLATE ........ 162

# List of Tables

TABLE 1 μENGINE AND BATTERY PERFORMANCE COMPARISON [4]. 20
TABLE 2 MICRO TURBINE DESIGN PARAMETERS AND PERFORMANCE WITH TOTAL PRESSURE RATIO OF 4.1 AND OPERATING AT 2,400,000 RPM. IN THE MICRO BEARING RIG, THE LOAD IS MUCH LESS THAN 76W AND IT WILL REQUIRES A SMALLER PRESSURE RATIO TO REACH THE SAME SPEED. 29
TABLE 3 PARAMETERS ESSENTIAL FOR ICP TIME-MULTIPLEXED DEEP-RIE. 62
TABLE 4 RECIPIES USED TO PRODUCE TRENCHES IN THE NEXT TWO FIGURES. 66
TABLE 5 SIMULATION MATRIX FOR 8 CAPILLARY DESIGN. FLOW FOR 6 FEEDING PRESSURES WERE CALCULATED FOR EACH DESIGN DIMENSION. 106
TABLE 6 RECIPIES PROVIDED BY STS WITH STS ICP ETCHER. 152
TABLE 7 RECIPES FOR LAM 480 PLASMA ETCHER (ICL ETCHER-1) 152
TABLE 8 THERMAL OXIDE PROCESS (FOR HANDLE WAFER) 152
TABLE 9 LAM 480 (ETCHER-1) RECIPE 19. 156
TABLE 10 AME 5000 (MAGNETRON) SHALLOW PLASMA ETCHING PARAMETERS. 156
TABLE 11 NOVELLUS SACRIFICIAL OXIDE RECIPE 156
TABLE 12 OXFORD SACRIFICIAL OXIDE RECIPE 156
TABLE 13 RECIPIES DEVELOPED AT MIT TO BE USED FOR DEEP ETCHING. 157
TABLE 14 THICK RESIST (AZ4620) SPIN PROCESS 157
TABLE 15 PLASMA-QUEST PRE-LAE CLEAN 157

# Chapter 1

# Introduction

### *Section 1.1 Motivation and Overview*

Modern systems require increasing amount of power to operate. One of the most efficient power sources, the land-based gas turbine engine, produces electric power that supplies more than 10% of the United States utility electricity. This number will triple in the next decade as the power industry improves the efficiency of coal-burning power plants by incorporating gas turbines. [1,2]

In a gas turbine generator, power is converted through a continuous thermodynamic combustion cycle (Brayton cycle). Ambient air is sucked into the engine, and its pressure is raised by the compressors. The pressurized air is mixed with fuel and burned in the combustor. The hot air then expands through the turbine, generating power in excess of what is needed to drive the compressor. A generator transforms the excess shaft power to electric power.

While large power plants are being built or upgraded to meet the increasing need for electricity, portable power sources are also seeing extremely high demand. Although there is a constant drive to reduce the power consumption of portable systems, the added functionality and complexity of these systems usually cancels such reductions. This is well demonstrated by the battery life of portable computers, which have not improved much regardless of advances in battery technology. Thus, a big leap in portable power sources would solve many problems.

Since direct on-site energy conversion reduces both power transmission loss and storage issues, building a micro gas turbine generator is an attractive means to satisfy the growing demand in the portable power. Moreover, an initial calculation shows that the power density of a micro gas turbine generator is more than 10 times higher than state-of-the-art lithium batteries (Table 1). At the same time, Micro-electrical-mechanical systems (MEMS) technology could provide the fabrication techniques needed to realize this micro device. Viewing these, a program, sponsored by Army Research Office, was initiated at MIT to develop technologies that will enable a micro gas turbine generator. The initial goal of the program is to build a 0.5-inch diameter size device that will produce 50W of power. [3-6]

| | μEngine + fuel | $LiSO_2$ battery (BA5590) |
|---|---|---|
| Power output (W) | 50 | 50 |
| Energy (w-hr) | 175 | 175 |
| Weight (grams) | 50 | 1000 |
| Size ($cm^3$) | 60 | 880 |
| Specific Energy (w-hr/kg) | 3500 | 175 |
| Energy Density (kw-hr/$m^3$) | 3000 | 200 |

**Table 1 μEngine and battery performance comparison [4].**

The baseline design of the gas turbine engine is shown in Figure 1-1 [7-9]. It consists of a 1-stage centrifugal compressor and radial inflow turbine, with a fuel injection system and a combustion chamber located in between. [10-12] A generator is attached to the compressor shroud, which has the lowest temperature on the rotor. Air bearings support the rotor. A hollow shaft is designed to reduce heat conduction from the turbine to the compressor. [13,14] The size of the engine, particularly its millimeter-range thickness, is larger than most MEMS devices. When compared with a commercially available engine such as the ABB GT13 gas turbine (Figure 1-2), we notice that the microengine is greatly simplified. But this microengine is arguably one of the most complicated MEMS device considering the mask count, the number of wafer required, the necessary tolerances, and the fact that a freely-rotating part is included.

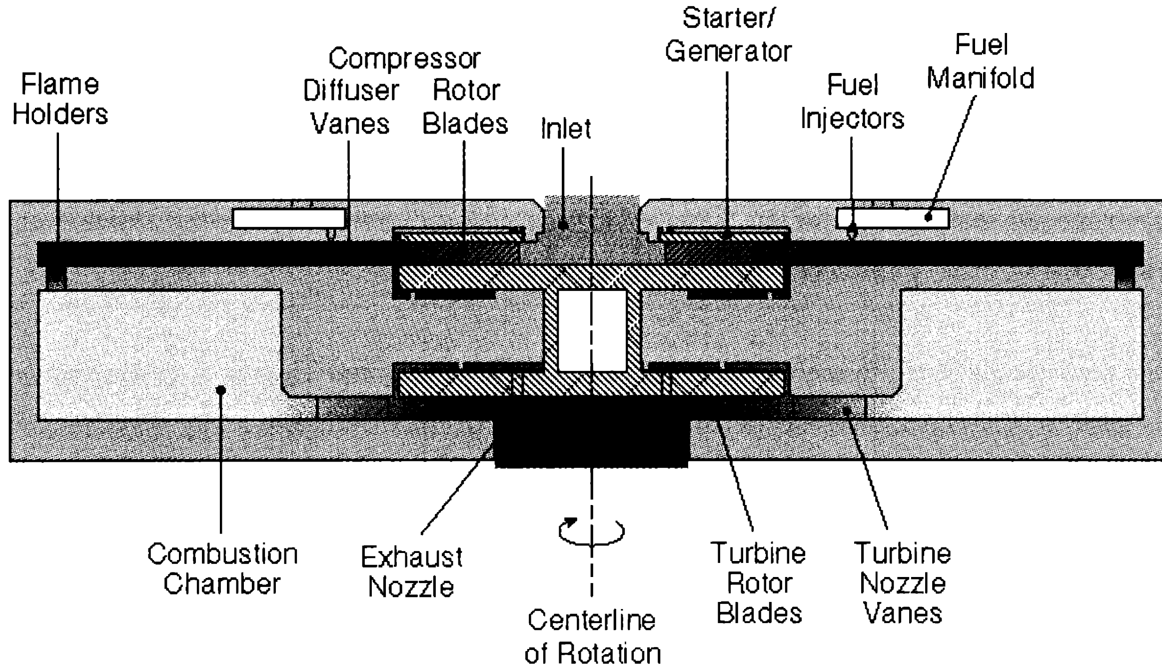


**Figure 1-1 MIT Micro Gas Turbine Generator. It has about 10 parts, with inlet diameter of 2 millimeters and weight of 1 gram without fuel. The flow rate is about 0.1 gm/sec.**

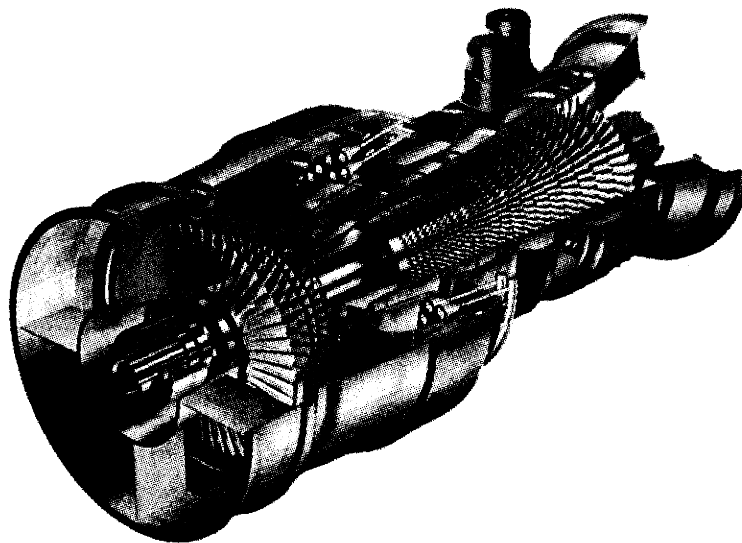

**Figure 1-2 ABB GT13 gas turbine. It has about 10,000 parts, with inlet diameter of 2 meters and weight of 400 tons. The air flow rate is of the order of 500 kg/sec and it produces 150 MW of power. The typical purchase cost is about $300/kW.**

A core element of the micro gas turbine generator is the high-speed turbine and compressor. We are addressing the challenge of building a micro gas turbine generator by first building sub-components. An important subcomponent that we need to build is a micro device that demonstrates high-speed rotation. The essential components of this device include: 1, A source of torque; and 2, High speed radial and axial bearings. The micro bearing rig was the subcomponent implemented for this purpose. This concept comes from Dr. Fredric Ehrich, who also helped with the component design.

This thesis is dedicated to the development of the micro bearing rig. The micro bearing rig is designed to study microfabricated air bearing and rotordynamics. In addition, by developing a baseline fabrication process for the micro bearing rig, we can extend it to build other micro devices and the final engine.

### Section 1.2 Thesis Goals

This thesis is targeted at the fabrication and characterization of the micro bearing rig, which is a micro turbine supported by a pair of thrust bearings and a journal bearing. The main goals of this thesis are:

1. To establish a baseline fabrication process for the micro-bearing rig that can be extended to build other sub-components as well as the final engine.

2. To develop an instrumentation system and packaging scheme that will allow for the testing of the micro-bearing rig.

3. To characterize the performance of the micro air bearing and evaluate the analysis code.

To summarize, the goal of the thesis is the realization of a complex fabrication process and as well as the packaging and test protocol necessary for a micro turbine that spins. The micro bearing rig is a 3-dimensional structure with a freely rotating part, and its process can be extended to build more complicated MEMS devices, such as a micro gas turbine engine. The set of

instrumentation and testing results should serve as useful guidelines to help the MIT micro engine project reach the final goal.

### *Section 1.3 Thesis Layout*

The thesis is organized into the following parts. An overview of the micro bearing rig design is described in chapter 2, followed by device fabrication in chapter 3. Packaging and instrumentation are discussed in chapter 4. Then chapter 5 and 6 present the thrust bearing flow models and flow measurements. Chapter 7 discusses the spin test results. Finally, conclusions are drawn in chapter 8 along with recommendations for future work. Details of the process flow, package design, and fluidic model are included in appendices.

### *Section 1.4 Reference*


[1] "Challenges of Electric Power Industry Restructuring for Fuel Suppliers", DOE/EIA-0623, Sep, 1998.

[2] "Boosting Power Plant Efficiency", Global Climate Change – a Fossil Energy Issue Review, Office of Fossil Energy, DOE, March 5, 1999.

[3] Epstein, A. H., et. al. "Micro Gas Turbine Generators", Interim Technical Progress Report, ARO 33888CH-MUR, Army Research Office, N.C., 1995.

[4] Epstein, A. H., et. al. "Micro Gas Turbine Generators", Interim Technical Progress Reprot, Massachusetts Institute of Technology, Cambridge, MA, 1996.

[5] Epstein, A. H., C. Groshenry, C. W. Haldeman, M. A. Schmidt, S. D. Senturia, C. S. Tan, I. A. Waltz, and J. Wong, [1995]: "Final Technical Report entitled Microjet Engines", MIT Lincoln Laboratory, Lexington, MA, Apr. 1995

[6] Epstein, A. H. and S.D. Senturia, [1997]: "Micro Power from Micro Machinery," Science, Vol. 276, pp. 1211, May, 1997.

[7] Epstein, A. H., S.D. Senturia, G. Anathasuresh, A. Ayon, K. Breuer, K-S Chen, F. E. Ehrich, G. Gauba, R. Ghodssi, C. Groshemy, S. Jacobson, J.H. Lang, C-C Lin, A Merha, J.M.

Miranda, S. Nagle, D.J. Orr, E. Piekos, M.A. Schmidt, G. Shirley, M.S. Spearing, C.S. Tan, Y-S Tzeng, I.A. Waitz, [1997]: "Power MEMS and Microengines," IEEE Transducers '97 Conference, Chicago, IL, June 1997.

[8] Epstein, A. H, S.D. Senturia, O. Al-Midani, G. Anathasuresh, A. Ayon, K. Breuer, K-S Chen, F.F. Ehrich, E. Esteve, L. Frechette, G. Gauba, R. Ghodssi, C. Groshenry, S.A. Jacobson, J.L. Kerrebrock, J.H. Lang, C-C Lin, A. London, J. Lopata, A. Mehra, J.O. Mur Miranda, S. Nagle, D.J. Orr, E. Piekos, M.A. Schmidt, G. Shirley, S.M. Spearing, C.S. Tan, Y-S Tzeng, I.A. Waitz, "Micro-Heat Engines, Gas Turbines, and Rocket Engines - the MIT Microengine Project," 28th AIAA Fluid Dynamics and 4th AIAA Shear Flow Control Conference, June 1997.

[9] Groshenry, C. [1995]: "Preliminary Design Study of a Micro-Gas Turbine Engine," Master thesis, Department of Aeronautics and Astronautics, Massachusetts Institute of Technology, Cambridge, MA, Sep. 1995.

[10] Mehra, A. and I. Waitz [1997]: "Development of a Hydrogen Combustor for a Microfabricated Gas Turbine Engine," Technical Digest, the Solid-State Sensor and Actuator Workshop, Hilton Head, SC, June 8-11, 1998, pp. 35-40.

[11] Tzeng, Y. S. [1997]: "An Investigation of Microcombustion Thermal Phenomena," SM thesis, Department of Aeronautics and Astronautics, Massachusetts Institute of Technology, Cambridge, MA, June,1997.

[12] Waitz, I. A., G. Gauba, and Y-S Tzeng, "Combustors for Micro-Gas Turbine Engines," ASME J. of Fluid Eng., Vol. 120, March, 1998.

[13] Spearing, S. M. and K. S. Chen [1997]: "Micro Gas Turbine Engine Structures and Materials," 21st Annual Cocoa Beach Conference and Exposition on Composite, Advanced Ceramics, Materials and Structures, Jan, 1997.

[14] Chen, K.S., "Materials Characterization and Structural Design of Ceramic Micro Turbomachinery", Ph.D. thesis, MIT, Feb., 1999.

# Chapter 2

# Micro Bearing Rig Design

This chapter is organized into three sections to introduce the design of three important components of the micro-bearing rig: the turbine, thrust bearings, and journal bearing.

The design of the micro bearing rig involves the cooperation of a number of people. The initial functional design was undertaken by Dr. Fredric Ehrich, with the detailed geometry and dimensions determined by the members of micro-fabrication and fluidic mechanics groups. Professor Epstein, Professor Schmidt, and Dr. Jacobson have also provided important input to the functional design.

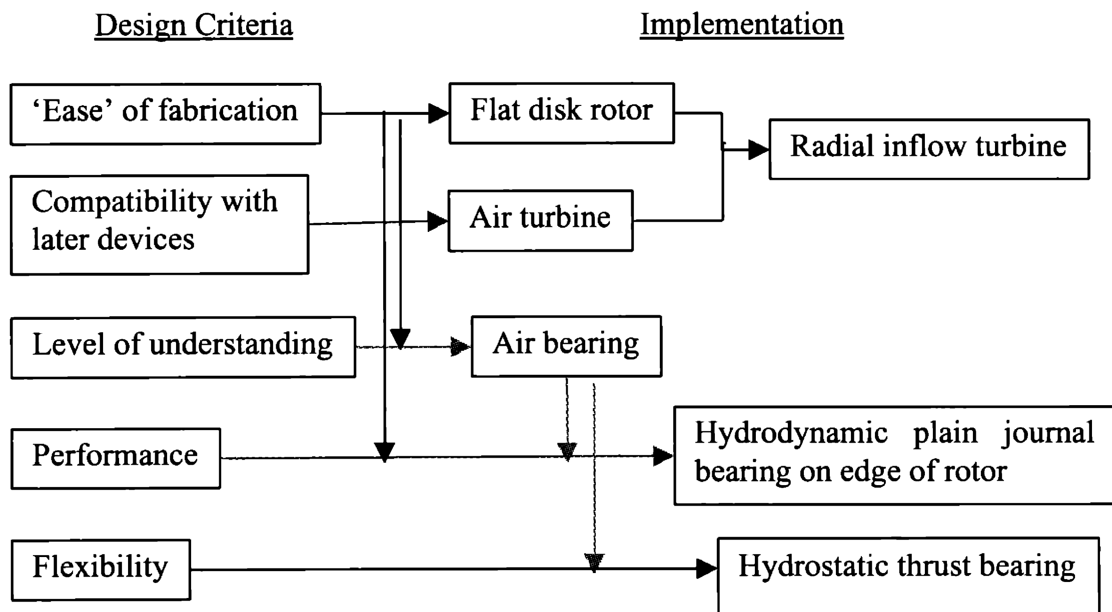


**Figure 2-1 Micro bearing rig component design.**

Figure 2-1 shows the micro bearing rig component design thought process. The left-hand side illustrates five design criteria while the right-hand side shows the implementation. A flat-disk rotor is chosen because of its compatibility with MEMS fabrication techniques. A turbine is the natural choice for a torque source because it is a central component of later devices in the micro engine project. We chose a radial inflow turbine to maximize output power given the aforementioned constraints. To leverage the group's background in fluidic dynamics, we chose air bearings instead of magnetic or electrostatic bearings. Because the device relies on air to operate, choosing air bearings also reduces the geometrical complexity. Next, the location of the journal bearing is chosen, based on fabrication simplicity and performance (minimize gap/rotor radius ratio and considering that centrifugal force will reduce gap at high speed), to be on the rotor disk edge instead of on a center shaft. It is design to be a plain hydrodynamic bearing to reduce fabrication complexity. Finally, a hydrostatic thrust bearing was chosen because of its control flexibility and its low-speed stiffness.

Figure 2-2 shows an exploded view of the micro bearing rig. It is made of 5 bonded wafers, with a total thickness of 2-3 millimeters. The turbine rotor is located in the 3$^{rd}$ (middle) wafer. The rotor is supported axially from above and below by a pair of 1 millimeter diameter thrust bearings, and it is supported radially by the journal bearing. High-pressure air will come in from a turbine air inlet, turn 90 degrees and form air jets after flowing through the turbine inlet guide vanes. The air blows on the turbine and spin it, and then exhaust from the forward main exit that surrounds the forward thrust bearing. The forward thrust bearing is supplied by a separate port that leads to the plenum through the struts, and the air is exhausted through the forward main exit (Figure 2-3). The aft thrust bearing air comes from a port in the 5$^{th}$ wafer, and the air is exhausted through an aft exhaust port. Figure 2-4 shows a cross-sectional layout of the assembled micro bearing rig.

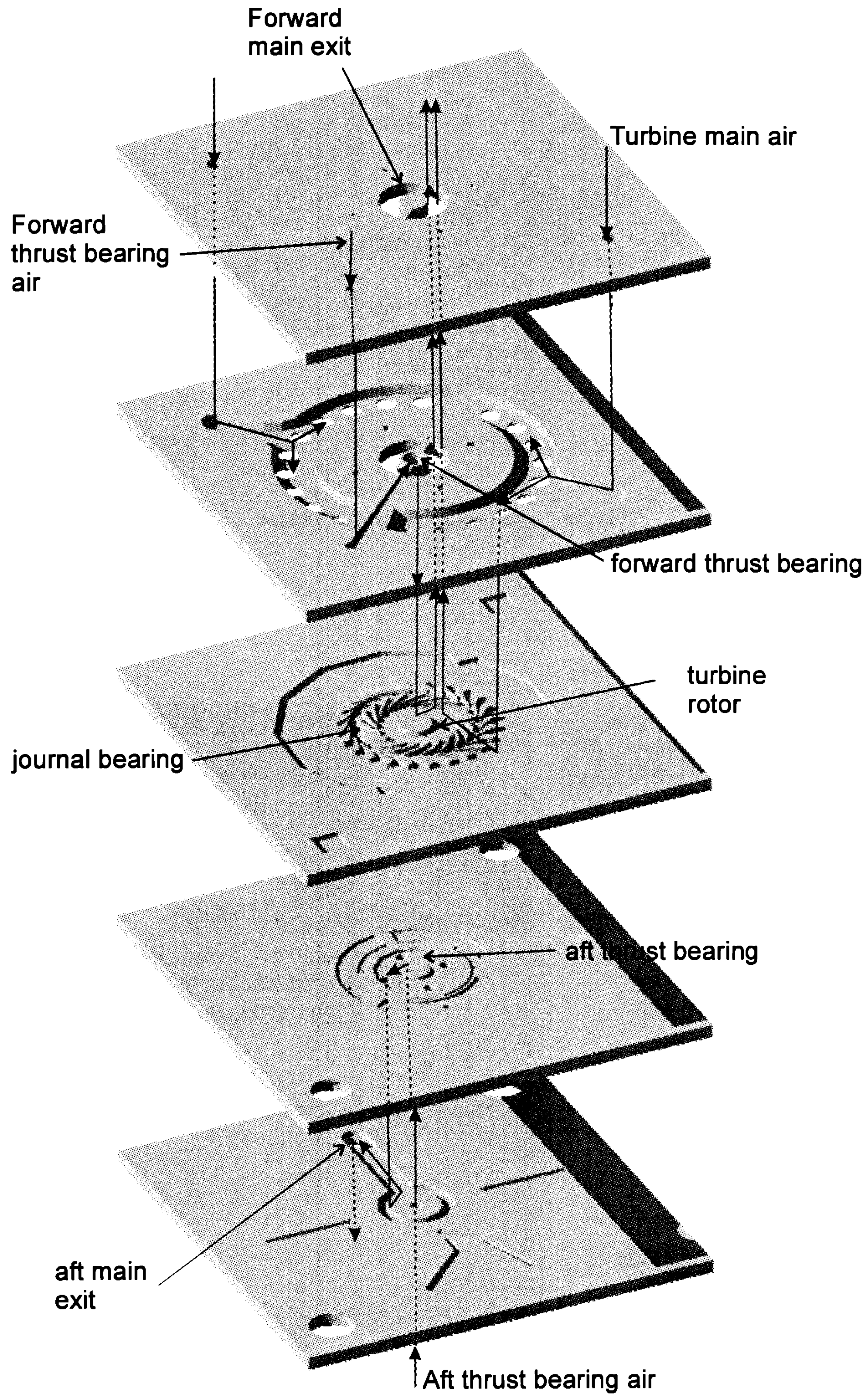


**Figure 2-2 Exploded view of micro bearing rig.**

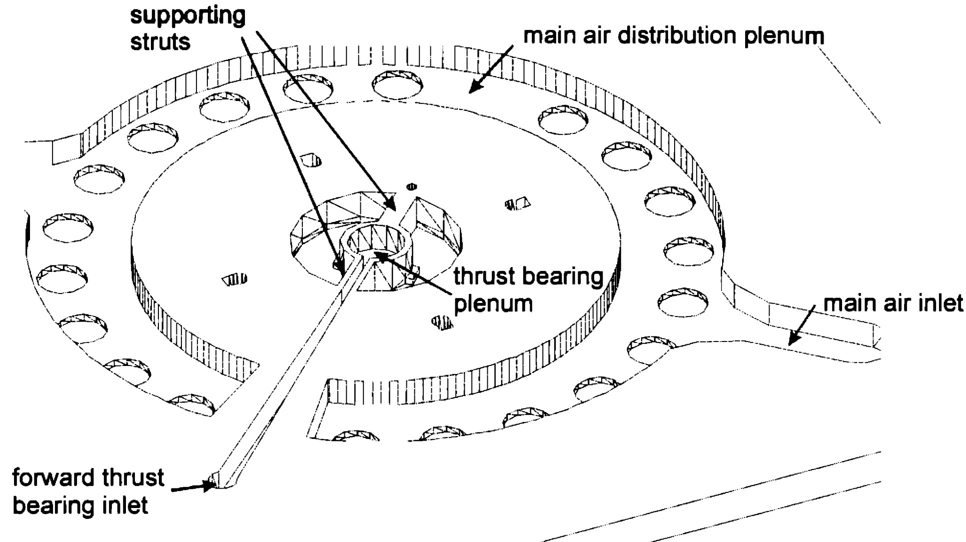


**Figure 2-3 Close-up view of 2nd wafer.**

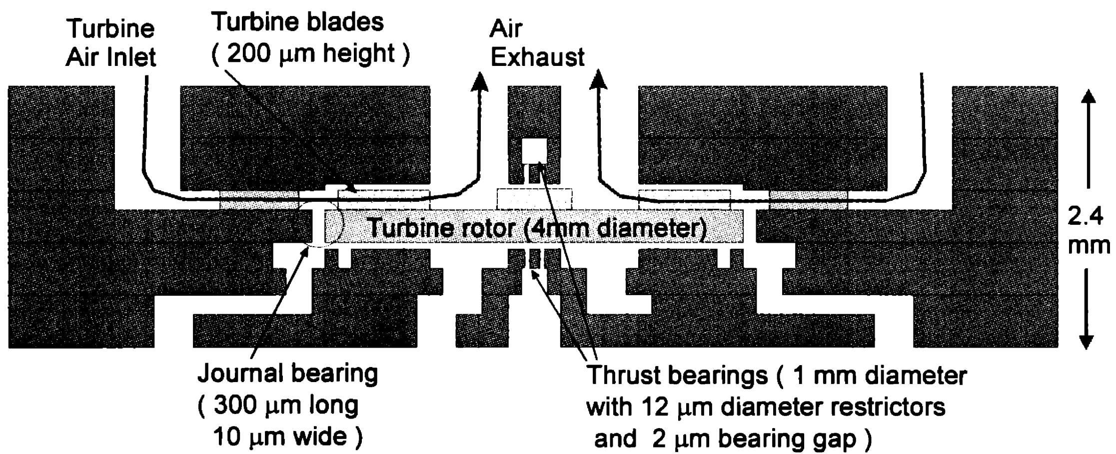


**Figure 2-4 Cross-sectional layout of micro bearing rig.**

### *Section 2.1 Turbine design*

Because the geometry of the turbine blades is limited by the micro-fabrication technology to 2D-extruded shapes, a radial inflow turbine design was favored. Figure 2-5 shows the turbine profile determined by Dr. Stuart Jacobson using the MIT MISES code [1,2]. The calculated design parameters are summarized as follows in Table 2.1. The calculated turbine torque versus speed relationship is shown in Figure 2-6.

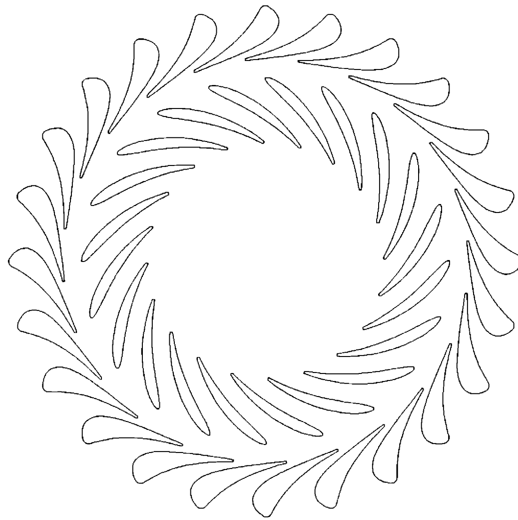

**Figure 2-5 Micro turbine blades design. The rotor spins counter clockwise.**

A detailed investigation of design issues for micro turbomachinery was performed by A. Mehra and is not repeated here [3].

| Parameter | Design value |
|---|---|
| Turbine blade height | 200 μm |
| Turbine blade trailing edge width | 26 μm |
| Turbine blade height to width ratio | 1.7-7.7 |
| Turbine blade inner radius | 1.3 mm |
| Turbine blade outer radius | 2.0 mm |
| Mass flow rate | 0.39 g/s |
| Shaft power | 76 W |
| Isentropic efficiency (total-total) | 0.96 |
| Isentropic efficiency (total-static) | 0.89 |
| Turbine inlet air velocity (abs/rel) | 395 / 160 m/sec |
| Turbine exit air velocity (abs/rel) | 182 / 297 m/sec |

**Table 2 Micro turbine design parameters and performance with total pressure ratio of 4.1 and operating at 2,400,000 rpm. In the micro bearing rig, the load is much less than 76W and it will requires a smaller pressure ratio to reach the same speed.**

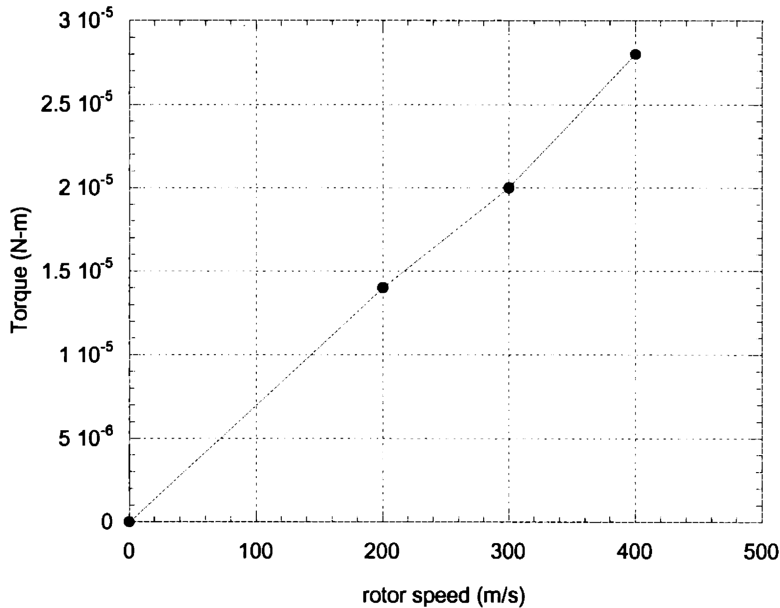


**Figure 2-6 Rotor torque vs. speed for the designed turbine based on MISES result from Dr. S. Jacobson. The torque is calculated by dividing the turbine power by the rotation rate, assuming 9W of viscous dissipation from the bearing at full speed and a quadratic relationship between rotor speed and bearing dissipation.**

### *Section 2.2 Thrust bearing design*

In general, there are two types of air thrust bearings: the self-pressurized hydrodynamic bearings and the externally pressurized hydrostatic bearings.

Hydrostatic bearings rely on an external pressure source that feeds lubricant into the bearing. Figure 2-7 contains an outline of the principle of "externally pressurized lubrication," which is commonly referred to as "hydrostatic lubrication." The lubricant is usually fed by a pump. As the pump starts to run, the pressure in the shallow recess grows (Figure 2-7b) until the lifting pressure is reached (Figure 2-7c). After this point, a lubricant film builds up to separate the bearing pad surfaces, and flow Q is delivered. Different loads (W) lead to different values of the recess pressure and of the film thickness (Figure 2-7e and f).

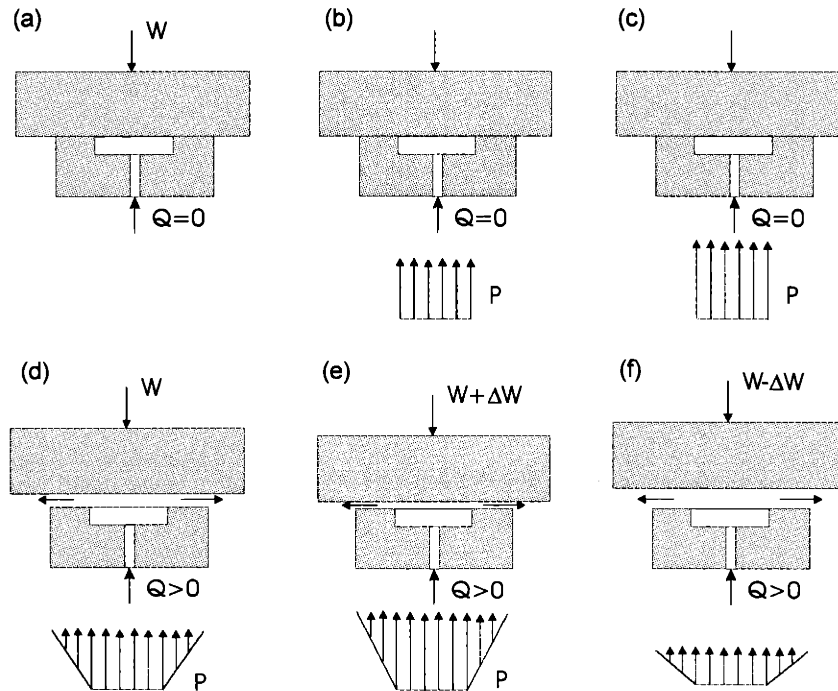


**Figure 2-7 Hydrostatic lubrication. Pressure diagrams and fluid film formation in an axial single-pad bearing [4].**

A pair of opposed thrust bearings double the loading capacity and can support the loads in either direction. When a load is applied as shown in Figure 2-8:

1. As the load increases, the bottom bearing gap closes and the top bearing gap opens.
2. The reduced bottom gap increases the flow resistance, decreasing the flow rate through the bottom bearing. The opposite effect applies to the top bearing.
3. For the bottom bearing the pressure drop through the supply orifice decreases, hence increasing the pressure in the bearing film. (For a pump supplied bearing, decreased flow will increase the pump supply pressure.) On the other hand, the pressure in the top bearing film decrease because pressure drop through supply orifice increases.
4. The bearing gap adjusts until the force developed from the pressure films balances the applied load.

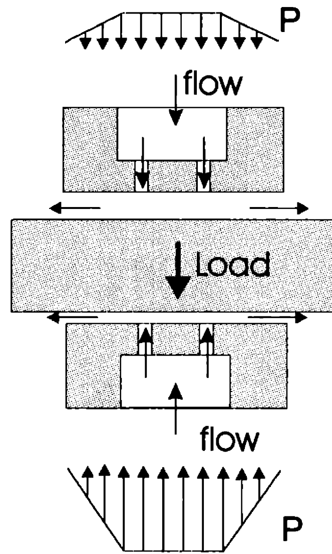


**Figure 2-8 Hydrostatic opposed-pad axial bearing.**

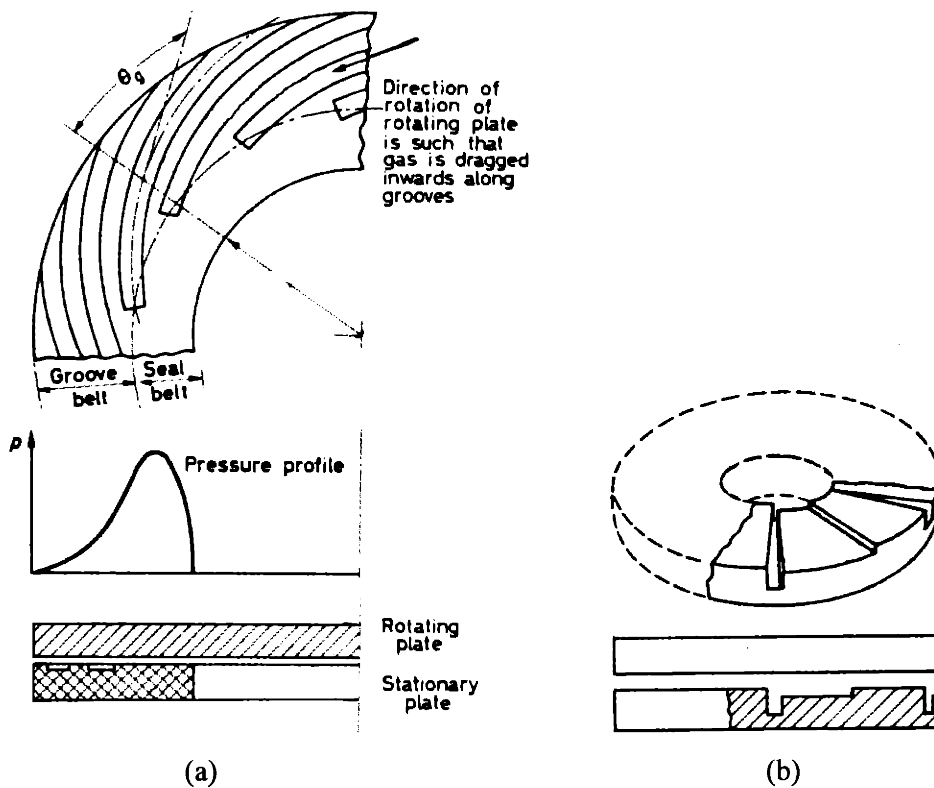


**Figure 2-9 (a) Spiral thrust bearing. (b) Step pad thrust bearing (Figure from reference [5]).**

Hydrodynamic bearings operate in a different manner. The motion of the rotor drags the surrounding viscous fluid, acting to pump the fluid to build up a pressure field that supports the

rotor itself. Many different designs exist the hydrodynamic bearings, including ones with spiral grooves or step pads. (Figure 2-9a, b) They all have the advantage of being easier to micro-fabricate because there is no need to build sealed pressure plenums. But they share the common problem of having poor stiffness at low speeds. Hydrodynamic bearings can provide high stiffness when rotating without the expense of an external pressure source. Nevertheless, they have no stiffness at zero speed and have to grind themselves to start. On the contrary, hydrostatic bearings can provide high stiffness/loading capacity at zero speed, but they are more complicated to build. To allow external control and variation, we chose hydrostatic thrust bearings for the first design. This has the additional advantage of preventing excess friction force and grinding in the thrust bearing during rotor start-up.

Hydrostatic thrust bearings require a proper bearing flow compensation design to maximize their load carrying capacity and stiffness. There are many types of compensation mechanisms. In large-scale bearings, commonly used compensation mechanisms include constant flow system, capillary, orifice, constant flow valve, diaphragm-controlled restrictors, and infinite stiffness designs [6]. Figure 2-10 shows a comparison of different compensation mechanisms as reported in Ref. [6]. The vertical axis is flow rate in (a) and lubricant film thickness in (b), and horizontal axis is the applied load. Infinite stiffness system and constant-flow system are superior to other designs, keeping a relatively large film thickness even at large loads.

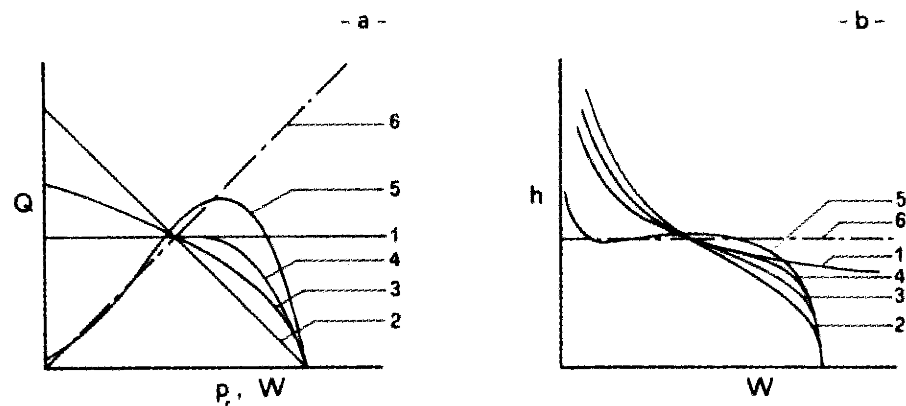


**Figure 2-10 Flow rate Q (a) and film thickness h (b) versus load W for different supply systems; 1 - constant flow system; 2- capillary; 3- orifice; 4- constant flow valve; 5- diaphragm-controlled restrictor; 6- infinite stiffness (h = constant) [6].**

In the micro scale, it is difficult to build complicated systems such as infinite stiffness bearings. Our chosen design is shown in Figure 2-11. The compensation restrictors consist of straight

narrow tubes (capillaries) that connect the high-pressure plenum to the bearing pad. The pressure drop that results from the flow resistance of the capillaries (capillary resistance) and the turning of the flow from the capillaries into a much smaller gap (inherent resistance) serves as the compensating mechanism. A constant pressure is fed to each bearing plenum. When an external load is applied to reduce the gap, the radial outflow resistance in the bearing gap will increase. At the same time, the capillary resistance is insensitive to the reduced bearing gap. The inherent resistance will increase with decreasing bearing gap, but its change is less than the radial flow resistance if designed correctly. Therefore, the pressure at the capillary exit, $P_{bearing}$, will increase with decreasing gap because it is approximately equal to the ratio of the flow resistance,

$$P_{bearing} = (P_{source})\frac{R_{rad}}{R_{cap} + R_{inh} + R_{rad}}, \qquad (2\text{-}1)$$

where the $R_{cap}$, $R_{inh}$, and $R_{rad}$ stands for the nonlinear flow resistances for the capillaries, the inherent restrictors, and the radial outflow between the bearing gap, respectively. And the pressures are gage values with respect to the ambient exhaust. Since the pressure within the bearing gap is proportional to $P_{bearing}$, a stabilizing force will develop to counter the external load and to increase the gap.

In our design, the length of the capillaries is designed to be 100 μm so that they are compatible with the available wafer thickness. The capillary diameter, location and number of the capillaries, and the bearing gap are chosen based upon calculations by Dr. Richard Walker of CS. Draper Lab (using a code developed by MTI [7]). The initial thrust bearing design has eight capillaries located at a radius of 0.35 mm. The capillary diameters is 10 μm and the bearing gap is 1 μm. The size of the bearing pad is chosen to be 1 mm diameter to minimize blockage of the main turbine exhausting flow and allow future device instrumentation.

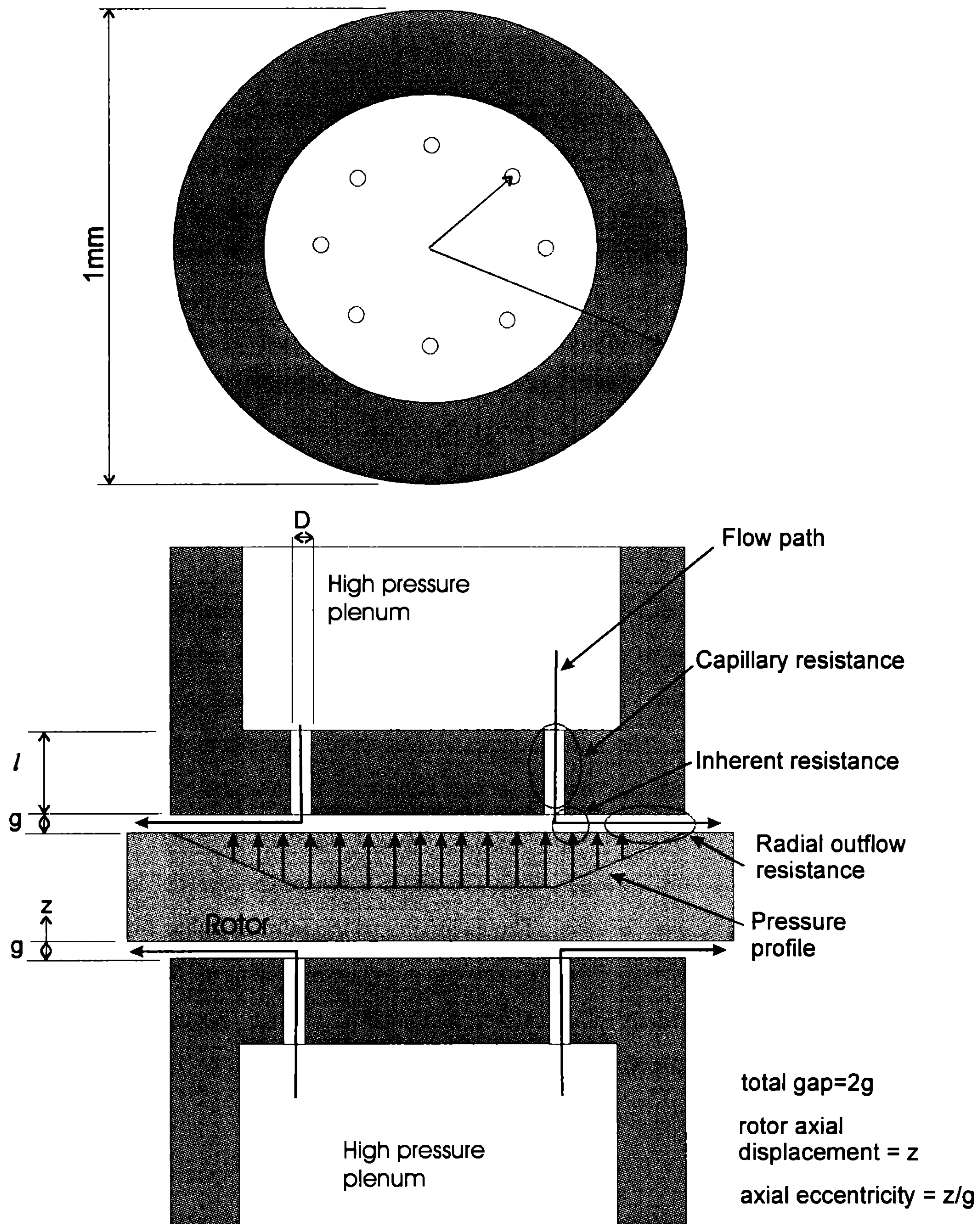


**Figure 2-11 Micro hydrostatic thrust bearing design. This design incorporates both the capillary restriction and inherent restriction effect for bearing compensation. Key design parameters are capillary diameter D, length *l*, and bearing gap g which is half of the total bearing gap because there is a pair of opposed bearings. In the text, values for bearing gap are given in terms of g. Rotor axial position is typically defined as axial eccentricity, which is axial displacement normalized by bearing gap.**

### *Section 2.3 Journal bearing design*

There are several types of radial bearings that are commonly used for supporting rotors. Rolling element bearings are the favored choices in situations when a low starting torque is needed. Also, they have no self-excited instabilities and they are less sensitive to short interruptions in lubrication. Unfortunately, they require large space in the radial direction and critical alignment, and they have low damping capacity, higher drag and lower life time. For higher speed operation that requires lower drag and longer lifetimes, non-contact bearings such as magnetic bearings and gas lubricated bearings are more favored. As mentioned at the beginning of this chapter, we have chosen an air bearing because we want to leverage our knowledge in fluid dynamics. Moreover, the micro bearing rig relies on airflow to operate and air cannot be eliminated in the bearing gap. With this concern, it is easier to implement an air bearing design.[1]

Among many possible designs of air bearings, a hydrodynamic plain journal bearing was chosen because it is relatively simple to fabricate. Hydrodynamic journal bearings rely on a self-generated pressure field to support itself. As shown in Figure 2-12, the bearing requires a load (W) to push the rotor off-center. The rotor acts as a viscous pump that drives the liquid along and high pressure is generated in the converging section (Figure 2-13) to support the load. During stable operation, the rotor position can be defined by attitude angle $\varphi$ and radial displacement e, shown in Figure 2-12. The attitude angle, $\varphi$, is the angle between the applied load and a line connecting the journal and bearing centers. The excursion of the journal center from the bearing center, denoted by e, is typically normalized by the gap $c$ and expressed as an "eccentricity ratio," $\varepsilon$. Hence $\varepsilon = 0$ and $\varepsilon = 1$ represent fully-centered and crashed journals, respectively. At times, the rotor can whirl within a confined region, called the limit cycle, without crashing into the wall.

---

[1] It is worth mentioning that the electrostatic and magnetic bearings are also regarded as backups. But the electrostatic bearing has a low load capacity and its fabrication process is very challenging [7]. The magnetic bearing fabrication is also very difficult, and many materials lose their magnetic properties at the gas turbine operating temperature.

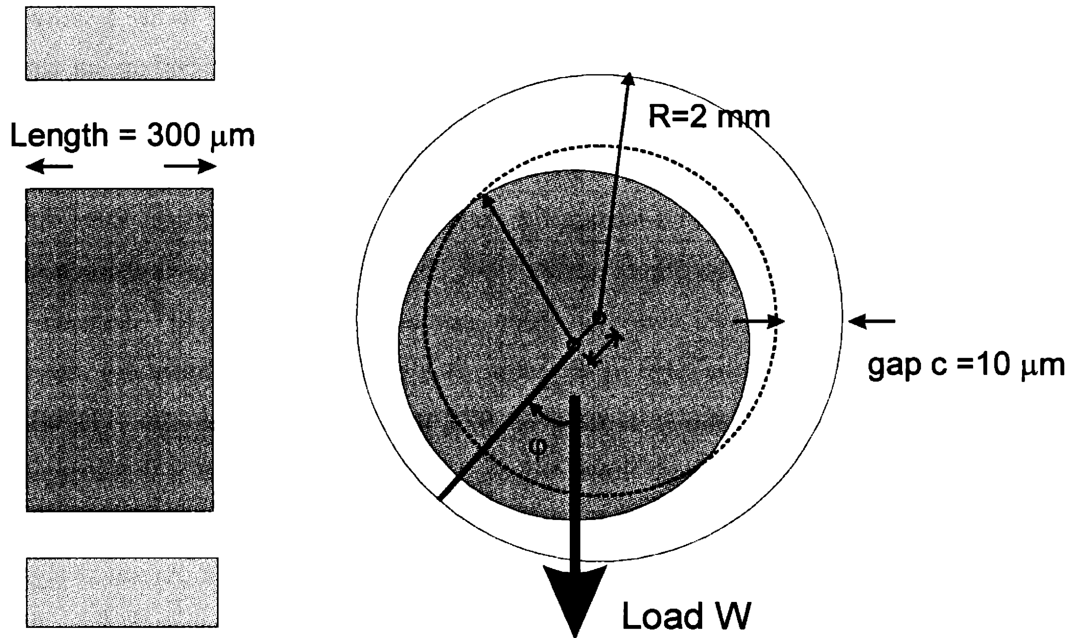


**Figure 2-12 Plain hydrostatic journal bearing. The drawing is not to scale to highlight the key dimensions. The rotor has a radius r and the bearing radius is R. The bearing gap is c, and bearing is loaded by W. The stable position is not aligned with the loading but forms an angle called the attitude angle φ. The maximum displacement of the center of the rotor is e.**

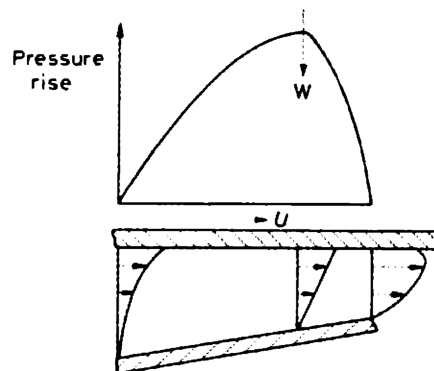


**Figure 2-13 Velocity profile of viscously dragged flow through a converging channel. The top plate is moving to the right at speed U, and pressure is generated to support the moving plate [5].**

To increase the loading capacity and stiffness, we want to maximize the bearing length to rotor diameter ratio, and minimize the gap to rotor radius (c/R) ratio. [5,9-11] However, the fabrication capability limits the length to gap ratio to approximately 30:1. Thus, the circular bearing gap has been chosen to be 10 μm wide and 300 μm deep/long.

There are three ways to implement the journal bearing. Typical choices are to use a center shaft to reduce the L/D ratio, as shown in 1st and 2nd diagram in Figure 2-14. We end up not choosing the first approach (center hole) because it increases the c/R ratio. Moreover, the rotor expansion caused by centrifugal force does not favors this design because the gap around center shaft will increase, further reducing the c/R and hurting the performance. The centrifugal force does not work against the 2nd approach in the figure (center shaft), but it was difficult to envision a suitable fabrication process, and we ended chose the edge journal bearing design (3rd diagram in the figure) and put the bearing on the edge of the rotor. This implementation translates into a very low length-to-journal-diameter ratio (L/D ratio = 0.075, most bearings have L/D ~ 1), which is also undesirable because axial leakage flows reduce the load capacity. But it is a design most compatible with available micro-machining techniques. In our design, the journal bearing diameter is chosen to match the turbine rotor size to be 4.1 mm. The chosen design was analyzed in detail by Ed Piekos using a custom SPECtral Reynolds Equation Solver, dubbed SPECTRES [8-10].

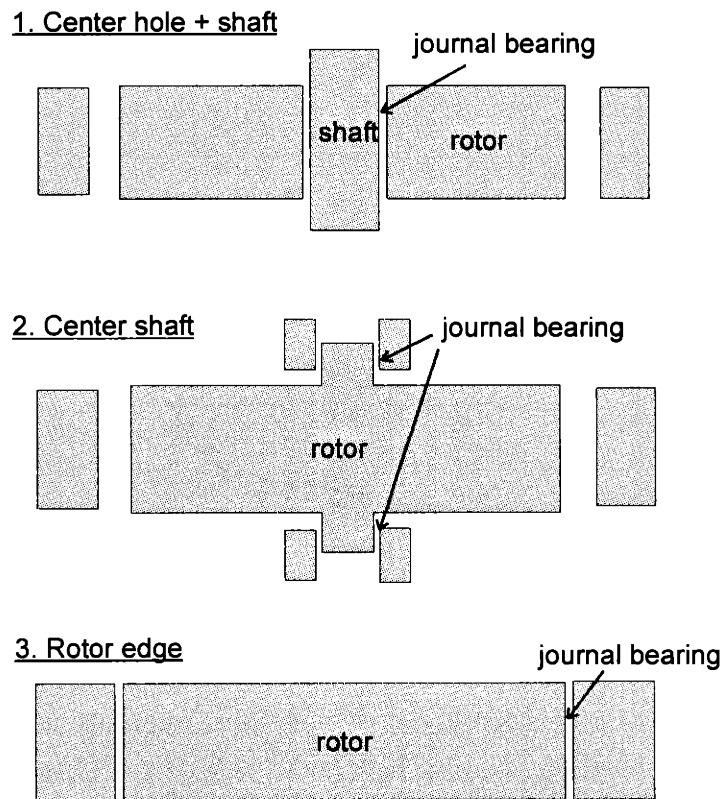


**Figure 2-14 Journal bearing location options.**

The net bearing force comes from integrating the pressure around the journal. Figure 2-15 shows the pressure distribution around a plain journal bearing. When the speed is low and the bearing is operated at low eccentricity, the pressure field is symmetric. At higher speed, the pressure increases and the pressure field becomes more asymmetrical. The peak of the pressure is also aligned closer to the load line. Eventually, if the load is too high, the required stable running gap becomes smaller than wall roughness, and the rotor will contact the wall and crash.

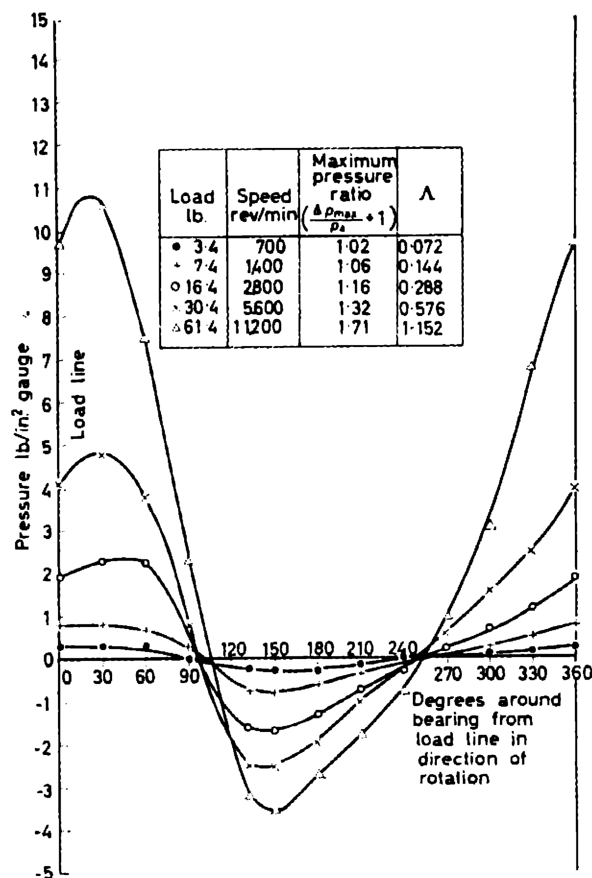


**Figure 2-15 Pressure contours around a plain hydrodynamic journal bearing with load varying from 3 to 61 Lb. [3]. The bearing diameter is 2 inch, length is 4 inch, and gap is 0.001045 inch.**

In large-scale systems using gas-lubricated journal bearings, the load is usually set by the weight of the shaft. As for the micro bearing rig, the mass of the turbine rotor is too small to establish stable operation. To generate a side load, we divide the bearing backside into three equal 120 degree sections, each leading to a pressure plenum (Figure 2-16a). Two of the sections are fed with higher-pressure air, and the other is fed with lower-pressure air. The thick arrows in Figure

2-16a shows the axial cross flow which sets up a pressure field in the journal bearing. From cross-sectional view in Figure 2-16b we can see that the bearing will see different local ambient pressures in either side, and a net force will be generated to push the rotor to the right. This is a better approach than relying on gravity for the load because the operation of the device will be insensitive to device orientation.

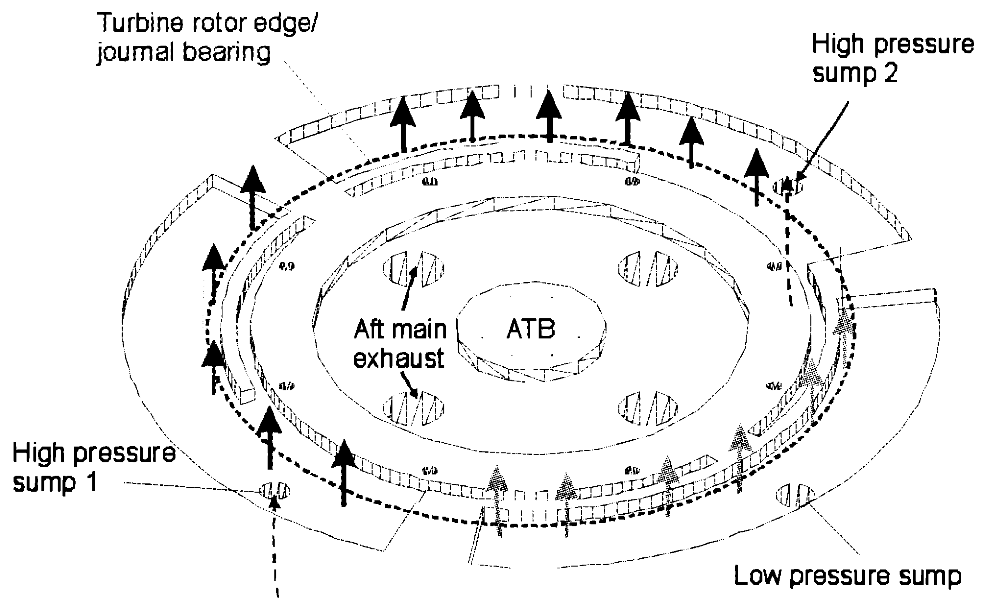


(a)

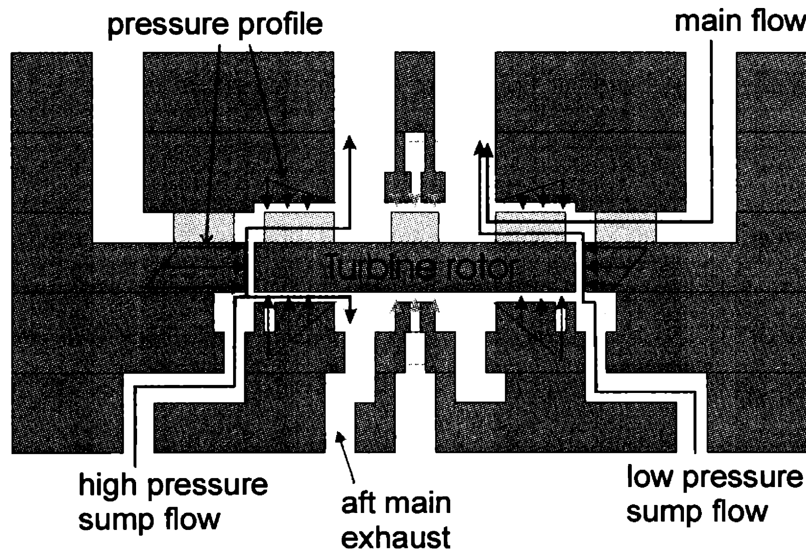


(b)

**Figure 2-16 The journal bearing sump plenums design. (a) The rotor/edge journal bearing gap overlaps with the plenums such the rotor experiences three different ambient pressures. (In practice, the two high sumps are usually set to equal pressure.) The thick arrows shows the axial cross flow path that goes through the journal bearing gap. This flow sets up a pressure field in the journal bearing to push the rotor sideways, as shown in part (b).**

High-speed bearing operation also requires a balanced rotor because rotor imbalance causes synchronous whirling (whirling frequency = rotating frequency). Once the rotor speed is higher than the bearing critical frequency, the rotor will rotate with respect to its center of gravity, not the geometric center. Therefore, the maximum operating eccentricity decreases with imbalance. Thus, keeping all other conditions the same, a rotor with imbalance would crash at a lower speed. The other problem with synchronous whirling is its interaction with the natural frequency of the system. If the designed operating speed is higher than the natural frequency of the system and the system lacks sufficient damping, each time the rotor accelerates past the natural frequency (and multiples of the natural frequency) the whirling amplitude will increase, raising the potential for a bearing crash.

Another typical mode of failure is the half-speed whirl. As explained earlier, the hydrodynamic bearing relies on the viscous pumping to generate the supporting pressures. Because the journal is sliding relative to the stationary bearing, the established shear flow in between has an average speed that is half the journal speed. If the rotor is whirling at half the rotation speed the relative speed between the journal and the fluid will be approximately zero and no pumping action will exist. At this point, the bearing loses all of its loading capacity and becomes unstable. The above qualitative explanation can be verified by looking at the individual terms of the Reynolds equation. Practically, most bearings fail before the whirling speed reaches 0.5 of the rotation speed.

To help the fabrication group understand the trade-off between bearing aspect ratio, bearing width, and bearing stability, a non-dimensional "maximum-minimum eccentricity chart" was produced by Piekos [13]. For the fabrication group, it is more convenient to directly compare the stable running gap against the bearing length and aspect-ratio, because they are the most critical parameter in plasma etch (chapter 3). It is assumed that the running-gap has to be much larger than the etched roughness of the wall to prevent wall crash. For this purpose, the author converted the non-dimensional chart (by Piekos) into a map of 'minimum running-gap' (Figure 2-17). The 'minimum running-gap', denoted by $g_o$, is defined to be the smallest distance between rotor and bearing during stable operation, assuming that lowest required side-load is applied to stabilize the rotor. In the chart, we assume a rotor diameter of 4 mm, and compare $g_o$ with the gap aspect ratio. It is clear that $g_o$ increases with aspect ratio of the bearing gap. Four different bearing length (L=150~800 μm) are also shown for comparison, and we can see that the $g_o$ increases with the length of the bearing. Using this chart, the fabrication team can optimize the

journal bearing length and aspect ratio to maximize $g_o$ according to the wall roughness associated with the chosen process.

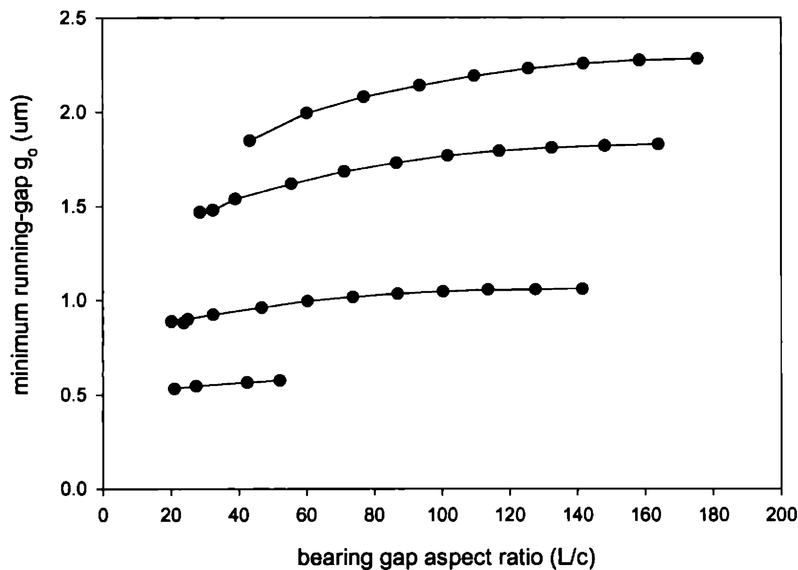


**Figure 2-17 Minimum stable running-gap vs. bearing aspect ratio – derived from maximum 'minimum eccentricity' chart from Piekos [10]. The trade-off between bearing etch, running gap, and bearing length L is clearly shown. This chart assume rotor diameter of 4mm.**

### 2.3.1 Rotor tilting balance

The three journal side-loading plenums see different pressures. If they are allowed to leak radially inward to the aft thrust-bearing exhaust, the flow would establish a pressure field that could tilt the rotor. To eliminate this problem, a tilt balance channel is designed so that there is no net torque acting on the rotor to excite the angular whirling mode (Figure 2-18). The idea is to build two C-shaped channels inside the plenums that lead to the high-pressure sumps. This will establish a symmetric pressure field and no net tilting torque will be exerted on the rotor.

### 2.3.2 Journal bearing side loading and rotor axial balance

Because of the centrifugal turbine design, the cross-sectional area of the turbine blades is 15 times larger than the thrust bearings; high load-capacity thrust bearings are needed to keep the rotor axially supported. (Figure 2-16b) However, the load capacity of hydrostatic thrust bearings is

limited by the feed pressure. It is imperative to manage the pressure acting on the back of the rotor to keep the rotor balanced axially with respect to all proposed operating protocols.

The following is done to help with the rotor axial-balance. According to calculations that assume a linear pressure drop, the inner radius of the surface facing the rotor bottom is set to be 1.465 mm. In addition, eight vent holes are also fabricated at r = 1.75 mm to reduce pressure build-up on the "generator pad" (Figure 2-18). As will be discussed in chapter 5, axial balance imposes a large constraint on the spin-testing protocols.

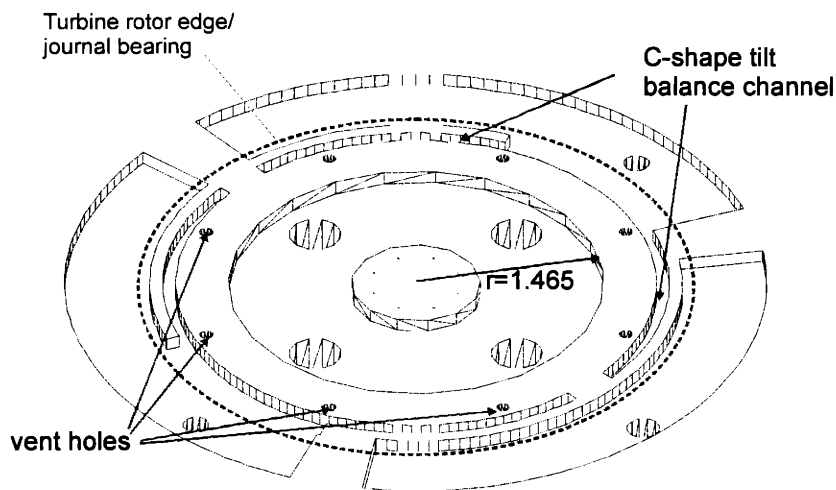


**Figure 2-18 Rotor tilt balance channel and back-side vent holes.**

### 2.3.3 Jacking ports

The experience obtained from the macro bearing rig testing shows that hydrostatic stiffness can be developed by axial through flow across the journal bearing. [12] The journal bearing gap acts as a inherent restrictor that regulates the pressure in the gap. The effect correlated well with an entrance-length model, but the associated low natural frequency was undesirable for high speed operation. To eliminate the critical frequency associated with this effect, the sump plenum was short-circuited by an instrumentation port, now called the "jacking port" instead, directly above the rotor. Cross flow is minimized once the pressure on both sides of the turbine becomes equal. This feature is also included in the micro bearing rig design. Four 250 μm diameter ports positioned above the journal bearing gap are designed and built to be connected to the sumps if needed. They are conveniently used as a viewing port for inspecting the completion of the journal bearing etch (chapter 3).

### *Section 2.4 Summary*

In this chapter, we reviewed the basic operating theory and design parameters of the key components of the micro bearing rig. We started with a discussion of the micro bearing rig component design, and a short summary of the radial inflow turbine design followed. The hydrostatic thrust bearing design issues were then presented. The chapter concluded with an overview of the hydrodynamic journal bearing design considerations and design parameters of features that are included to stabilize the bearings.

In the next chapter, we will switch the topic to show the fabrication process used to realize this device and the related challenges.

### *Section 2.5 References*

[1] Drela, M., "Two-Dimensional Transonic Aerodynamic Design and Analysis using Euler Equations," February 1986, thesis, MIT.

[2] Youngren, H., "Analysis and Design of Transonic Cascades with Splitter Vanes," March 1991, M.S. thesis, MIT.

[3] Mehra, A. "Computational Investigation and Design of Low Reynolds Number Micro-Turbomachinery," SM thesis, Department of Aeronautics and Astronautics, Massachusetts Institute of Technology, Cambridge, MA, June, 1997.

[4] R. Bassani and B. Piccigallo, "Hydrostatic Lubrication," Elsevier, 1992, Chapter 2.

[5] Grassam, N.S., Powell, J.W., "Gas Lubricated Bearings," London Butterworths, 1964.

[6] Opitz H., "Pressure Pad Bearings," Proc. Instn. Mech. Engrs., 182, 3A (1967-68) pp. 100-115.

[7] Mechanical Technology Incorporated, Latham, NY.

[8] Mur Miranda, J. O. [1997]: "Feasibility of Electrostatic Bearings for Micro Turbo Machinery," M. Eng. Thesis, MIT Department of Electrical Engineering and Computer Science, December, 1997.

[9] Piekos, E., Orr D.J., Jacobson, S.A., Ehrich, F.F. and Breuer, K.S. [1997]: "Design and Analysis of Microfabricated High Speed Gas Journal Bearings," AIAA Paper 97-1966, Snowmass Village, CO, June, 1997.

[10] Piekos, E. , Breuer, K. S., "Pseudospectral orbit simulation of nonideal gas-lubricated journal bearings for microfabricated turbomachines," to be published in Journal of Tribology.

[11] Piekos, E., " Numerical modeling of gas-lubricated journal bearing for micro fabricated turbomachines," Ph.D Thesis, MIT, 1999.

[12] Orr, D.J. "Macro-scale investigation of high-speed gas bearings for MEMS devices." Ph.D thesis, MIT, 1999.

# Chapter 3

# Fabrication Process

This chapter starts with a description of the established fabrication process for the micro bearing rig. Followed by discussion about key challenges that were encountered and overcome along the development process.

### *Section 3.1 Fabrication process flow*

Based on the design shown in the previous chapter, we realized that a successful build of the micro bearing rig required integration of several state-of-the-art technologies. It appeared that a combination of multiple-wafer bonding and deep silicon etching were the core technologies to be developed. However, because the novelty of the process, it was difficult to yield any immediate result if we tried to develop and integrate all the technologies at the same time. We decided to gain knowledge incrementally by first built a prototype by combining known techniques while seeking the best fabrication process and allocating resources.

The prototype was built with a combined die/wafer level process. (appendix A) We found a few design flaws and learned several lessons from the fabrication and testing of this prototype. First, the original packaging design was leaky, preventing proper pressure setups at each port. Second, the device tolerance was very poor, and the yield was low, both results from the fact that die-level processes require hand assembly. The rotors did spin, but the basic testing system could not capture the speed data, and we learned that we had to improve the instrumentation.

Learning from the first generation prototype, we established a set of strategies that guide the process development:

1. Step-by-step dimensional inspection and short-loop process development/improvement.
2. Assemble the whole device at the wafer level.
3. Use fusion bonding instead of low-temperature bonds to ensure high temperature compatibility and good sealing.
4. Keep wafers independent by postponing bondings as long as possible. Therefore, a defective wafer can be removed from the inventory without affecting the other four wafers.
5. Design packaging in parallel with the fabrication process to ensure compatibility.
6. Simplify the process as much as possible to reduce development time and enhance the chance of producing completed devices (even if they may need further improvement). Development time is assumed to correlate with by mask count, and the number of DRIE/bonding steps.

A redesign was initiated to fix the problems encountered. The packaging scheme was redesigned to incorporate o-rings to eliminate leaks. The minimum size of commercially available o-rings ( 0.057 inch =1.45 mm) set the die size to 1.5 $cm^2$, resulting a yield of 12 devices per 4" wafer. A full wafer-level process was designed using silicon fusion-bonding. The forward thrust bearing feed line was isolated from the main turbine air. After intensive process tuning and development, we established a process to build the spinning micro bearing rig. This process is presented in the next section.

### 3.1.1 Full wafer-level process

The full wafer-level process flow involves the use of 16 masks and 9 deep silicon etching steps on 5 wafers. A schematic illustration of the process is shown in Figure 3-1 [1,2]. A step-by-step process description is included in the appendix A. The fabrication starts by etching shallow global alignment marks on both sides of all wafers with the help of infrared alignment. Next, a shallow pattern is etched in the $2^{nd}$ wafer (called the forward endplate, FEP) to define the bearing gaps, typically 2 μm wide. The accuracy of the etch depth has a strong influence on the performance of the thrust bearing, and a smooth and flat etched surface is also critical. A second shallow etch of 4-8 μm defines the blade tip clearance in the same wafer. In order to get a flat smooth etched surface, we use a $HBr/Cl_2/NF_3$ magnetically coupled plasma in an Applied

Materials AME5000 magnetron plasma etcher. The AME5000 produced repeatable results with tolerance of less than 0.1 μm.

The blade tip clearance etch is followed by a deep silicon etch on the opposite side of the wafer to a depth of 350 μm to define the thrust bearing plenum and main air distribution plenum. Next, a 0.1 μm sacrificial PECVD oxide layer is deposited. Based on our short–loop study, hydrogen-rich PECVD oxide was shown to release hydrogen during the deep RIE and reduce the etching rate significantly. Therefore, the deposited oxide is densified at 1000°C in nitrogen for an hour to reduce the hydrogen content. The purpose of depositing a protection layer on the deep-etched side is to protect the surface from being etched by fluorine once the wafer is etched through in the next deep RIE.

Accordingly, the 2nd wafer is inverted, a lithography operation is performed, and the wafer is reversibly attached to a quartz carrier wafer using a photoresist bond. Next, a 2nd deep etch is performed to etch through the wafer to the deep features on the front surface. After etching, the handle wafer is released with a piranha[2]/acetone rinse, and the device wafer is further cleaned by $O_2$ plasma ashing. This 2nd wafer (FEP) is fusion bonded to the 3rd wafer, called the rotor plate (RP), which has been etched to a depth of 200 μm to define the turbine blades and the turbine inlet guide vanes. Following a critical photolithography step on the RP to define the journal bearing, the RP/FEP pair is again attached to a quartz carrier wafer and then deep etched to fully define the rotor.

In principle, the rotor is free at this point. However, sacrificial tabs have been created in the process of fabricating the FEP which bond to the rotor, holding it in place. These tabs are removed by laser-assisted etching after the final bonding, at which point the rotor is contained by the 2nd and 4th wafer.

The process proceeds with the fabrication of the 4th wafer (Aft End Plate, AEP), which is similar in process to the FEP, a 1st wafer (Forward Foundation Plate, FFP) and a 5th wafer (Aft Foundation Plate, AFP), which provide fluidic interconnects. The AEP and AFP are fusion bonded together, after which this pair is bonded to the RP/FEP pair, and then bonded to the FFP, completing the stack.

---

[2] 3:1 $H_2SO_4/H_2O_2$ mixture.

The bonded 5-wafer stack is sawed into 1.5 $cm^2$ dies and immersed in diluted HF to remove any surface oxide that will prevent proper etching during the laser assisted etching (LAE). The sample is positioned in a chlorine chamber during LAE, and the laser beam heats the sacrificial tabs that hold the rotor. [3] The heated silicon reacts with chlorine to form volatile silicon tetrachloride, and the tabs are selectively removed as the laser is scan over them. The rotor is freed once the tabs are completely removed, and this completes the micro bearing rig fabrication process.

Figure 3-2 shows an SEM of the cross-section of a fabricated FEP/RP pair, and we can see the thrust bearing plenum in the middle and the main air distribution plenum near the periphery. A close-up view of the thrust bearing plenum is shown in Figure 3-3. The 16 μm diameter thrust bearing capillary restrictors are illustrated in the picture. Because the die cutting process create particles and jagged edge, the 1 μm bearing gap does not look uniform at this scale. Higher magnification SEM viewing perpendicular to the cross-sectional surface indicates a uniform gap width.

The next figure shows a bonded AEP/AFP pair, the aft thrust bearing plenum and aft main exhaust flow path are clearly shown. Figure 3-6 shows a completed bonded 5 wafer stacks with related depth measurements. One can see the achieved DRIE depth control. All the errors in etch depths are less then 10%, which is acceptable. The internal flow paths are shown in the next figure.

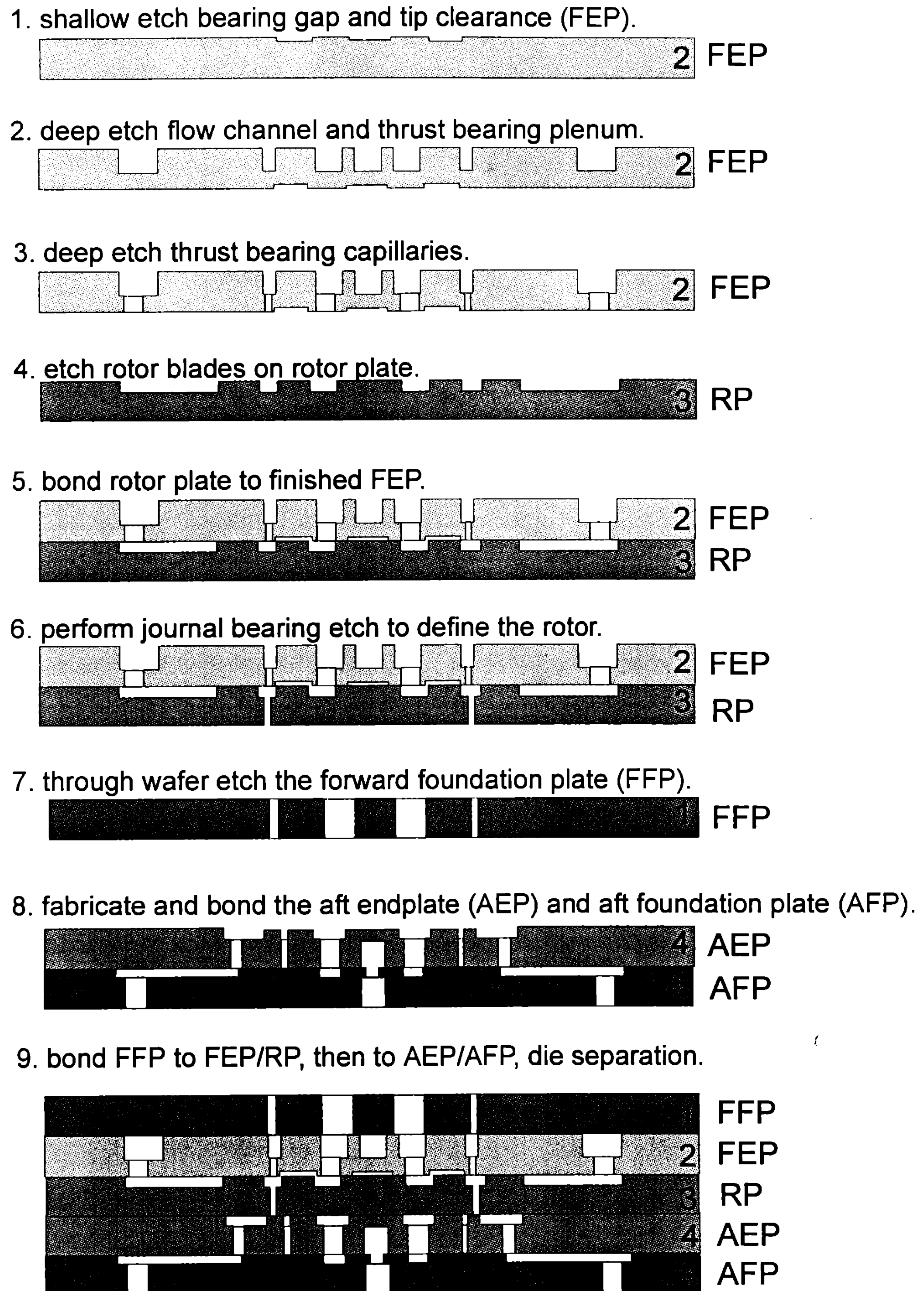


**Figure 3-1 Micro rig fabrication process.**

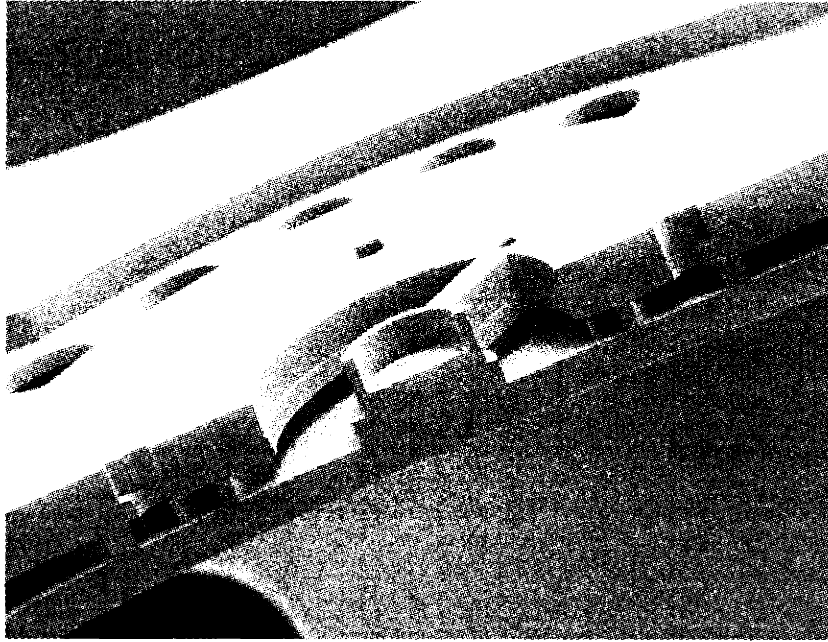

**Figure 3-2 Bonded 2nd-3rd wafer pairs.**

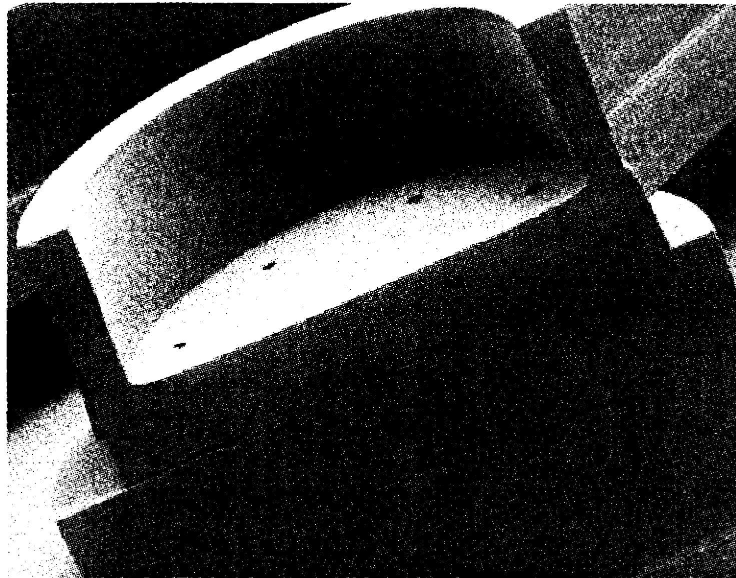

**Figure 3-3 Close-up view of thrust bearing plenum. Thrust bearing orifices are also shown. The diesawing process chips the edge of the thrust bearing pad and makes the 2 μm bearing gap more visible.**

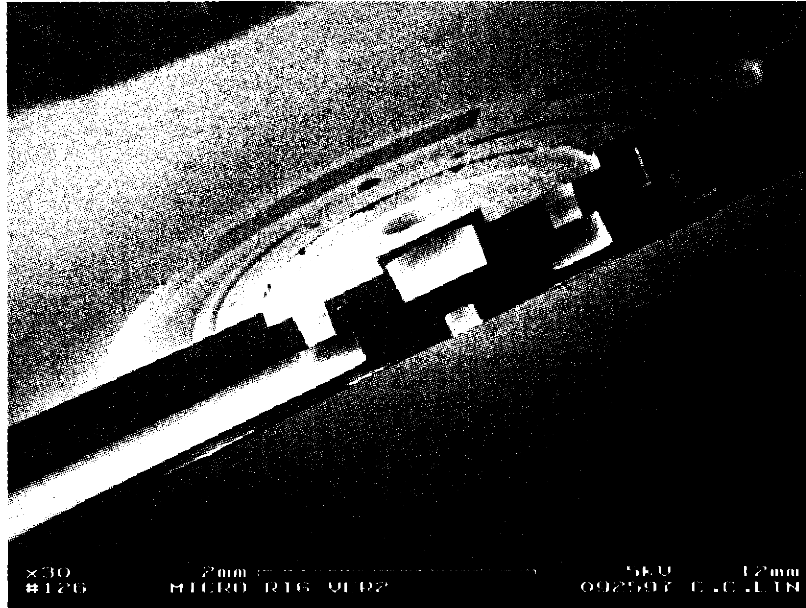

**Figure 3-4 Fabricated 4th/5th bonded wafer pair.**

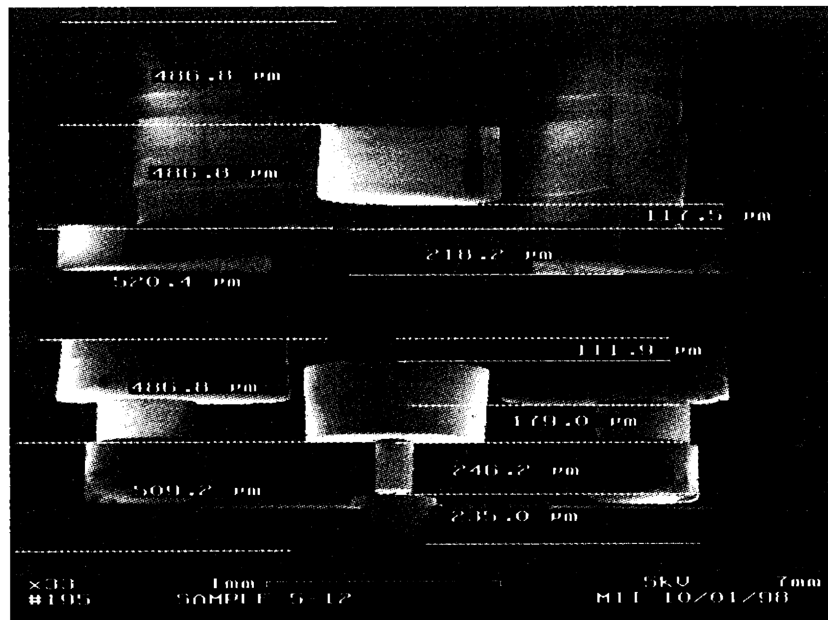


**Figure 3-5 Cross-sectional view of micro bearing rig showing the depths measurements of each deep etch.**

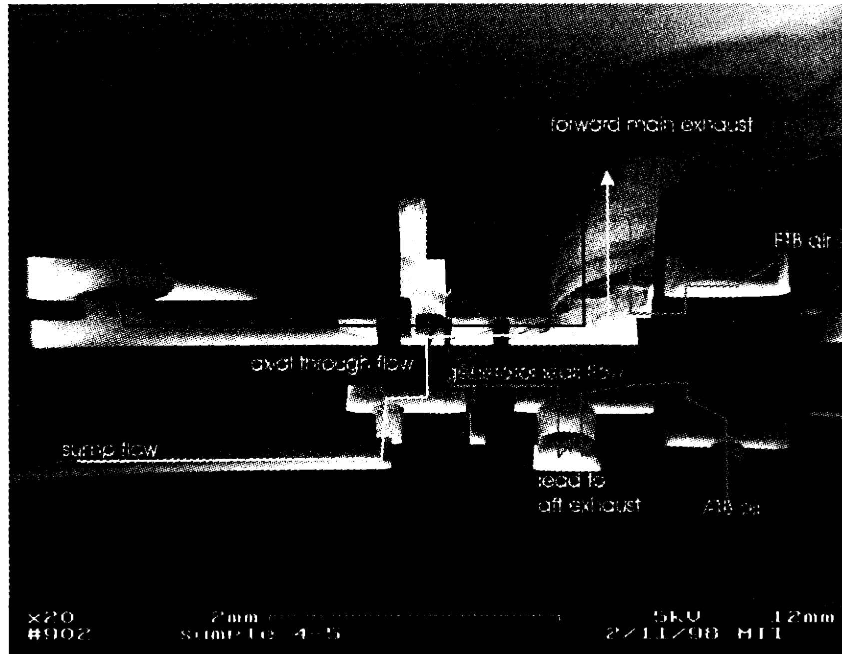


**Figure 3-6 Cross-sectional SEM of micro bearing rig showing the internal flow paths.**

## *Section 3.2 Fabrication techniques and challenges*

Due to the complexity of the micro bearing rig, there were quite a few "non-traditional" steps which were difficult and needed development. These included the deep-RIE development, aligned etching from both sides of the wafer, multiple wafer bonding, and laser-assisted etching. They are discussed in the next sections.

### 3.2.1 Deep RIE optimization:

In a traditional reactive ion etcher, in order to promote etch anisotropy, the plasma chemistry is carefully chosen to induce an etch-hindering polymer formation on the trench sidewalls. The physical attack of ion bombardment increases the etch rate by orders of magnitude. The bottom of the trench therefore etches much faster and an anisotropic trench profile is created. The Bosch process was invented to tackle this problem from a different angle. Contrary to typical reactive ion etching processes, the core of the Bosch process consists of two plasma cycles instead of one. The process iterates between an etching cycle using pure fluorine-based chemistry ($SF_6$) and a polymer passivating cycle utilizing $C_4F_8$ to deposit a Teflon-like $x(CF_2)$ films (Figure 3-7). During the etching cycle, the passivating film is preferentially removed from the bottom of the

trenches due to ion bombardment, while preventing etching of the sidewalls. Therefore, the etch advances in the direction along the ion trajectory (perpendicular to the wafer). The subsequent passivating cycle coats the newly created etched surface and replenishes the remaining coating. The success of the process hinges upon a proper balance between the etching and passivating cycles. While incomplete passivation results in a reentrant or isotropic trench profile, excessive passivation will create grassy surfaces or a complete stop of the etching. One feature of this process is the vertical striation mark produced on the wall (Figure 3-8) due the cycle switching.

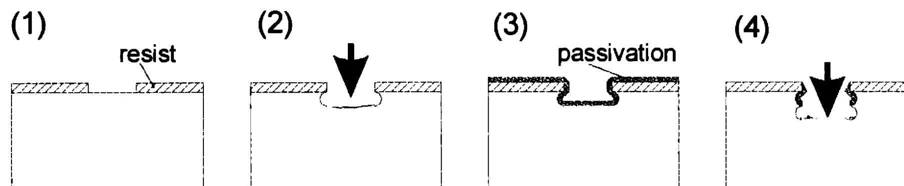


**Figure 3-7 Bosch process.**

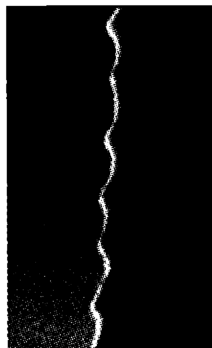

**Figure 3-8 Trench sidewall showing vertical striation marks (scalloping) due to the process. The vertical period is a function of cycle duration and is of the order 1 μm.**

Although the Bosch process can improve the anisotropy of the etch dramatically, it still requires a high density plasma to achieve high etch rates. Recently, ECR (electron cyclotron resonance), magnetron, and ICP (inductively coupled plasma) systems have been designed to produce low-pressure confined high-density plasmas [4]. The approach using an ICP plasma source integrated with a Bosch-patented process has been investigated with a Surface Technology Systems etcher for the past 4 years [5-6]. The etcher is shown in Figure 3-9. This approach has proven to be a reliable technology for etching deep high-aspect-ratio features. Silicon trenches with aspect

ratios of 20:1 can be achieved using a photoresist mask (Figure 3-10). The etch rate is typically about 2~3 microns per minute, which is more than 5 times higher than with conventional plasma etching, and the selectivity to photoresist is extremely high, typically 75:1.

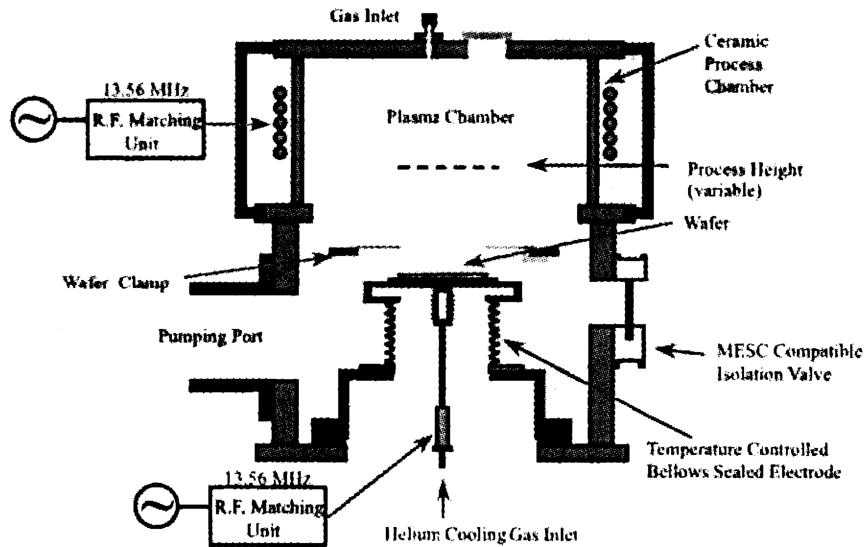


**Figure 3-9 ICP deep RIE etcher made by Surface Technology Systems (STS).**

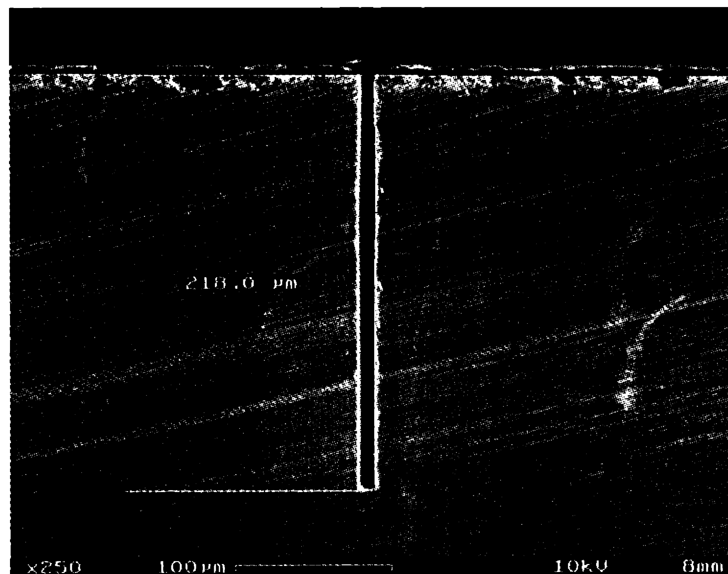


**Figure 3-10 A high aspect ratio etch performed by STS ICP, the gap width is 10 µm.**

### DRIE artifacts

Although the as-shipped etcher came with excellent capabilities in terms of etch rate and surface smoothness for deep etches of large features, several artifacts were discovered in our early etches.

The first problem, called the 'footing effect', is caused by charging at buried dielectric interfaces. Once the etch reaches the dielectric, the ions in the plasma will start charging the dielectric. Therefore, the ion trajectory is deflected sideways, causing the sidewall to be severly attacked. This presented a serious problem for users that etch to a burried dielectric. In our case, we were using oxide as a sacrificial layer for bonding a handle wafer to the device wafer during a two step through-wafer etch. The sacrificial oxide charged up and caused serious damage to the blade tip (Figure 3-11).

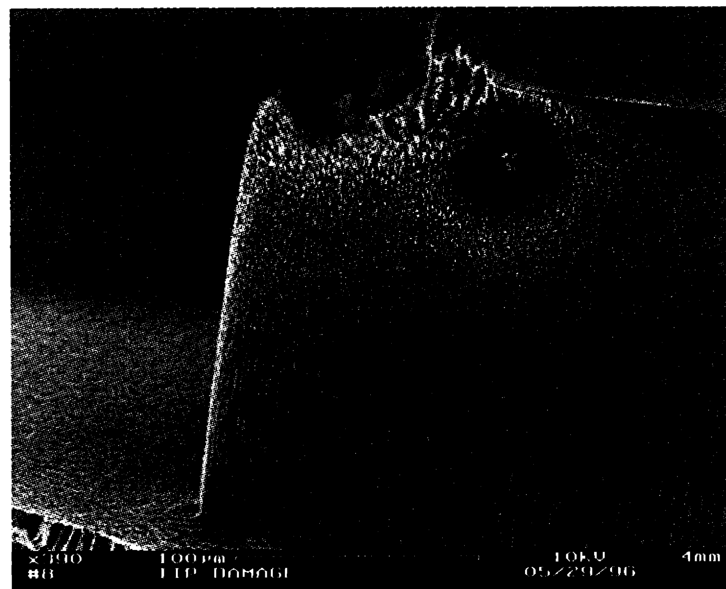

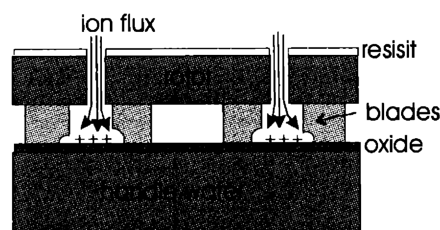


**Figure 3-11 Damaged turbine leading edge due to the footing effect. The blade is attacked during the 2nd deep etching that defines the journal bearing. During this etch the turbine is bonded to an oxidized handle wafer. When journal etch breaks through, the injected ions accumulate at the oxide interface and deflect the ions sideways to attack the turbine tip.**

This footing effect can be solved by many ways. At the beginning, we found quick solution by increasing the distance between the blades and the journal bearing gap from 50 μm to 100 μm. In addition, we also improved the resist linewidth control to reduce the required overetch. The combination of these solved the problem. This problem can also be reduced by etching process optimization, and the details will discussed in the next section.

The complexity of the proposed design requires us to etch from both sides of the wafer. It should be noted that because the dimensions of the features on both sides of the wafer are usually different, two problems were discovered depending on whether the larger features were etched first. If large features are etched first (e.g. the turbine/bearing etch), localized damage will appear at the corner where the narrower feature breaks though and meets the larger feature. This effect is due to bombardment of reflected reactive radicals from the back surface. The lower-left corner of the SEM in Figure 3-11 shows that shallow damage on the edge of the rotor. On the other hand, if the etch order is reversed, localized grassy needles are usually discovered at the same location (Figure 3-12). This is believed to be initiated by the remaining sidewall passivation from the first deep etch. If not completely removed, the passivation film protect the sidewall during the $2^{nd}$ deep etch. Performing an oxygen plasma clean to remove the passivation after the $1^{st}$ deep etch will significantly reduce this problem. Another solution is to perform a short fluorine-based isotropic etch to remove the needles afterward.

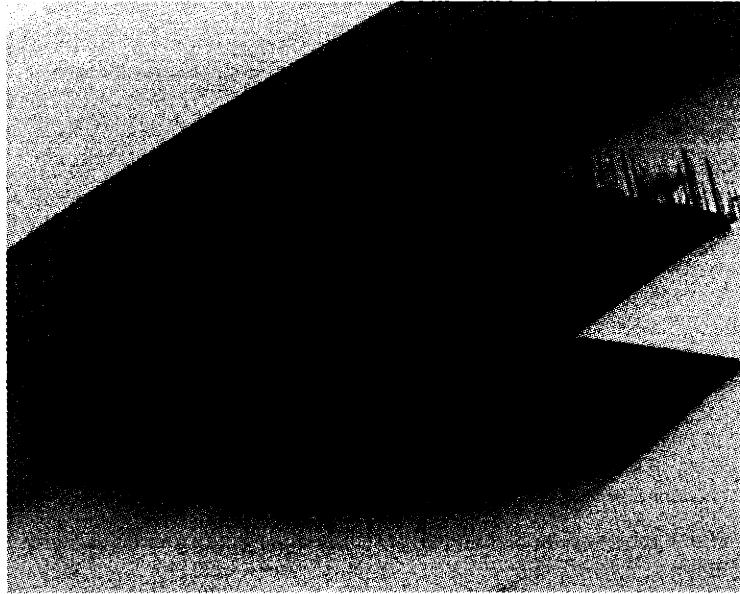

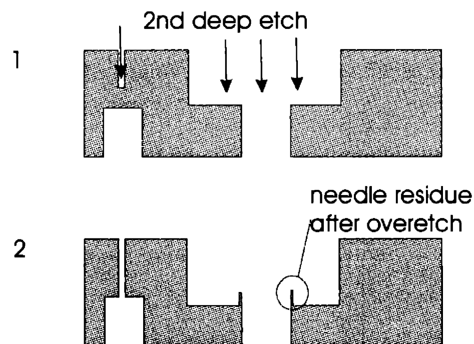


**Figure 3-12 SEM showing the needle-like residue at the interface of two overlapping deep etches (etched from both sides). These needles are usually about 1-2 micron wide, and their height depends on the length of the overlapped region. These needles could be eliminated by a short isotropic etch and reduced by minimizing overetch.**

There is one other issue that is consistently observed and related to the field distortion. Called 'pitting effect; an accelerated etch is always observed beside a feature that has a sharp corner (Figure 3-13). This is very undesirable because a crack could propagate from the corner when the part is stressed. We learned that rounding off the feature to a greater than 10 μm radius was sufficient to eliminate the problem.

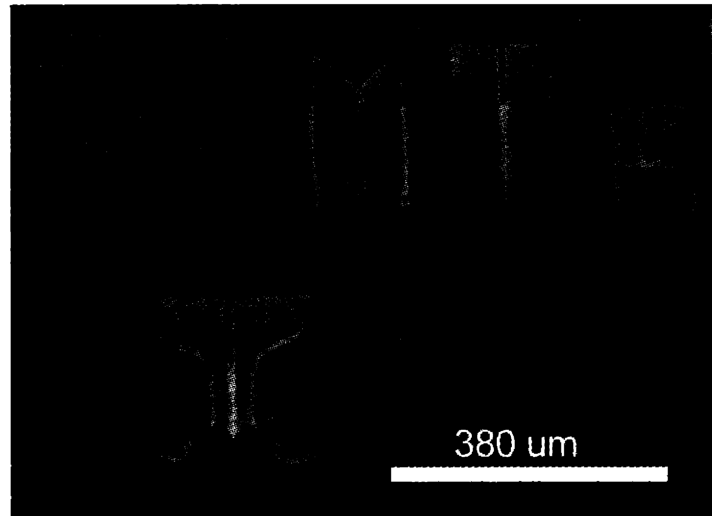


**Figure 3-13 SEM showing the pitting effect. An accelerated etch pits the root of sharp features and dig into the surface. This is very undesirable because of the stress concentration problems. The picture also shows the problem of having a reentrant profile that gradually remove the narrow features (linewidth=10 μm, depth=300 μm).**

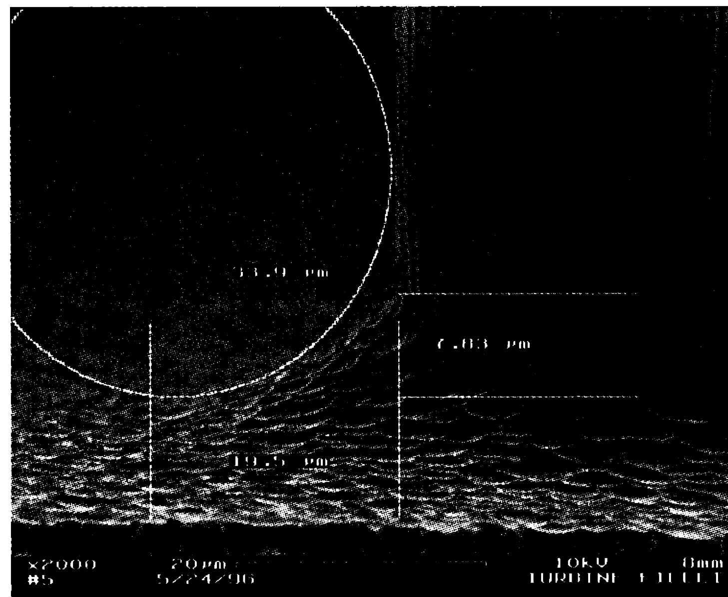

**Figure 3-14 SEM showing the root fillet of the turbine blade leading edge.**

The turbine blade is highly stress due to centrifugal force during spinning, and the root of blade experiences the highest stress. It is very important to reduce stress concentrations at the root by

producing a smooth fillet. Figure 3-13 shows the root of the etched turbine leading edge. The existence of horizontal and vertical striations indicates that the process needs further improvement. The fillet radii are directly controlled by the plasma etching conditions. Further increase in the fillet radii can raise the failure stress levels to allow for higher rotation speed or taller blades operate at same speed. [7] Either improvment could further increase the maximum power that can be produced by each device. [8]

### Design of Experiment study

Although changing device design can solve some of the issues, improved recipes can relieve those design constraints. Moreover, successful fabrication of the micro turbine requires us to push the limit of the DRIE machine further. In particular, the specific requirements for the micro bearing rig fabrication include the following:

1. A 10 μm wide, 300 μm long (30:1 aspect ratio) trench etch that defines the journal bearing gap. Minimizing tapering and wall roughness are necessary to improve the performance.

2. Elimination of sharp morphology changes and rough surfaces around high stress areas such as the turbine blade root to prevent fracture due to stress concentration.

3. Anisotropy control (vertical sidewall) for through-wafer etches (e.g., FFP) or etches exceeding 300 μm.

4. Accuracy and uniformity in etch depth and width control.

In order to achieve the dimensional control that is required to build a working device, a thorough understanding of the role of each control variable is necessary. Therefore, a Design of Experiment (DOE) analysis based on response-surface models was led by Dr. A. Ayon at MIT to improve the ICP etching process [5,6,9,10]. There are eleven total control variables that can be adjusted to optimize the etch process, including the duration and overlap of and between each cycle, the flow rate of the etching and passivating gases, the coil and platen power for each cycle, and the setting of an automatic pressure control (APC) valve (Table 3). We can optionally set the pressure for both the etching and passivating cycles and allow the APC valve to self-regulate according to mass flow controller (MFC) feedback. Practically, though, since the cycle duration is usually

around 10 seconds and it take seconds for the APC to reach steady state, a single fixed APC setting is usually used and the chamber pressure is indirectly controlled by manipulating the gas flow rate. In addition to chamber pressures, processing observables include the power and flow rate readout, and the AC/DC bias. The output parameters that users are really interested in are etch rate, selectivity, uniformity, surface roughness and anisotropy with respect to different geometric factors such as feature width, shape and total exposed area. 45 experiments were run to correlate these variables.

| Control Variables | Plasma observables | Process results | Geometric factors |
|---|---|---|---|
| Etch:<br>Coil / platen power,<br>Flow,<br>Cycle time overlap.<br>Passivation:<br>Coil / platen power,<br>Flow,<br>Cycle time / overlap.<br>APC angle.. | Chamber pressure,<br>Matching circuit load/tune,<br>AC/DC bias for etch /passivation cycles,<br>Chamber temperature. | Etch rate,<br>Selectivity,<br>Uniformity,<br>Anisotropy (trench profile),<br>Surface roughness,<br>Local damages. | Line-width,<br>Trench aspect ratio,<br>Total exposed area. |

**Table 3 Parameters essential for ICP time-multiplexed deep-RIE.**

Some of the findings from these experiments are consistent with the physics of etching and previous work. For example, we know that the etch rate increases with etching gas flow rates. Also, pressure increase will promote isotropy in profile. This is because the ion energy goes down with increasing pressure, causing reduction in both sheath width and electrode bias. If we increase the platen power, the concentration of ions and reactive neutrals will increase, as well as ion directionality. Anisotropy is therefore enhanced, although the increase in ion bombardment causes a reduction in selectivity.

If we summarize the results from the response surfaces, we can conclude the following:

1. The etch rate increases with etch platen power, etch flow rate, pressure reduction, and reduction in passivating flow rate and cycle time.
2. The selectivity increases with lower pressure as well as etch cycle duration.
3. The uniformity increases with lower pressure and has a strong dependency on flow rate.
4. The anisotropy increases with etching and/or passivating platen power as well as etching and/or passivating flow rate.
5. The footing effect is reduced with increasing flow rate but uniformity and anisotropy will suffer.

### Journal bearing etch improvement

Based on the DOE study, short-loop optimization was initiated and several recipes were developed for different purposes as listed in the appendix. The most difficult process developed is the journal bearing etch. The difficulties arose from the required high aspect ratio plus the insufficient heat dissipation, caused by the buried deep cavities and quartz handle wafer layer. Due to design constraints, we needed to etch 3-level (including handle wafer) bonded stacks during bearing etch, and lack of proper wafer cooling affected etching result. The solution required a combination of an improved process recipe with thick-resist photolithography. (The author would like to acknowledge helps from R. Khanna on wafer processing.)

Because the processing results depend on the geometry of the etching mask, optimization of the masking scheme is as important as the etching conditions. Soft masks (photoresist) are most commonly used, while hard masks ($SiO_2$) and composite masks (Figure 3-15) are used to define narrow (<10 μm) and deep (>100 μm) etches if necessary and to battle selectivity problems caused by insufficient heat dissipation in etching multiple bonded stacks.

We found that for patterning high aspect ratio features, it is necessary to:

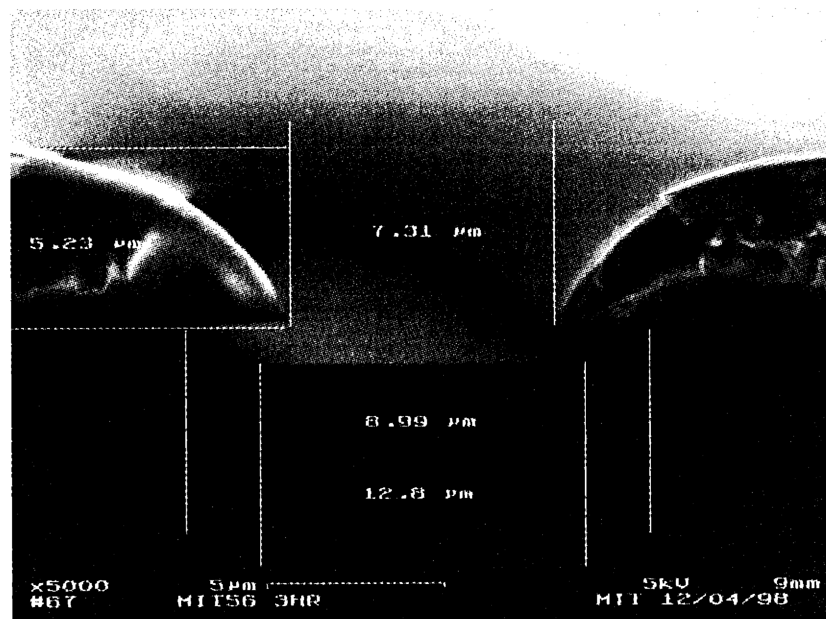


**Figure 3-15 Composite resist oxide mask on top of silicon. A one micron oxide was wet patterned using the 5.2 μm photoresist. This mask was used for the etches shown in Figure 3-19 and Figure 3-20. It was concluded that the extra oxide layer did not improve the trench profile.**

1. Minimize the waviness that causes problems of line-width variation and early resist breakdown. The micro loading effect causes the etch rate to reduce quickly with the gap when the gap becomes smaller than 10 μm. When etching high aspect ratio structures with such small linewidths, a one micron mask variation can translate into tens of microns of depth variation. An undesirable extended over-etch then become necessary to ensure completion of narrow feature etches. This is improved by using an optimized coating process that reduces the waviness of the thick resist (AZ4620).

2. Minimize re-flow of resist sidewall, which causes erosion at the entrance section of the trenches when the resist at the resist-substrate interface recedes as the etching progresses. The reflow is significantly reduced when postbaking the wafer at the 90°C, shown in Figure 3-16 as compared to Figure 3-15 which is baked at 110°C for 30 minutes. There is no evidence of any selectivity reduction due to the baking temperature change. The erosion reduces the trench verticality by producing tapering (Figure 3-17).

Two recipes have been used recently to produce high-aspect-ratio (>20:1) trenches. (Table 4) It was discovered that a direct reduction of pre-etch resist opening does not improve the anisotropy of the bearing etch. With the same recipe, the etch rate drops significantly when the critical dimension reduces. At the same time, the run out (etch in the direction perpendicular to the trench) can also increase. Figure 3-18 and Figure 3-19 show the result of two different etches with the same recipe (fixed time) but different initial mask opening and mask. Figure 3-20 shows another run with smaller gap and an increase of 50W of coil power (increasing etch rate). From these figures we can see that the etching rate continues to drop with the initial dimension, but that the final gap doesn't decrease further when the CD changes from 9 to 7 μm. Moreover, there is an increasing trench tapering that is related to the etching time and the pre-etch resist profile

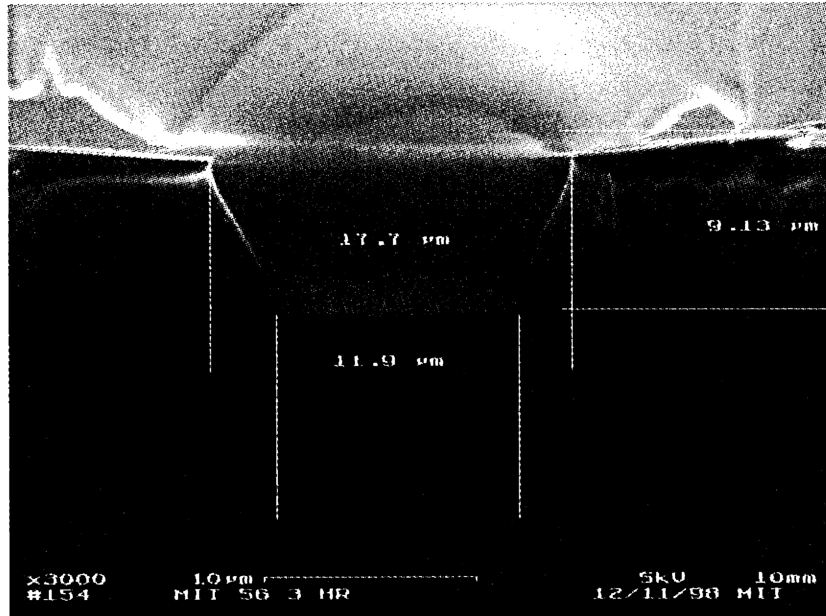


**Figure 3-16 Resist profile after 30minutes hardbake at 90C.**

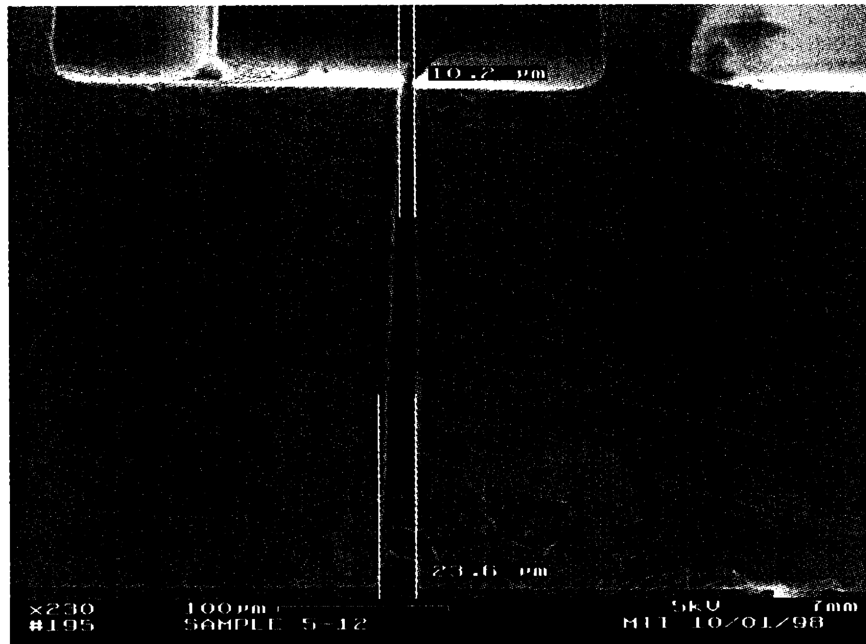


**Figure 3-17 Tapered journal bearing etch (the etch starts from the bottom). We believed that the taper is caused by significant erosion of the reflowed resist sidewall when etching bonded wafers.**

| Recipe # | $SF_6$ flow (sccm) | $SF_6$ time (sec) | $SF_6$ overlap (sec) | $C_4F_8$ flow (sccm) | $C_4F_8$ time (sec) | APC angle | Etch coil power | Etch platen power | Pass platen power |
|---|---|---|---|---|---|---|---|---|---|
| 56 | 105 | 14 | 0.5 | 40 | 11 | 65 | 800 | 12 | 6 |
| 59 | 105 | 14 | 0.5 | 40 | 11 | 65 | 750 | 12 | 6 |

**Table 4 Recipies used to produce trenches in the next two figures.**

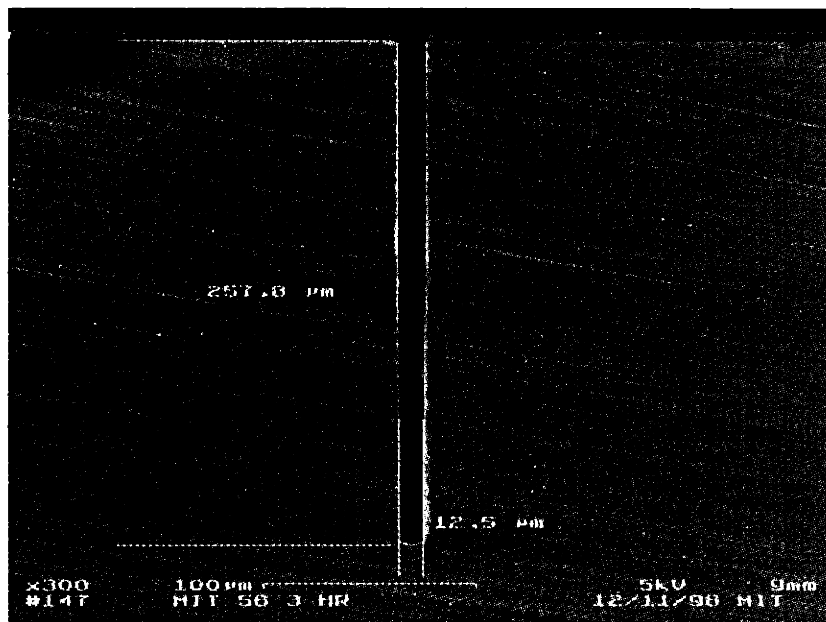


**Figure 3-18 MIT 56 3 hours. Original resist mask opening is 11 μm.**

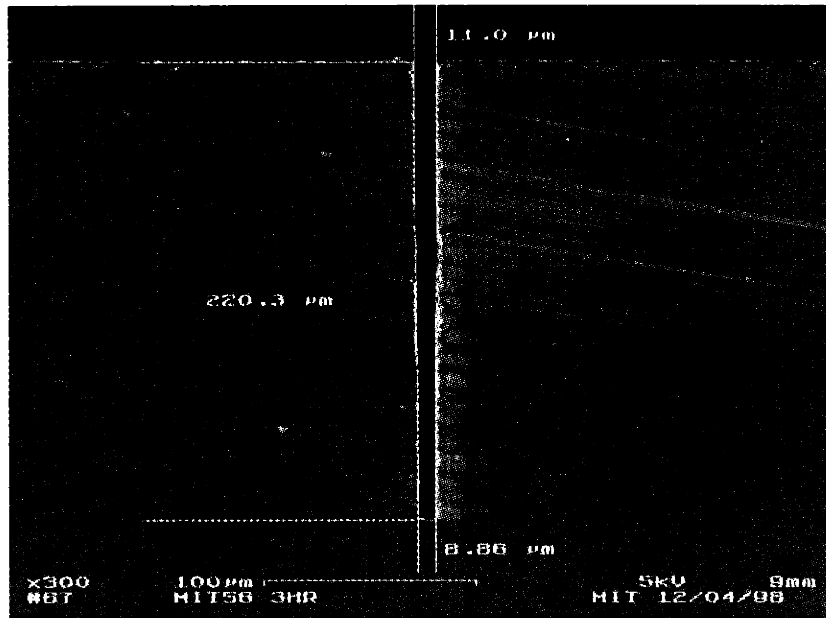


(a)

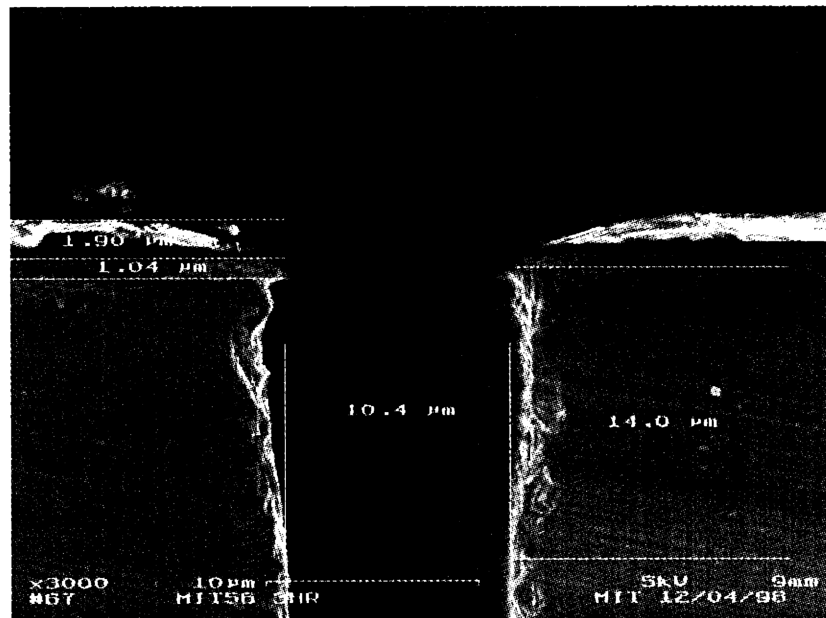


(b)

**Figure 3-19 Trench profile after 3 hours etch of recipe MIT 56. With composite mask originally defined as 9 μm, the etch rate improves significantly and the erosion problem is reduced due to the reduction in etch time.**

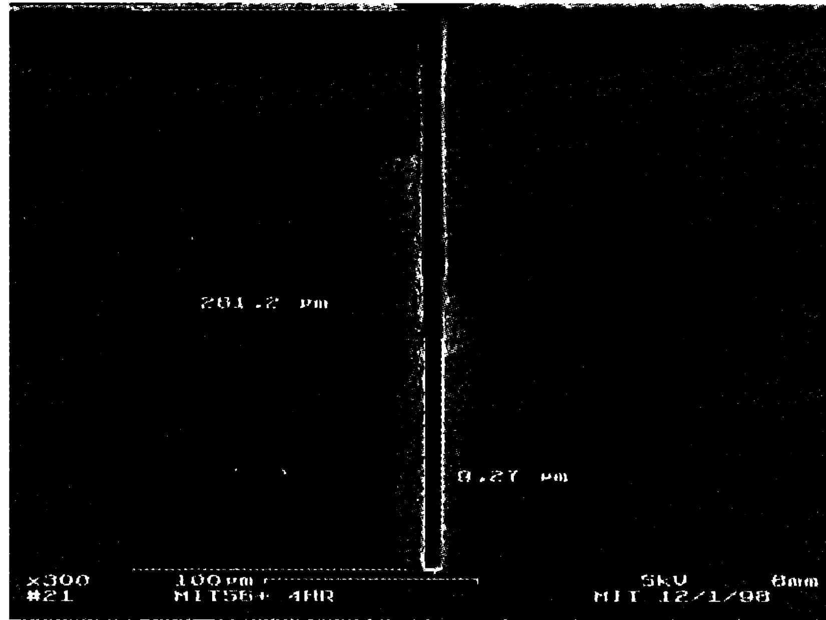


(a)

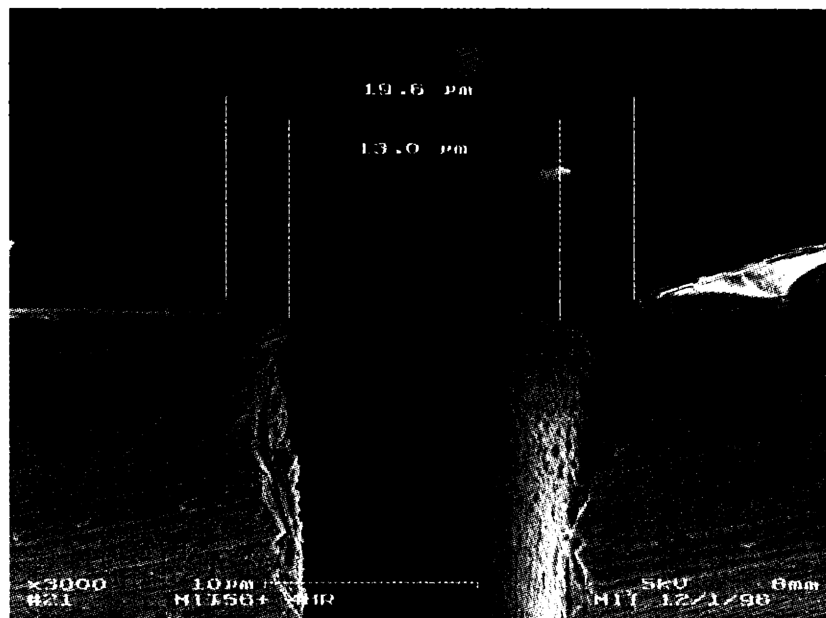


(b)

**Figure 3-20 (a) Deep etched trench with MIT recipe 59 for 4 hours. The etch is patterned with a resist/oxide composite mask with an original opening of 7 µm. (b) The mask profile after etching, It is clear that the edge has been significant eroded and bearing gap is widened. The surface near the opening is very rough due to mask erosion and ion impingement.**

### Aligned two-sided wafer etching

The concept of two-sided wafer etching is illustrated in Figure 3-21. We start by performing a 1st deep RIE that etches half way into the wafer. Then the resist mask is stripped and the wafer is cleaned using a 3:1 sulfuric acid/hydrogen peroxide mixture (piranha) followed by oxygen plasma ashing. Wafer surface protection in this process is crucial to prevent both contamination and physical damage. Therefore, a sacrificial oxide is deposited on the etched surface in the next step. The layer prevent the surface from being etched during the 2nd deep etch once two deep features connect.

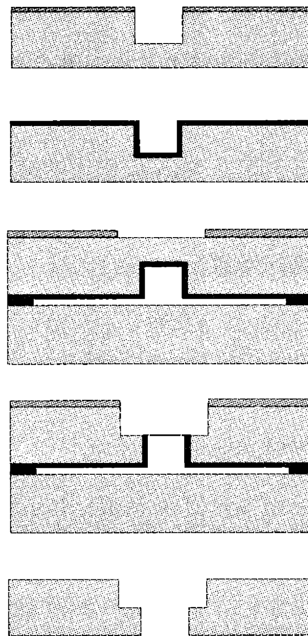

**Figure 3-21 Multiple wafer aligned etching/bonding protocol.**

In the next step, the wafer is flipped over and the backside is patterned. The features are aligned to the global alignment marks that were infrared aligned to the other side. Then the wafer is reversibly attached to a handle wafer to prevent He leakage into the chamber upon etching through the wafer, as discussed next.

With the high coil power (typically 600-800 W) in the ICP system, the ion flux into the wafer exceeds $1 mA/cm^2$ [4], making it critical to cool the wafer to prevent resist burning. In the STS system, this is achieved by a helium flow that blows on the backside of the wafer during etching.

This presents a problem for the through-wafer etches because helium will leak into etching chamber when a single hole is etched through and extinguish the plasma. In order to solve the above problems, we use a handle wafer that reversibly attaches to a device wafer to prevent He leaks. We chose photoresist (AZ4620) as the intermediate bonding layer. During photoresist bonding only the wafer edge is coated with resist to prevent footing damages. Quartz wafers were chosen as the handle wafers because they provide an excellent etch stop. In addition, the optically transparency of quartz allows for visual inspection of etching completion of small features from the backside.

After the etching, the handle wafers are released with a combined acetone rinse and piranha etch. A buffered hydrofluoric etch removes the sacrificial oxide, followed by another piranha and oxygen plasma ashing. Because piranha does not remove the passivation film deposited by the ICP etcher, it is necessary to go though all the above cleaning steps to prevent surface delamination during bonding. Occasionally, a repeat of the above cycle is required to fully clean the surface. Once the wafer is cleaned, we obtain a wafer with aligned features etched from both sides and pristine surfaces for the next bonding steps.

### 3.2.2 Multiple wafers aligned silicon fusion bonding

Historically, some of the earliest uses of wafer-to-wafer bonding were for packaging. [11] There are two common bonding techniques, one called anodic bonding, the other called eutectic bonding. Anodic bonding involves the use of both elevated temperatures and an electric field, and is performed using a silicon wafer and sodium-rich Pyrex glass wafer. The applied temperature is usually around 400°C, and required voltages range from 200~1000 Volts. Eutectic bonding uses an intermediate layer that will form a eutectic alloy with the bonded substrate and 'solder' the two wafers together. The bonding is performed around the eutectic temperature (typically 200-400°C) of the chosen material system, and applied pressure or scrubbing is sometimes required to improve the bonding quality. Low temperature bonds appeal to the IC industry for packaging and there have been continuous efforts to reduce the bonding temperature with various techniques, such as spin-on glass bonding, polymer bonding, and surface activation bonding. For example, a recent paper reports successful bonding using lithium aluminosilicate-β-quartz glass at 160°C [12]. The required alkali-rich glass in anodic bonding is a design constraint and thermal mismatch will create stress problems at elevated temperatures. Eutectic bonds are typically weaker and can

separate once the temperature is raised beyond the eutectic points [13]. Direct silicon-to-silicon fusion bonding was developed to provide a strong permanent high-temperature-stable bond and to extend the process design space to include novel actuators and wafer-level packaging [14].

For this project, the bonding has to be immune to the high temperatures (700-1000°K) at which the gas turbine operates. Therefore, silicon fusion bonding is the preferred choice.

Silicon fusion bonding is one of the most rigorous micro-machining processes. It requires a very clean environment to minimize particles and surface residues which may ruin the bond. A mirror flat surface with roughness less than about 20 Angstrom is required. It is also critical to minimize the wafer bow.

The fusion bonding process usually begins with a standard RCA clean ($H_2O_2$:$NH_4OH$:$H_2O$ /HCl:$H_2O_2$:$H_2O$) followed by wafer contacting and a high temperature anneal. The RCA clean does not just clean the surface but also creates hydroxyl-dangling bonds on the surface which transform into Si-O-H-O-Si bonds after the initial contact. During thermal annealing, typically at 800°C to 1100°C, the hydrogen and oxygen atoms diffuse away from the interface and the bonding strength increases. Eventually, the two wafers are fused together with no observable interface layer left. As with other bonding techniques, there is also a constant interest in reducing the required bonding anneal temperature. Sometimes a surface treatment, such as physical bombardment of inert gas, is performed prior to bonding to create more dangling bonds [15]. Annealed at the same low temperature (<400°C), the bonding strength improves compared to wafers without the surface treatment.

As the number of process and/or stacked wafers increases, there is a higher probability of warpage and particle contamination and bonding becomes challenging. Bonded wafers are usually examined by an IR source using a CCD camera. Bonding voids appears as concentric fringes (Newton rings) whose spacing correspond to the vertical gap of the delaminated region. (Figure 3-22) X-ray and ultrasound provide alternative methods for inspecting the bond quality. The bonding strength has been characterized by a number of techniques, and is typically in the range of 2000 erg/$cm^2$ [16].

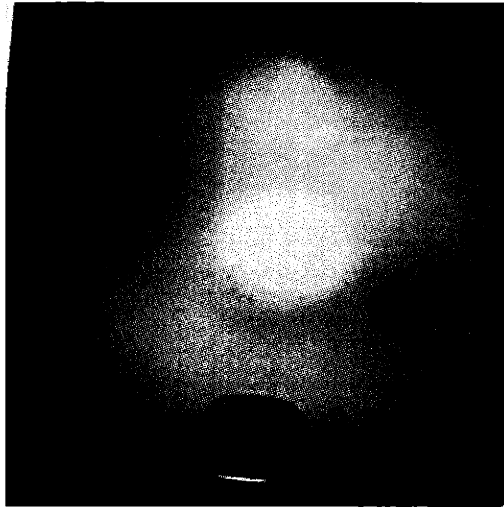

**Figure 3-22 Infra-red image of a fusion bonded pair of silicon wafers. There are several voids casued by either particles or surface contamination.**

There are a number of problems encountered during the bonding of multiple stacks of wafers. Figure 3-23 shows the infrared image of a bonded 5-wafer stack from build one to build four and a recent good build. The problems encountered are clearly shown in the images. Based on these runs, we can formulate several important factors that need to be considered for multiple-wafer fusion bonding.

1. Eliminate wafer plastic deformation caused by sealed cavities:
In build one, the 5-stack was delaminated due to wafer deformation caused by expanded air in sealed cavities during the wafer anneal. The source of deformation was two shallow cavities that were 1 μm deep surrounding the alignment marks (dark square region on either side of the wafer). These two 1 cm by 1 cm windows were included to help locate the alignment marks in aligning dark field masks. Even though the 'membrane' thickness above the cavity is 450 μm, it can still plastically deform by more than 25 μm after the bonding anneal. This deformation formed pivot points so that only an H-shaped region of the wafer was bonded.

2. Relieve or remove stressed thin films that introduce wafer warpage:
We developed the step of adding a sacrificial oxide film to protect the backside of the wafer during through wafer etching. In the $2^{nd}$ build, the film wasn't stripped before the bonding of the endplates and caused the bonded wafer pairs to bow. When we contacted all wafers together, the bowing only allowed the center of the wafer to be properly contacted, and eventually only 3 bonded dies were obtained from this build.

3. Apply low pressure during bonding:

In the 3rd build, uniform pressures were applied during bonding to assist wafer contact. An improvement in wafer contact is clearly shown in the IR image. However, the wafer cracked during the anneal. The crack started from the points where the aligner/bonder sticked flats in to keep wafer apart during alignment. These flats, if not cleaned properly, can easily leave particles and scratches that stress the wafers when the stacks are pressed together during bonding. The cracks can propagate due to thermal shock if the wafers are loaded into the anneal furnace too quickly. In build 4, lower pressure was applied (4000 mbars) and we reduced the speed of loading for wafer anneal, eliminating the cracks.

In summary, it is easy to get accumulated deformation issues caused by the imperfection of prior bonds. In build 4 all 12 dies were recovered after die separation but only 9 of them showed proper function (chapter 5). It is necessary to follow a strict protocol to minimize any bonding imperfections that will keep aggregating when stacking multiple wafers together. Also, it is very difficult to get good bonding at the periphery of the wafer. Finally, the flatness of the starting material is also very important. Once paying attention in each step by following a strict protocol, we start to obtain good quality bond and higher yield.

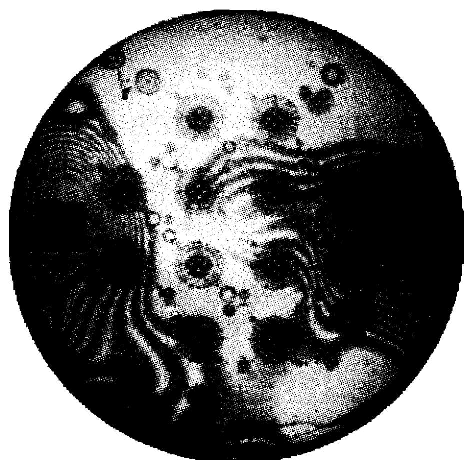

1st build

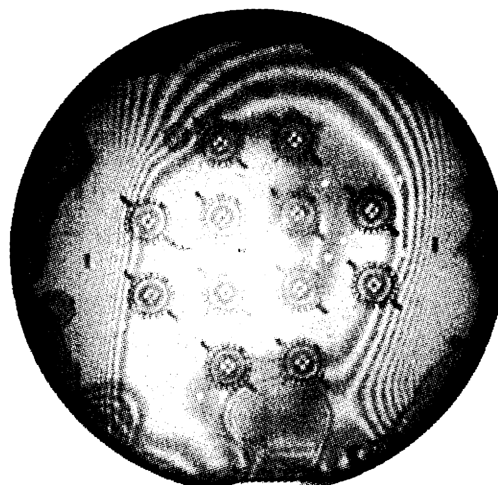

2nd build

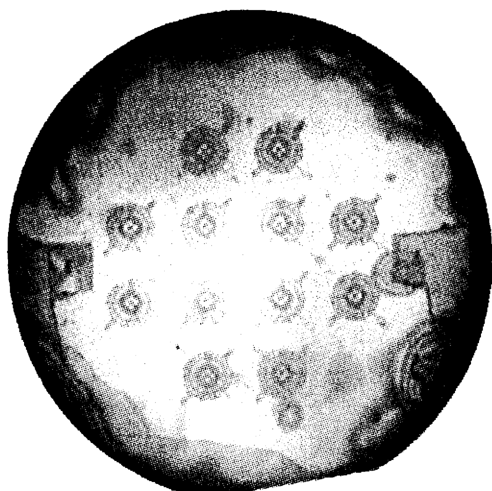

3rd build

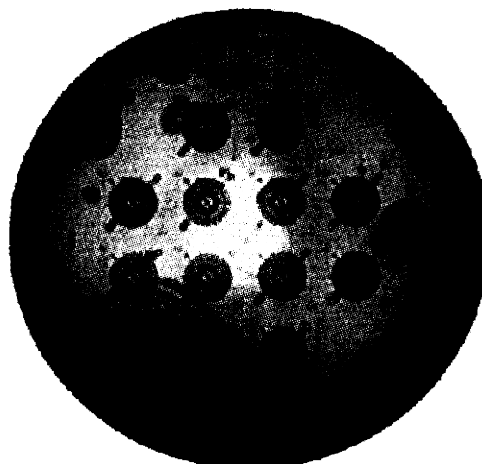

4th build

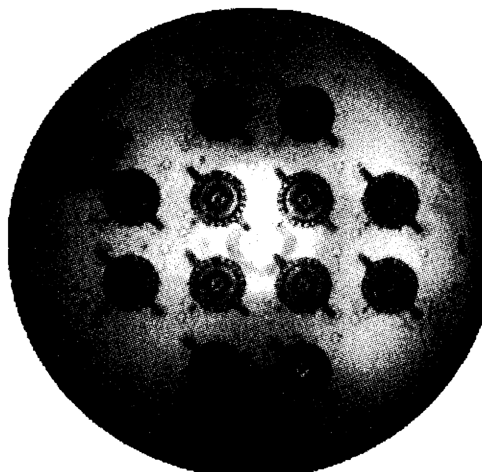

8th build

**Figure 3-23 IR image of bonded 5-wafer stacks.**

### 3.2.3 Laser-assisted silicon etch and free-moving part fabrication

Laser etching is an ablative process that is often used for serial processes like micro-trimming of resistors. The laser-assisted etch [17], sometimes called LAE or LACE (Laser Assisted Chemical Etch), is a chemically assisted process that relies on the reaction between silicon and chlorine. An argon ion laser beam (8W) is focused to a micron size spot that heats the silicon locally to near its melting point in a chlorine flowing ambient. The heated silicon volume reacts with chlorine to form volatile silicon tetrachloride that is carried away by the flow (Figure 3-24). The system, at Lincoln Lab, was established by Dr. Bloomstein. The author would also like to acknowledge helps from D.-Z. Chen and R. Ghodssi.

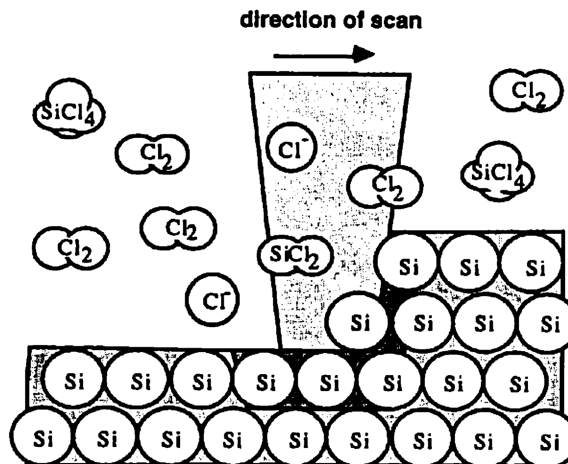


**Figure 3-24 Laser assisted silicon etching. (T. Bloomstein, 1995)**

One issue of the proposed aligned through-wafer etching bonding protocol is that it's inconvenient to build free-moving parts based on the protocol. If we allow the free part to be etched from both sides of the wafer, it will fall off at the completion of the etching. It will be extremely hard to handle those pieces and go through the proper cleaning steps for fusion bonding. In the prototyping phase (Appendix A), we used a die-level thermal compression bonding scheme to allow the handling of small pieces. Unfortunately, it reduced the yield significantly.

Laser assisted etching provides us with one way of resolving this issue as shown in Figure 3-25. After the 1$^{st}$ deep etch, the wafer that has the free-moving part is fusion bonded to another wafer

that has pre-defined sacrificial tethers. After bonding, the 2nd deep etch is performed to separate the part. The bond at the sacrificial tab prevents the rotor from falling off. After capping the free part with a third wafer, we use LAE to etch the sacrificial tab away and create the free moving structure. Alternatively, we can put the tab on the middle wafer (shown with dashed line in the figure). This approach has two advantages because we can postpones the bonding to the last step. First, we only need to perform deep etch on single wafer instead of bonded pairs. This helps with dimensional inspection and thermal dissipation during etching. Second, we only lose one wafer instead of a couple of wafers prior to the final bonding step, therefore yield is improved. However, in the micro bearing rig design we cannot allocate ports for the laser to reach the journal bearing.

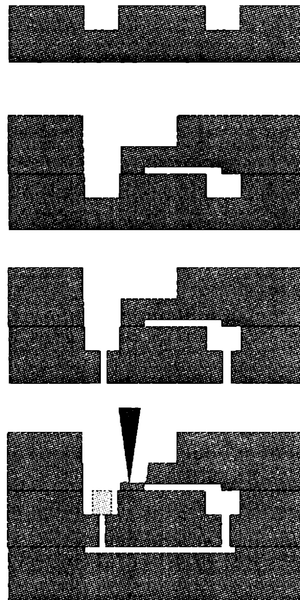

**Figure 3-25 Extension of aligned multiple wafer etching/bonding protocol to create a free-moving part.**

The SEM in Figure 3-26 shows the sacrificial tether. The size of the tether is determined by the minimum area that can assure a good fusion bond, proper laser focusing, and reasonable etching time. The current design measures 100 μm long, 300 μm wide, and 100 μm thick. Because the laser is focused by a lens that is located above the sample and will be clipped by the edge of the top wafer, it is hard to completely remove the tab. A recess across half of the 100 μm length is cut such that the rotor is bonded only to the outer half of the tab (50 μm by 300 μm). During etching, only half of the tab needs to be removed to free the rotor. Figure 3-27 shows an SEM of the area where the removed tab was located.

(a)

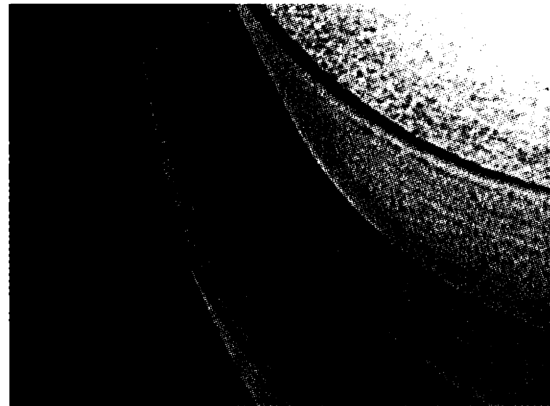

(b)

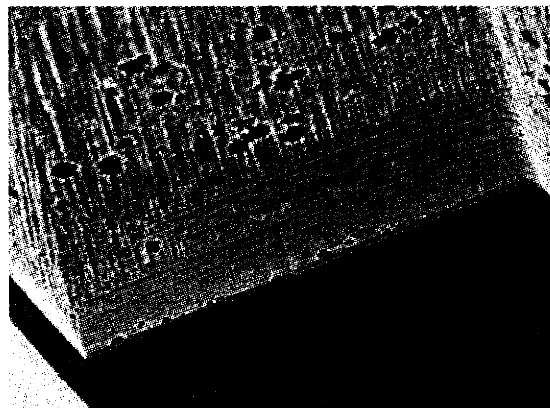

(c)

**Figure 3-26 SEM showing the sacrificial tabs that hold the rotor shaft. (a) The image is taken from the main air exhaust. (b) Close-up view of the tab. The height is 100 μm, width is 300 μm, length 100 μm. (c) Further close-up shows the recess cut into the tab, The left half is bonded, while the right half has a 1 μm gap.**

**Figure 3-27 SEM showing the completely removed tab. Overetch of the order of a few microns that cuts into the rotor shaft is also shown.**

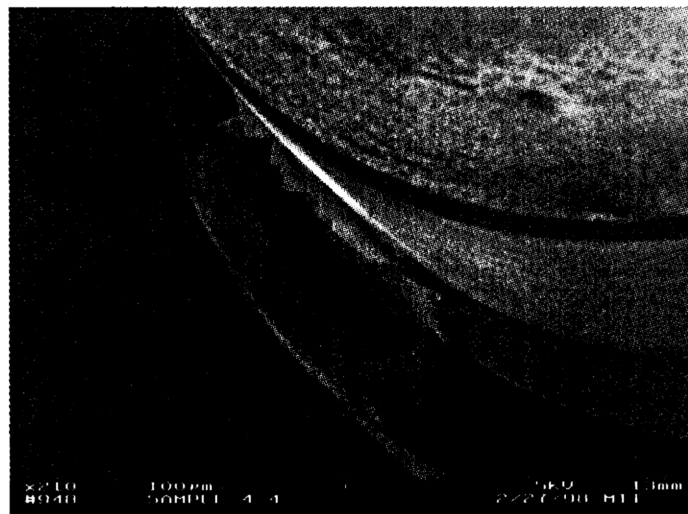


**Figure 3-28 Thin film shells that impede completion of the tab removal.**

**Figure 3-29 The collapsed thin film shell. The tab is still removed in this case.**

A thin film residue that covered the outer shell of the tabs is usually discovered once the sample is etched (Figure 3-28). The film often times collapses and prevents the laser from being properly focused, causing the etch to fail. Auger analysis of the film indicates a high concentration of oxygen and carbon atoms in addition to silicon. Ion-sputtering surface removal confirms that the carbon only exists on the surface and that there are a few thousand angstroms of oxygen rich silicon. It is believed that the source of the film comes from incomplete cleaning of the ICP sidewall passivation polymers. Once the wafer goes through the high temperature fusion bonding anneal, the fluorine atoms are released and a mixture of a carbon rich, silicon layer is formed. The additional oxygen could come from trapped water in the recess areas after the RCA clean prior to bonding. It is discovered that a high-power oxygen plasma clean followed by 10 minutes of 1:1 HF/DI dip reliably removes the film, significantly improving the yield of the LAE tab removal.

### *Section 3.3 Reference*

[1] Lin, C.-C., Ghodssi, R., Ayon, A. A., Chen, D.-Z., Schmidt, M. A., "Fabrication of a Micro Turbine/Bearing Rig," IEEE Solid State Sensors and Actuators Workshop, 1998, late news poster paper.

[2] Lin, C.-C., Ghodssi, R., Ayon, A. A., Chen, D.-Z., Epstein, A. H., Breuer, K., Schmidt, M. A., "Fabrication and Characterization of a Turbine Driven Micro Bearing Rig," IEEE MEMS 99, 1999, pp. 529-533.

[3] Bloomstein, T. "Laser Microchemical Etching of Silicon" Ph.D. Thesis, MIT, January 1996.

[4] Hhardwaj, J. K., and Asharaf, H., "Advanced Silicon Etching Using High Density Plasmas," SPIE vol. 2369, pp. 234-243, 1995.

[5] Ayon, A.A., Bayt, R., Braff, R., Lin, C.-C., Sawin, H.H. and Schmidt, M.A., "Etching Characteristics and Profile Control in a Time Multiplexed Inductively Coupled Plasma Etcher," Technical Digest, Solid-State Sensor and Actuator Workshop, Hilton Head, SC, June 8-11, 1998, pp. 41-44.

[6] Ayon, A.A., Braff, R., Lin, C.C., Sawin, H.H., Schmidt, M.A., "Characterization of a Time Multiplexed Inductively Coupled Plasma Etcher," Journal of the Electrochemical Society, Vol. 146, 1, January 1999, pp. 339-349.

[7] Chen, K.S., Ayon, A.A., Lohner, K.A., Kepets, M.A., Melconian, T.K., and Spearing, M.S., "Dependence of Silicon Fracture Strength and Surface Morphology on Deep Reactive Ion Etching Parameters," MRS fall meeting, Boston, MA, 1998.

[8] Epstein, A.H., et. al., "Micro Gas Turbine Generators", Interim technical progress report, 1997.

[9] Ayon, A.A., Ishihara, K., Braff, R.A., Sawin, H.H., Schmidt, M.A., "Microfabrication and Testing of Suspended Structures Compatible with Silicon-on-Insulator Technology," Journal of Vacuum Science and Technology, February, 1999.

[10] Ayon, A.A., Braff, R.A., Bayt, R., Sawin, H.H., and Schmidt, M.A.,"Influence of Coil Power in the Etching Characteristics in a High Density Plasma Etcher," Journal of the Electrochemical Society, Vol. 146, 7, 1999.

[11] Ko, W. H., Suminto, J. T. and Yeh, G. J., "Bonding Techniques for Microsensors," Micromachining and Micropackaging of Transducers, Elsevier, 1985, pp 41-61.

[12] S. Shoji, H. Kikuchi,and H. Torigoe, "Low temperature anodic bonding using lithium aluminosilicate-b-quartz glass ceramic", Sensor and Actuators, A 64, pp 95-100, 1998.

[13] Tiensuu, A.-L., Bexell, Schweitz, J. A., Smith, L., Johansson, S., "Assembling three-dimensional microstructures using gold-silicon eutectic bonding," Sensors and Actuators, A 45, 1994, pp. 227-236.

[14] Martin Schmidt, “Silicon wafer bonding for micromechanical devices”, Solid-State Sensor and Actuator Workshop, Hilton Head, 1994.

[15] Takagi H., Maeda R., Chuang T.R., Suga T., “Low Temperature Direct Bonding of Silicon and Silicon Dioxide by the Surface Activation Method”, IEEE Transducer 97, pp.657-660.

[16] Shimbo, M., Furakawa, K., Fukda K., and Tanzawa J., Applied Physics, 60, 2987, 1986.

# Chapter 4

# Packaging and Instrumentation

Packaging and instrumentation constitute an important part of this thesis. This chapter will first cover the packaging design, followed by a discussion concerning the instrumentation, including the fluidic control system and speed sensor.

## *Section 4.1 Packaging*

Packaging needs to be designed to allow for proper fluidic connections and instrumentation interfacing for device testing. It is designed in parallel with the fabrication process to ensure compatibility. The design guidelines for the current packaging scheme are:

1. Installation simplification: Repetitive use of the package is expected, and minimal installation time is preferable.

2. Instrumentation compatibility: Since it is undesirable to add further fabrication complexity by integrating micro sensors into the device, it is important that the packaging be compatible with external sensors, in particular an infrared optical position sensor. The transmissivity of the packaging is therefore important.

3. Online Inspection: Online inspection of the device is an important part of the testing procedure. Therefore, it is desirable to have the capability to check fluidic blockage and die alignment during a run.

4. Leak-free connections: The designed operating pressures for the thrust bearings is 100 psig. To minimize the flow measurement errors, we specify a maximum system leak rate of 0.2 sccm at design pressure.

In the early stage, a first generation package was built for testing the micro rig prototype. Based on experience from initial testing, a refined 3-plate PMMA-aluminum package was designed to fulfill the objectives above. Figure 4-1 illustrates the concept of the design, and detailed drawings are included in the appendix. The top and bottom plates, which are made of Plexiglass (PMMA), are transparent to the visible light and near infrared light used for the sensors. The middle piece has a center recess to hold the die. Small tweezer slots are machined on both sides of the recess for die handling. Because there is no need to shine light through the middle plate, we chose aluminum as the bulk material. Choosing aluminum has another advantage as it can be machined to a thickness that is 2 mils thicker than the device thickness. In this way, the top and bottom plates are not directly compressed on the device, and the die is held in place by the compressed o-rings. This design minimizes device bending caused by plate flatness problems. Two-dimensional finite element analysis was performed by Dr. K.-S. Chen to estimate the deformation to the device that would result from the compressed o-rings. It was determined that this would have a negligible effect on the device.

One advantage of the three-piece design is that if a device with higher L/D ratio journal bearings is fabricated, we only need to replace the middle plate, which is easy and inexpensive. Besides, there is no need to perform post-machining plastic polishing inside the sample-holding recess to maintain good packaging transparency.

Stainless steel tubes are glued with epoxy to the top and bottom plates to bring air in and out of the device. One end of the tubes is bulged (made by Scanivalve [1]) to allow quick push-fit connection to special-sized Teflon tubes, which lead to the fluid control/measurement system.

O-ring glands are machined in the PMMA to accurately set the o-ring compression ratio to 25%. Because the space is tight, the inner gland walls are eliminated from the design. This design is

valid as long as the o-rings are exposed to higher pressure at the inner radius so that the rubber is pressurized toward the outer gland wall.

An additional plate was used to cap off the forward main exhaust completely for internal flow testing (chapter 5). We also added gaskets that were laser-machined out of latex rubber to fit in between the plates to prevent leakage through the inter-plate gaps. We are hence able to force the flow to follow a particular path and to exit from a particular port.

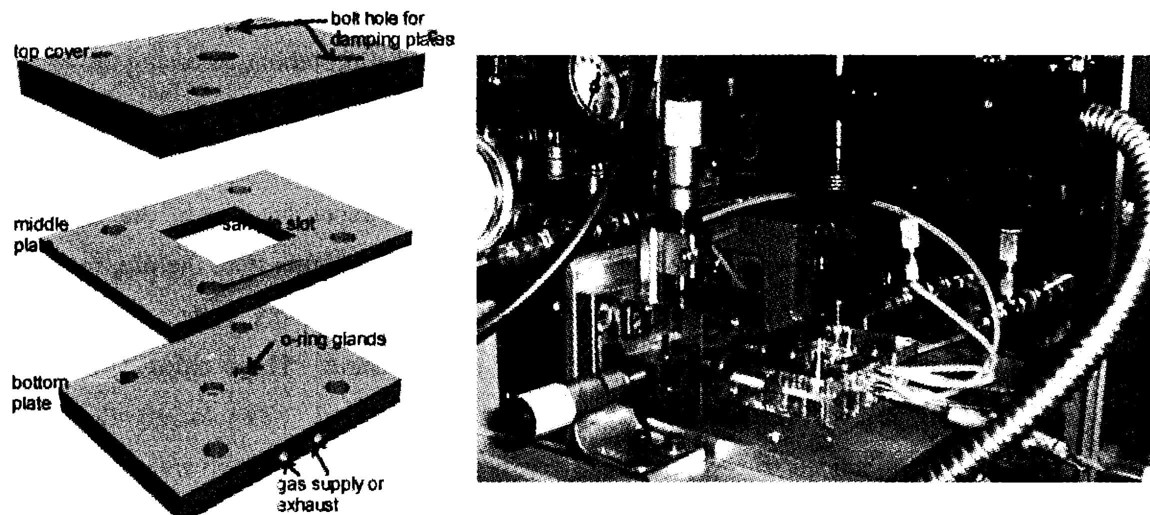


**Figure 4-1 Concept of micro bearing rig packaging.**

Spring-loaded pins were included in the design to allow for electrical contact. Because the designed capacitive speed sensor was not built within the time frame, the pins have not been tested.

During die installation, the plates are aligned in two steps by registering dowel-pins to holes on each plate. After the 1$^{st}$ alignment, the top and middle plates are clamped together by two bolts. The o-rings are then mounted into the glands. The sample is dropped into the slot afterward. The sample is held in place by a pair of thin stainless steel tabs (machined out of shim stock) so that it won't fall out in the next step. Thereafter, o-rings are loaded in the bottom plates and aligned to the flipped top-middle plates with sample facing down. Four bolts, with washers distributing the load, clamp the package together. After the package is connected to the fluidic system with the Teflon tubes, the installation is completed.

This package scheme has a achieved a leakage rate of less than 0.2 sccm at up to 125 psi. The leak test involves the use of a solid silicon block to replace the actual sample. High-pressure nitrogen is fed to each port and the flow rates are measured by MKS mass flow meters with a full scale range of 20 sccm. These meters have an accuracy of 1% of the full scale.

Based on an experiment using glands with different depths, it was found that at least 20% compression of o-rings is need for proper sealing, and an over-drilled o-ring gland would cause a big leak. Aging epoxy will result in micro cracking and de-bonding at the interface, which causes leakage. This is partially caused by frequent installation of the Teflon tubing, stressing the epoxy cyclically. Flexible tubing with quick connectors would be a better choice for future designs.

Die deformation is another problem that can be caused by the repetitive use of the package. Although the middle plate is precisely machined to be a few mils thicker than the die, repeated installation and de-installation of the die leaves scratches on the PMMA plates. Sometimes fragments of silicon chips embed into the PMMA and remain there. These chips deform the PMMA locally and are very difficult to remove without polishing. The locally deformed top/bottom plate and embedded silicon can directly press the die after installation and result in die bending and bearing gap variation. This information is supported by the thrust bearing flow measurement and will be explained in chapter 6. A surface re-polishing was performed to eliminate the problem, but repetitive polishing is impractical and will compromise the dimensional accuracy of o-ring glands.

The speed sensor fiber interface on the device is simply a through-wafer port that directly leads to the trailing edge of the blades. The hole was originally designed to be 5 μm larger than the 125 μm-diameter fiber. Early tests showed that it was very difficult to insert the fiber properly, probably due to the typical tapering of the DRIE hole. The new designs incorporate 150 μm diameter fiber holes on the die. A C-shaped slot, twice the size of the port, is machined on the top PMMA plate to allow the fiber to reach the port. The fiber is held and positioned by an external x-y micro-stage to ensure proper alignment and insertion depth control.

## *Section 4.2 Instrumentation*

There are several parts in the instrumentation system: a fluidic control/measurement subsystem, a laser-fiber speed sensor, a stereoscope that is being upgraded to an infrared lateral positional spectrometer, a commercial fiber bundle axial position sensor, and a data acquisition system.

The details of each sub-component will be explained in the following sections except the IR position sensor. The details of this sensor will be part of Dye-Zone Chen's thesis [2].

### 4.2.1 Fluidic control/measurement system

The purpose of this system is to provide flexible pressure control and flow rate monitoring of each port. The layout is shown in Figure 4-2. MTL house nitrogen is chosen to be the source because it has higher line pressure (160 psi) and is cleaner and dryer than the house compressed air. A low loss, 0.002 μm class filter (Millipore) is attached downstream from the wall, and the line is split into two branches. One branch provides flow for the thrust bearings, and the other for the journal bearing and the turbine.

The characteristics of the thrust bearing flow line are high pressure and low flow rate. Two independent flow regulators are used, both connected to MKS 179A mass flow meters in series, and branch to Honeywell 240PC series pressure transducers. The downstream tube length is minimized to reduce compressive effects that could cause delay in the pressure/flow measurement response.

The other branch (lower half in the figure) is more complicated with a backbone of a pair of pressure dividers. All mass flow meters except the one measuring main turbine flow are made by MKS (179A series); the main air flow meter is a Honeywell AWM5102. This design allows for a "one-knob" operation so that the pressure ratio between different ports stays fixed. One only has to control the main metering valve (valve A) to set the pressures properly. This simplifies the testing operation. To function properly, each pressure divider relies on a large flow-resistance ratio between the vent flow and the gauged flow, and the vent flow is usually at least 10 times

higher than the gauged flow. Since the majority of fluid is dumped to the vent, this setup is less sensitive to leakage.

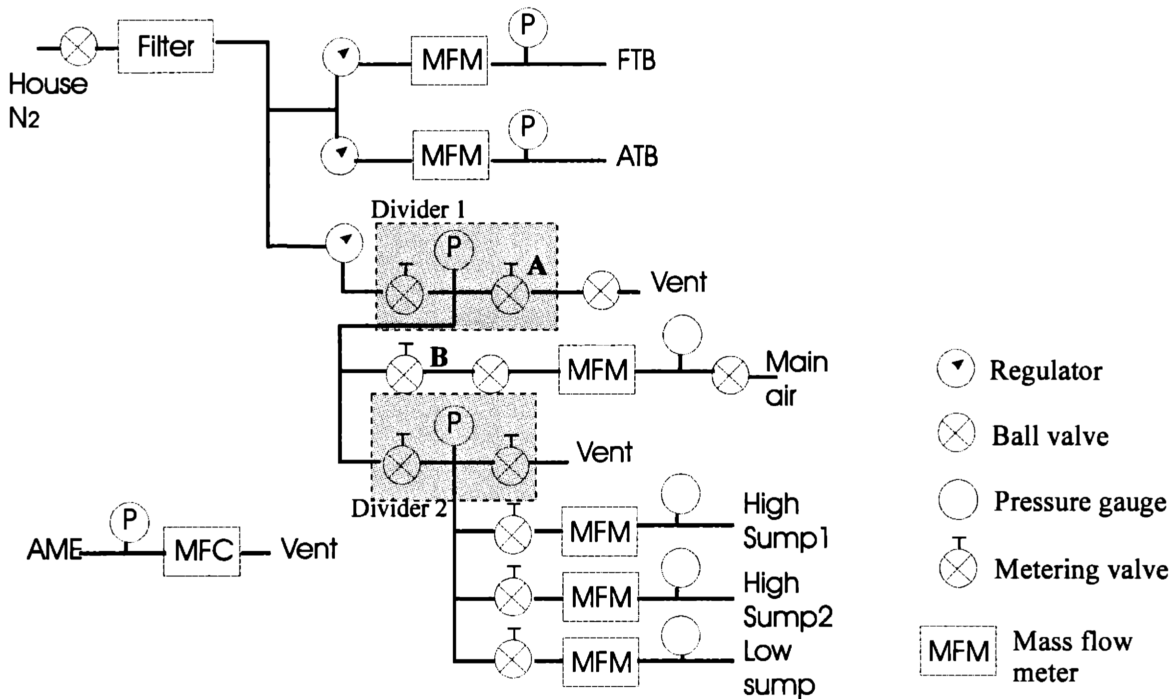


**Figure 4-2 Diagram illustrates the flow control and testing system. FTB: forward thrust bearing. ATB: aft thrust bearing. AME: aft main exhaust. A pair of pressure dividers enable the one-knob operation.**

Alternatively, the system is also designed to operate in direct feeding mode by shutting off the two vent ports of the pressure dividers. In this mode, the pressure ratio to different ports will not stay constant if we only adjust valve A, but one can adjust individual metering valves to set the pressure to each port.

One metering valve that provides additional resistance is added to the flow path downstream of the main valve (valve B in Figure 4-2). The purpose of this valve is to add flow resistance to further reduce the main pressure to a level below the sump pressure. This mode is needed to provide higher side loading, if necessary, to stabilize the bearing. MKS 179A mass flow meters and Honeywell pressure transducers are attached to each line, and electrical readouts of these meters are fed to the data acquisition system.

### 4.2.2 Speed sensor

Figure 4-3 shows the theoretical acceleration rate of the micro turbine, according to the torque calculated from GTL MISES code (by S. Jacobson). Two acceleration curves are shown in the figure. The solid line assumes that increasing pressure (which minimize flow separation in turbine) is applied according to speed to balance the drag, and the dashed line assumes a fix pressure of 5 psig is applied. As indicated in the plot, the small mass of the rotor results in a very high acceleration rate. Provided that enough pressure is supplied to balance the drag, it takes less than a second to reach the maximum speed. It has been experimentally proven that the rotor can accelerate to 60,000 rpm in 0.1 sec (chapter 6).

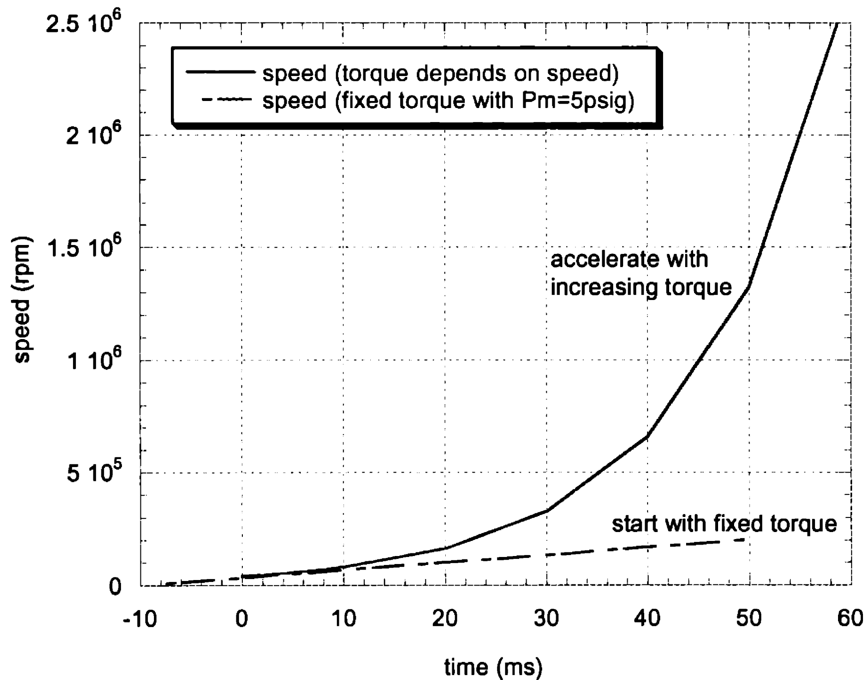


**Figure 4-3 Rotor acceleration rate.**

In order to capture the speed evolution along the runs, a fiber optic speed sensor was designed and built to measure the speed. The speed sensor consists of two parts. The optical part includes a 25 mW diode laser (from MeshTel) with wave length of 890 nm, a fiber coupler, a HP 4662 photo detector, and 125 μm diameter multi-mode fiber cables. SMA connectors are used to connect the source and detector to one end of the coupler. The other end of the coupler is connected to a fiber probe that has one end stripped to expose the bare fiber tip. The electronic

system consists of a 3-stage op-amp that forms a Schmitt trigger, a frequency divider, and an Analog device AD 573J frequency to voltage converter.

The layout of the optical subsystem is shown in Figure 4-4. The light emitted from the diode laser goes through the coupler to the fiber probe. A two-axis translational stage adjusts and holds the probe tip so that it points directly on the top surface of the turbine blades. The distance from the probe tip to the blade is approximately 100-150 μm. The blade top surface is mirror smooth (original polished wafer surface, but the surface between blades is rougher due to the ICP etch. Also, the surface between blades is 200 μm (blade height) further away from the probe tip. Therefore, the intensity of the reflected light varies when the blades move past the fiber. As the rotor starts spinning a light pulse train is collected at the probe tip. This pulse train, which goes through the coupler, is sensed by the photo-receiver and converted to an electrical signal. The large number of optic connectors (5) in the system increases the coupling loss, and there is additional significant loss at the bare probe tip. Using a 25 mW source, we collect μW level signals at the photo-receiver (determined using a power meter), orders of magnitude lower than the source. Even with a highly sensitive photodiode (7 mV/μW), the highest signal level is about 3 mV. The system has a very low signal-to-noise ratio as a noise level of about 0.5 mV is observed.

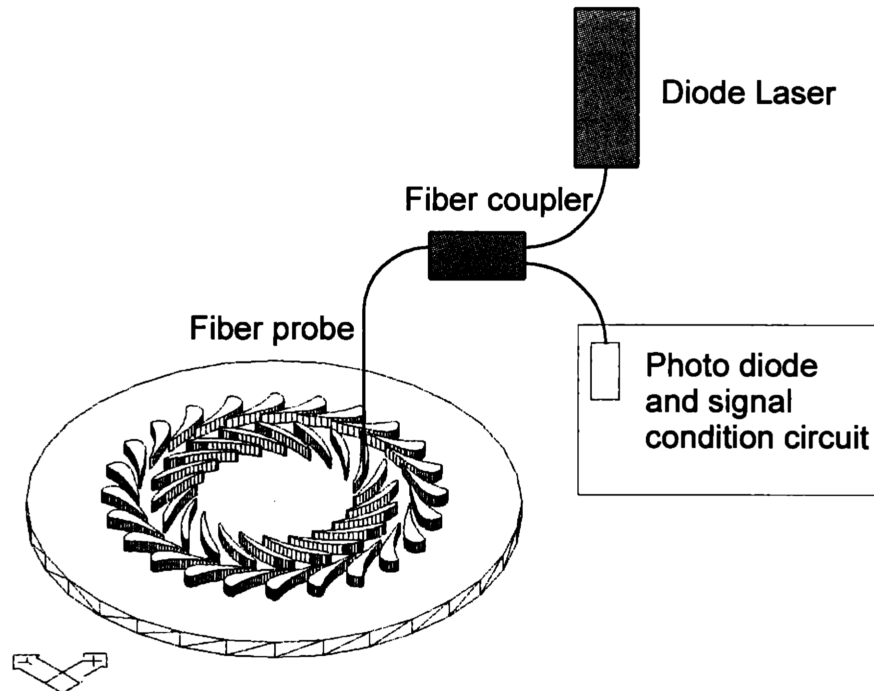


**Figure 4-4 Fiber optic speed sensor**

One problem for the electronics is the required frequency range. Since we are counting blades (there are 20 blades per rotor), the designed speed range of the rotor translates to a frequency variation of DC-1MHz. We used a commercial frequency-to-voltage converter (Analog Device AD 573J) that has a bandwidth of 100 kHz with a low frequency response limited by ripples below 100 Hz. To solve the problem of frequency limit, we add a frequency divider that reduces the number of collected pulses by a factor of ten. For low speed operation, we choose to give up the bandwidth below 150 Hz because we are not interested in operation at this low speed range (450 rpm).

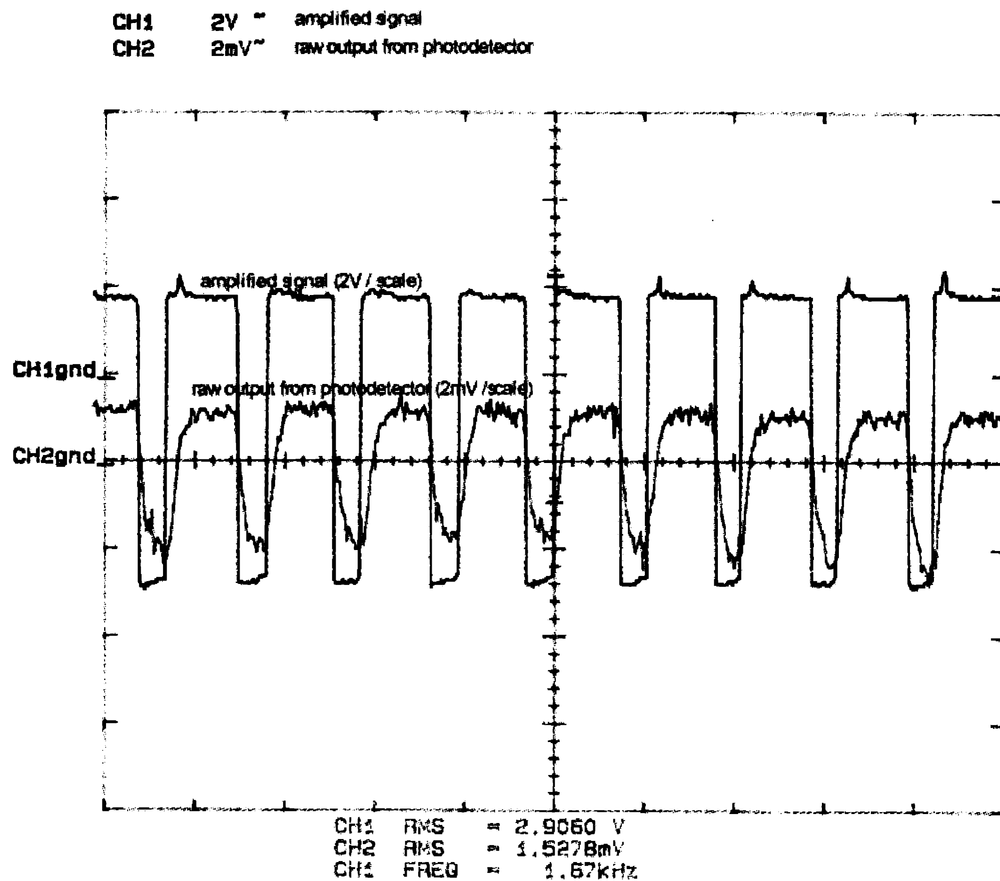


**Figure 4-5 Signals from the photo detector and the amplified signal.**

The response of the sensor is tested in two different ways. At low speed, a micro-fabricated rotor is glued to the tip of the electric motor shaft. The bare fiber probe is positioned to point at the blade tip so that a realistic shape of the pulses is generated. As the rotor spins, the pre/post-amplified pulses are displayed on the scope simultaneously to ensure that no extraneous signals are generated during amplification (Figure 4-5). The resistors are adjusted in this stage to optimize the setup of the comparator threshold. The maximum speed of this setup is limited by the motor to 5,000 rpm.

For higher-speed calibration, the probe is positioned to shine vertically on a flat piece of silicon. A function generator that produces square and triangle waves, with frequencies up to 1 MHz, modulates the laser to simulate optical pulses generated by the blade chopping. The conversion factor of the sensor, 38.125 Hz/mV, is obtained up to full speed.

For part speed transient analysis, the amplified pulses are fed to a high-speed data acquisition card (National Instrument PCI-MIO-E16-1) that can scan at up to 1.25 MHz. At this rate, we can resolve up to 60% of full speed. This is sufficient for post-test transient analysis.

### 4.2.3 Axial position sensor

Another fiber-optic position sensor was purchased from Philtec (model D6-A1BMTV+L+H) is used to assist in the axial position measurements. The original plan was to calculate the axial position based on the bearing flow rate. Since the hydraulic system reacts much slowly and the flow meter is connected upstream externally, this method is indirect and only represents time-averaged response. Additionally, the hot-wire mass flow meters that we are using have a settling time of about 1 sec.

The Philtec sensor works with similar principles to the speed sensor. The Philtec design eliminates the coupler and reduces connector loss though the use of a fiber bundle. The main fiber cable consists of a number of fibers, half of which transmit light, and half of which collect the reflected light. During on-site calibration, we proved that the reflection intensity was very well correlated to the distance (Figure 4-6). In the calibration, we used micro-fabricated rotor as the target surface, and positioned the sensor probe with an electrostrictive micrometer (model AD-100) from Newport. At the near side, a sensitivity of 0.02 μm/mV was achievable. Nevertheless, there is still a drift problem, and the discretion between tilting and translation is difficult. Operation during spin testing also requires uniform surface quality around the rotor, which is currently not well controlled. Vibration of the fiber due to the impingement of rotor exhaust air is another difficulty that has to be resolved in the future.

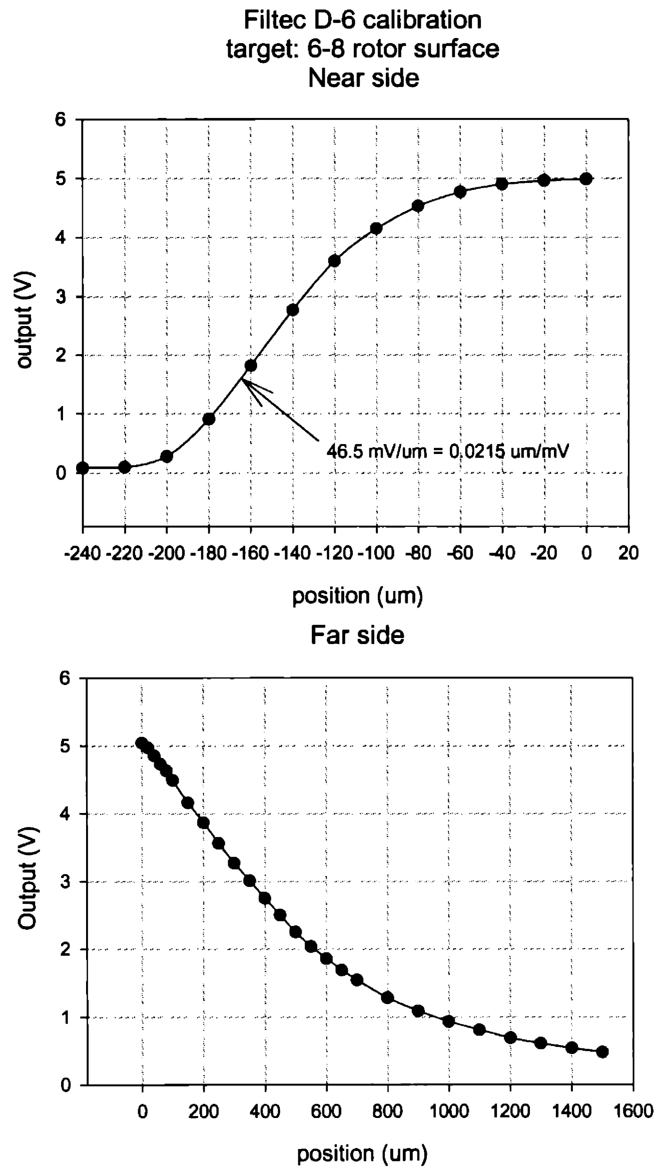


**Figure 4-6 Philtec (D6-A1BMTV+L+H) position sensor output.**

Despite the problems, this sensor can provide information on the rotor full gap during thrust bearing test and can also be used as speed sensor. The data will be summarized in the next chapters.

Finally, the author would like to acknowledge that a rotor position measurement is critical to understanding the rotor motion and analyzing bearing crashes. An infrared spectrum analyzer is being developed by D.Z. Chen [2] to address this issue.

### *Section 4.3 Reference*

[1] Scanivalve Corp., Liberty Lake, Washington.

[2] Chen, Dye-Zone, "Design and Calibration of an Infrared Position Sensor", M.S. Thesis, MIT, June, 1999.

# Chapter 5

# Static Flow Characterization

In this chapter we will present the results of static flow characterization of the micro bearing rig. The characterization has two purposes. First, to deduce device dimensions nondestructively. Second, to characterize thrust bearing performance.

Thrust bearing models are presented, and used to discuss the importance of each design parameter. The calculated results are then compared with experimental data from different generations of devices. This is followed by a discussion of utilizing flow measurements to characterize bonding yield and bearing dimensions. Finally, further validations of the model are presented, using bearing force information from a rotor axial position test.

## *Section 5.1 Fluidic modeling*

To understand the performance of the thrust bearings, one needs to know important parameters about the bearings, including the flow rate, the load capacity, the stiffness, and the power loss. In this thesis, the load capacity is defined as the maximum load that can be supported by the bearing. As shown in Figure 5-1, the load capacity comes from a integration of fluid pressure within the bearing gaps over the thrust bearing surface. The stiffness is the derivative of the supported load with respect to rotor axial displacement. The rotor axial displacement is typically normalized by bearing gap and expressed as axial eccentricity $\varepsilon$.

While load capacity provides information about the maximum force that a bearing can support, stiffness provides information about dynamics and critical frequency. While maximizing the load capacity and stiffness to match the design requirement, one will also optimize the design to obtain lower flow rate and reduce power loss. In this thesis, two different modeling approaches have been used to understand the thrust bearing parameters, and they will be introduced in the following sections.

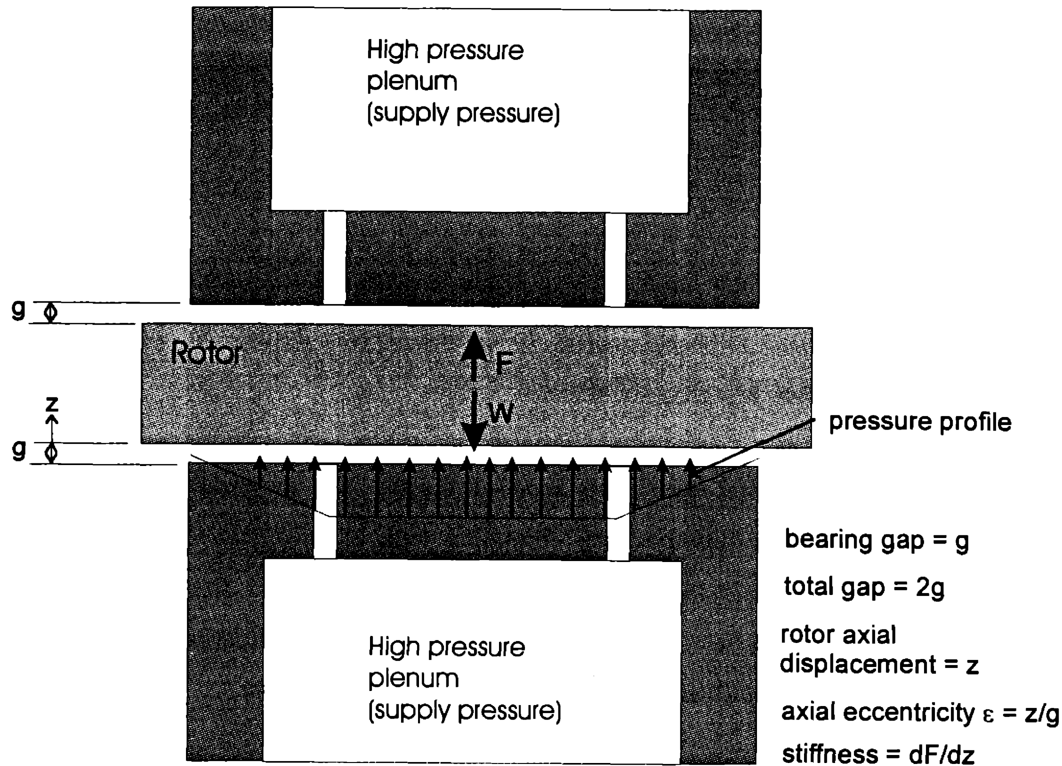


**Figure 5-1 Opposed thrust bearing pair. The load W is supported by a net-force F developed from fluid pressure acting on top and bottom. We define the bearing gap width in each side to be g when the rotor is centered. The total gap will be 2g, which equals to maximum travel of the rotor. The rotor axial displacement is defined as z, and the axial position is typically expressed in a non-dimensional form as z/g, denoted as axial eccentricity ε. The stiffness is defined as the derivative of the net-force F with respect to z.**

### 5.1.1 Baseline model

For capillary/inherent restrictor-compensated bearings, the design parameters are bearing pad size, capillary size and location, bearing gap, supply pressure, and the number of capillaries. At the beginning of the program, the bearing was designed through consultation with Dr. R. Walker at the Draper Labs. Later, an in-house baseline model was developed by Dr. Jacobson for design

purposes. This model simulates the thrust bearing with a series of flow resistances (Appendix C). This code provides quick results for parametric study over a wide field of designs.

With the baseline model, parameters such as total flow rate, stiffness, and load capacity can be quickly calculated with respect to different axial eccentricity and pressures. For example, Figure 5-2 shows the flow-rate variation vs. the supply pressure for different eccentricities of a single thrust bearing, which has eight 12 μm diameter capillaries and a 2 μm bearing gap. The bearing pad diameter is 1 mm (details see chapter 2). Changing axial eccentricity, denoted by ε, from –1 to 1 is equivalent to varying the gap from 0 μm to 4 μm in this figure. As expected, the flow rate is proportional to the gap with fixed pressure. And with a fixed gap, the flow rate is proportional to the supply pressure.

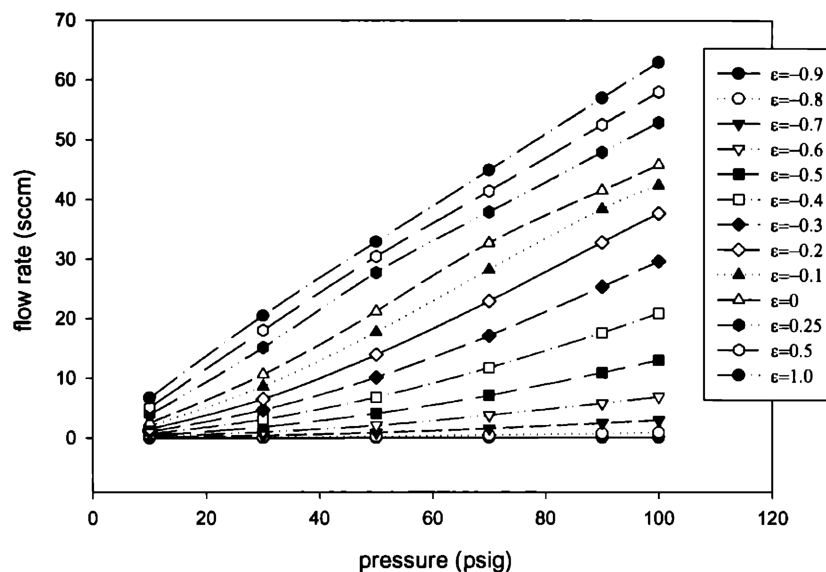


**Figure 5-2 Pressure flow relationships for hydrostatic thrust bearing with rotor at different eccentricity. The calculation assumes eight 100 μm long, 12 μm diameter capillaries, and a bearing gap of 2 μm (when ε=0).**

Figure 5-3(a) shows the predicted force vs. gap for a single bearing with 12 μm diameter capillaries. The force is proportional to the supply pressure as shown. In addition, the force decreases when the bearing gap increases. For our system, which has a pair of opposed bearings, the net bearing force is the force difference between a pair of bearings, and this is plotted in

Figure 5-3(b) for reference. In order to convert data from Figure 5-3(a) to Figure 5-3(b), one needs to choose a bearing gap from Figure 5-3(a) to define the rotor center position ($\varepsilon = 0$). The points in each line in Figure 5-3(b) are then defined by calculating the force difference between $\varepsilon = \pm\varepsilon_o$, and varing $\varepsilon_o$ from 0 to 1. Following this calculation, we find that larger bearing gap allows for longer rotor travel, which results in higher net force as shown in Figure 5-3(b). One should note that this trend is valid only in a small range because the force of a single bearing stops decreasing once the bearing gap exceed a certain length (~4 μm in Figure 5-3(a)). Consequently, the net force will no longer benefit from further increasing of the gap. For example, in the Figure 5-3(b), the gain in load diminishes when the gap increases from 1.75 to 2 μm as compared to increasing the gap from 1.25 to 1.75 μm. In addition, since we can estimate the stiffness by dividing the net-force at $\varepsilon = 1$ by the bearing gap, choosing a bearing gap that is too large to further raise the maximum net-force will reduce the average stiffness. Since critical frequency scales with stiffness, this is also not desirable. (One more reason for not choosing large bearing gap: large bearing gap increases the necessary mass flow.)

In order to find the optimal design to maximize both the loading capacity and stiffness, it is best to first inspect the single bearing force vs. bearing gap relationship. To the first order, a steeper slope in the single-bearing force vs. position curve means higher load capacity and stiffness. For example, Figure 5-4 shows the effect of the capillary diameter on the single bearing force. Although we get less loading from a single bearing with 10 μm diameter capillaries than ones with 16 μm capillaries and the same bearing gap, the net-force from a pair of opposed bearings is greater for the 10 μm capillary (as indicated by a greater slope in the 10 μm curve). Therefore, 10 μm diameter capillaries are favored for our design. Moreover, to maximize load capacity without reducing the stiffness, the optimal bearing gap would be approximately 2 μm at the point of inflection in Figure 5-4.

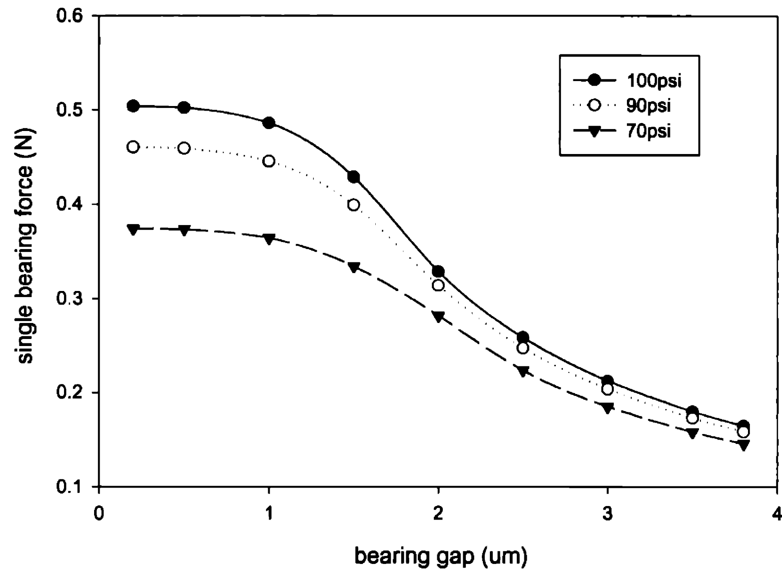


(a)

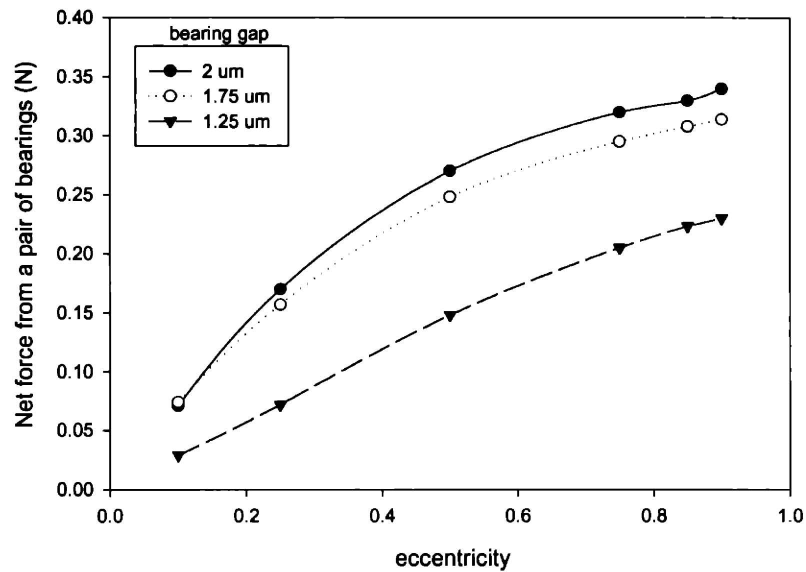


(b)

**Figure 5-3 Predicted (a) bearing force with respect to gap and supply pressure for a single thrust bearing, and (b) net bearing force from a pair of opposed bearings. This is calculated based on a design of with eight 12 μm diameter, 100 μm long capillaries.**

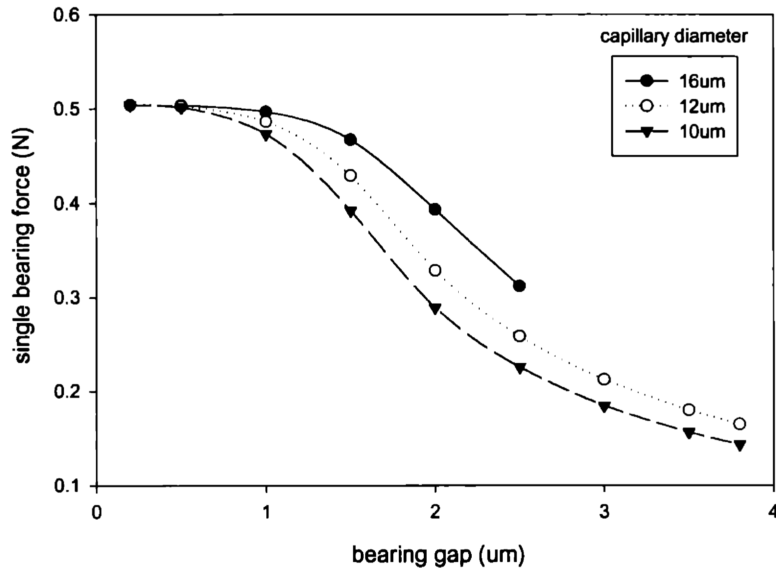


**Figure 5-4 Effect of capillary diameter on bearing force for a single thrust bearing, showing results of bearings with eight 100 μm long capillaries.**

After exploring the design space with the baseline model, we switched to a computational fluid dynamics model to get more detailed simulation results. These are discussed in the next section.

### 5.1.2 Computational Fluid Dynamics (CFD) model

After device testing, it was discovered that the baseline model did not fully capture the response of the device. In order to obtain better understanding of the current device and more accurate predictions for future designs, a full 3D CFD study was initiated using the commercial package (Fluent[3]). The complete Navior-Stokes equations with the compressible ideal gas law were used to solve the steady-state thrust bearing flow.

---

[3] Fluent V4.2, Fluent Inc., Lebanon, NH.

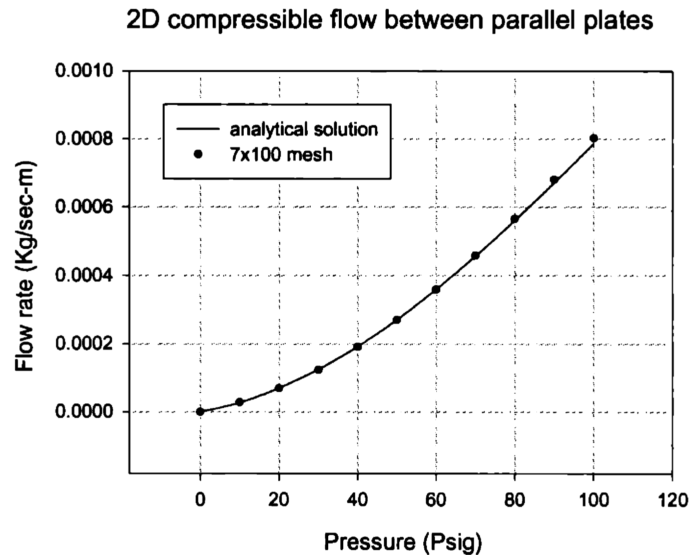


**Figure 5-5 Mesh convergence test. 2D CFD calculation results for flow between 2 μm gap parallel plates is compared with the analytical solution. A 7x100 mesh (7 layers across the flow and 100 grids along the flow) yields a good match.**

The accuracy of CFD calculations greatly depends on factors such as mesh refinement, boundary conditions, and the numerical schemes. The following approach was taken to confirm the code and to find the minimum mesh density that would produce accurate results. First, an axisymmetric (2-D) case that only includes the flow in between the bearing gap was calculated. Because an analytical solution is available for this case for both compressible and incompressible flows[4], this calculation provides a reference to optimize the mesh. The density of the grid was increased until a good match was obtained between the analytical and the CFD results. Because the flow path is only a few microns wide but several millimeters long, the critical mesh density is constrained by the dimension across the bearing gap. It was discovered that 7 mesh layers across the bearing gap were required to obtain an accurate solution (Figure 5-5). The CFD calculation error was less than 0.5% for cases with supply pressures up to 80 psi and was less than 2% at 100 psi. This error is within the degree of accuracy desired from these calculations.

In the next step, the effect of individual flow capillaries was included in a three-dimensional model (there are 8 capillaries in each bearing). The geometrical symmetry permitted us to

---

[4] Constantinescu, V.N., "Laminar viscous flow", Springer, 1995.

simulate only 1/16 of the circular bearing, saving calculation time. These calculations gave us information about the pressure distribution in the bearing gap. The baseline model could not provide 2-D pressure information because it assumes an axisymmetric flow. In Figure 5-6, we plot static pressure contours as the bearing gap varies. The source pressure is fixed for all three cases. The contour is generated on two planes for clarity: one is the mid plane parallel to the bearing pad surface, and the other is the r-z symmetry plane cutting through the capillaries. According to the Figure 5-6(a) to Figure 5-6(c), the average pressure in the bearing gap decreases with increasing bearing gap.

From Figure 5-6, it is clear that the original 8-capillary design does not produce an axisymmetric radial outflow. The distance between the capillaries is approximately twice as long as the distance between the capillaries and the bearing outer radius. Hence, a significant amount of flow first goes inward and then turns and comes out from the space between the capillaries. Figure 5-7 shows the effect of individual capillary restrictors on the velocity profiles. High velocity air jets turn at the end of each capillary, accelerates briefly and flowing out radially. In Figure 5-6, we can see asymmetric contours of static pressure due to the presence of individual capillaries. Low pressure area extend inward between capillaries, resulting in a reduction of average pressure in the gap and a decrease of the load capacity.

To optimize the bearing design, a matrix of simulations were performed, covering three different capillary diameters, with different feed pressures and bearing gaps. (Table 5) The length and location of the capillaries was not changed. (The parameters were narrowed down based on a parametric study using the baseline models.) In the CFD calculations, the surface integral of pressure is calculated and recorded together with the pressure at the inner radius. A total bearing force is then calculated based on these data and plotted against the bearing gap. In this way, a bearing force versus bearing gap curve can be generated for each design at different pressures (Figure 5-8, Figure 5-9) in order to show the relationship between net load, bearing stiffness and bearing eccentricity. As mentioned earlier, generally, the steeper the slope of the load-gap curve, the higher the bearing load capacity. The slope of the load-gap curve will approach zero when the bearing gap exceeds several microns. This is because the gap increase will not reduce the radial outflow resistance indefinitely, and the capillaries eventually take the entire pressure drop to fix a gap-independent bearing pressure. Therefore, continued increase in the total gap cannot raise the load capacity indefinitely.

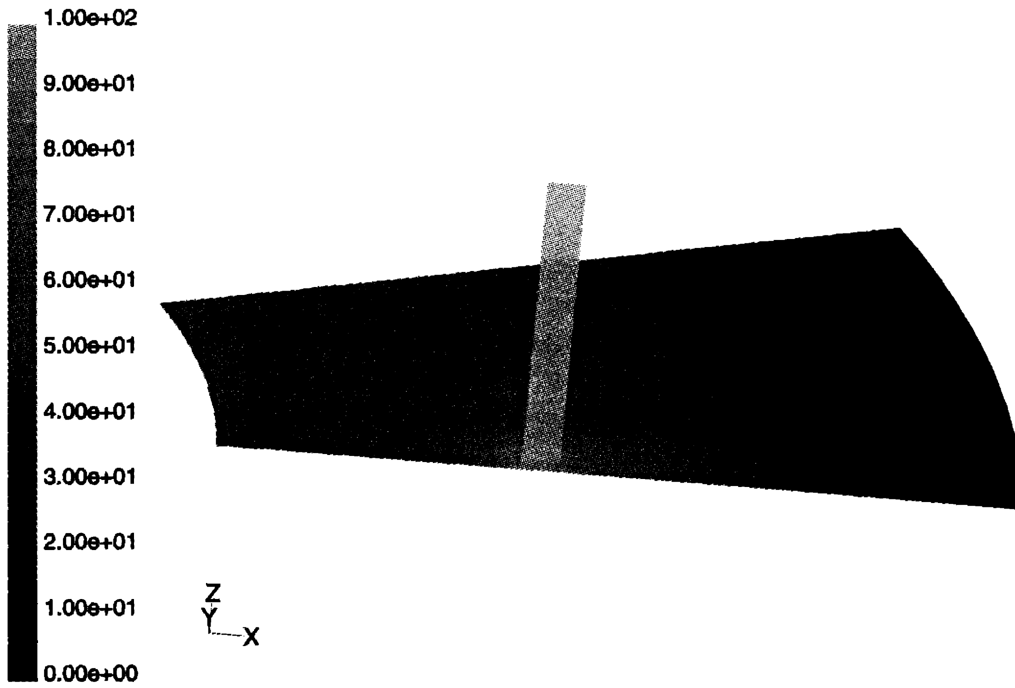


**(a)**

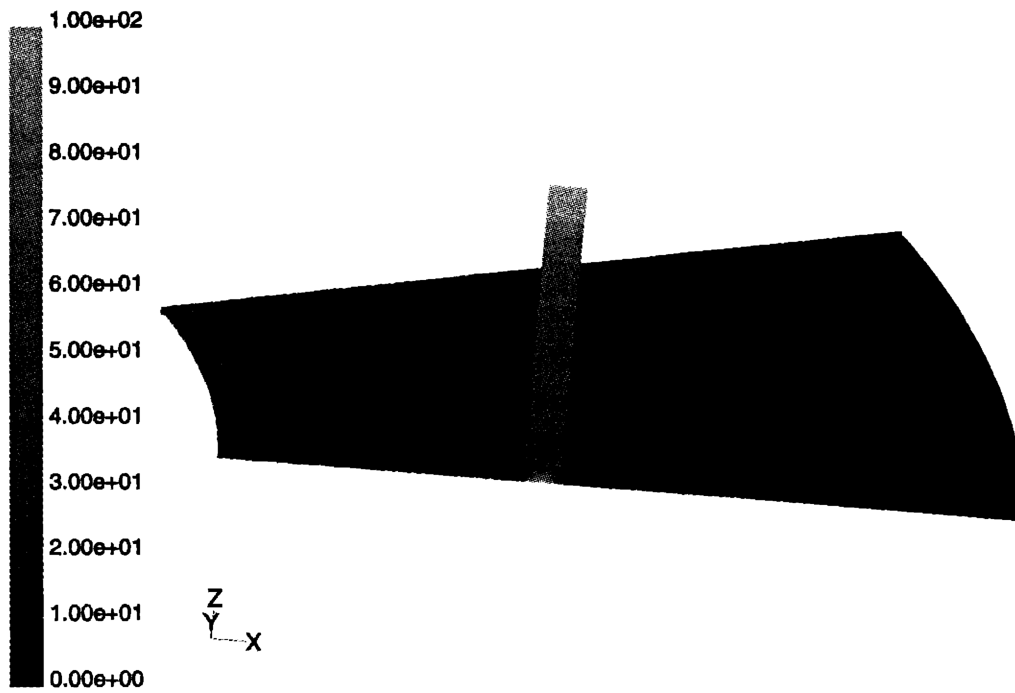


**(b)**

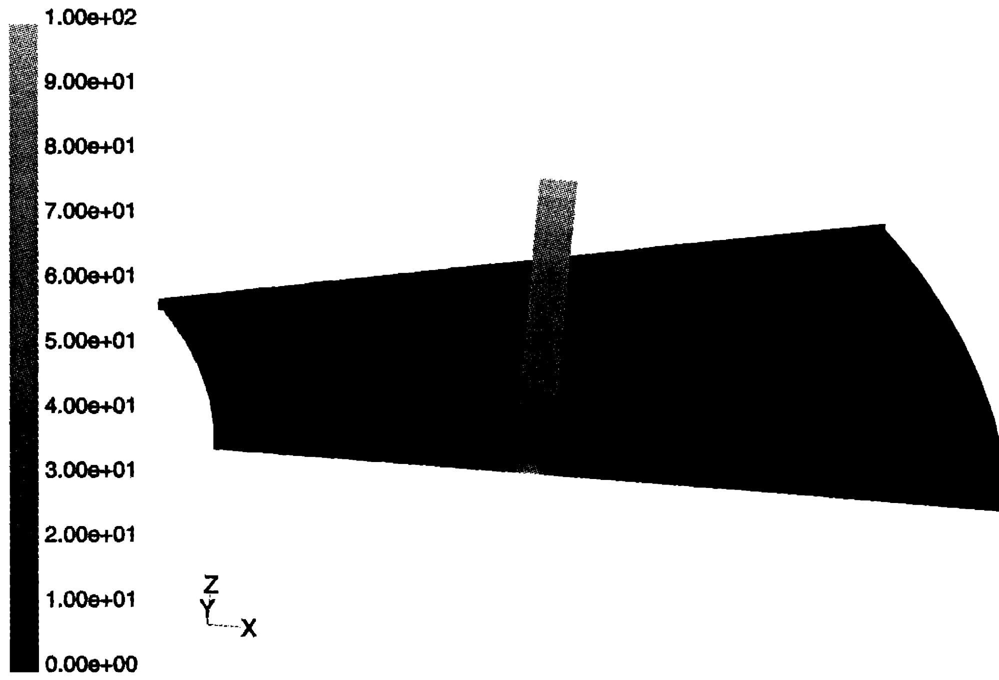


(c)

**Figure 5-6 Static pressure contours (in psig) of fluid in bearings with eight 12 μm diameter capillaries and a (a) 0.5 μm, (b) 3 μm, (c) 4 μm gap.**

| Capillary Diameter (μm) | Bearing gap (μm) | | | | | | |
|---|---|---|---|---|---|---|---|
| | 0.5 | 1.0 | 1.5 | 2.0 | 2.5 | 3.0 | 4.0 |
| 10 | X | X | | X | | X | X |
| 12 | X | X | X | X | X | X | X |
| 16 | X | X | X | X | | | X |

**Table 5 Simulation matrix for 8 capillary design. Flow for 6 feeding pressures were calculated for each design dimension.**

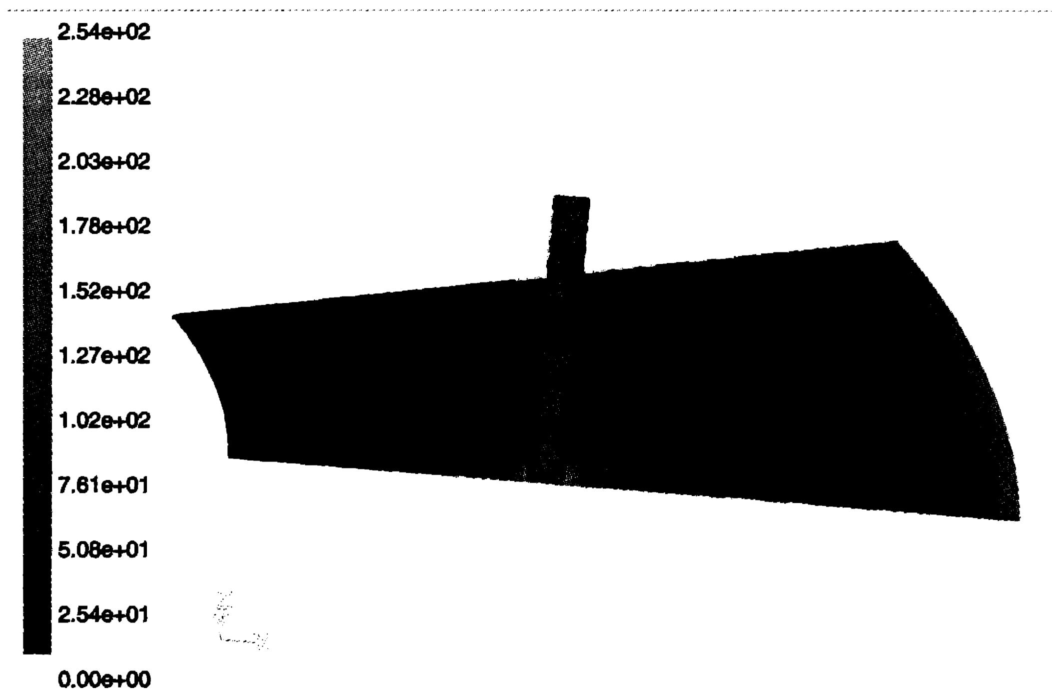


**Figure 5-7 Velocity contour of the 12 μm capillary design with 4 μm total gap bearing at zero eccentricity. The velocity unit is m/sec. The inherent restriction effect is clearly shown (high velocity flow near the exit of the capillary).**

The following steps were taken to derive stiffness from the CFD calculations. A symbolic equation fit to the calculated load-eccentricity curve, $F = f(\varepsilon)$, was first obtained. The net loading was obtained by combining the force acting on both sides of the bearing, that is, $Net_F = f(\varepsilon) - f(1-\varepsilon)$. We can also write the function *Net_F* in terms of rotor displacement instead of eccentricity. The stiffness-eccentricity relationship was obtained by taking a symbolical derivative of *Net_F* with respect to the displacement using the commercial package Mathematica. The calculated results will be shown at the end of the chapter after model verification.

As shown earlier in the pressure contour plots, the large distance between capillaries causes pressure drops which reduce the load capacity. Calculations were performed to explore the benefits of increasing the number of capillaries. As Figure 5-10 shows, when the number of the capillaries doubles, we obtain a much more concentric pressure pattern and an increase of bearing force (Figure 5-11(a) as compared to Figure 5-8). Moreover, Figure 5-11 shows that a reduction of capillary diameter (from 12 μm to 10 μm) together with doubling the number of capillaries further increase the slope of the force-eccentricity curve. As discussed earlier, this slope increase is desirable to improve the net force in application with an opposed bearing pair.

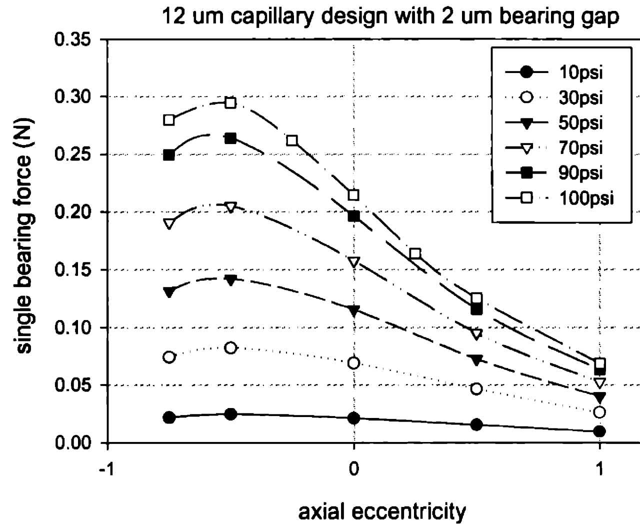


**Figure 5-8 Loading - position relationship for a 12 μm capillary bearing with a 2 μm bearing gap. As compared to the next figure, the curves have steeper slopes represent better stiffness of this design.**

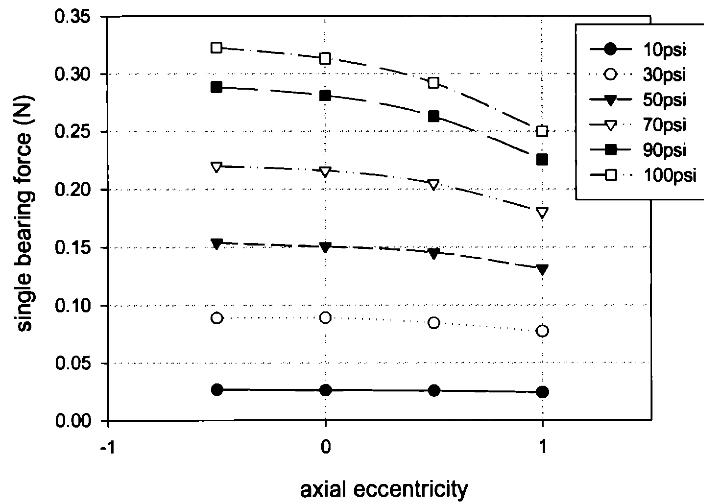


**Figure 5-9 Load capacity versus bearing position for a single thrust bearing based on 3D CFD simulations. The design values are: 16 μm diameter and 100 μm long capillary, bearing gap is 1 μm. There are 8 capillary restrictors per thrust bearing.**

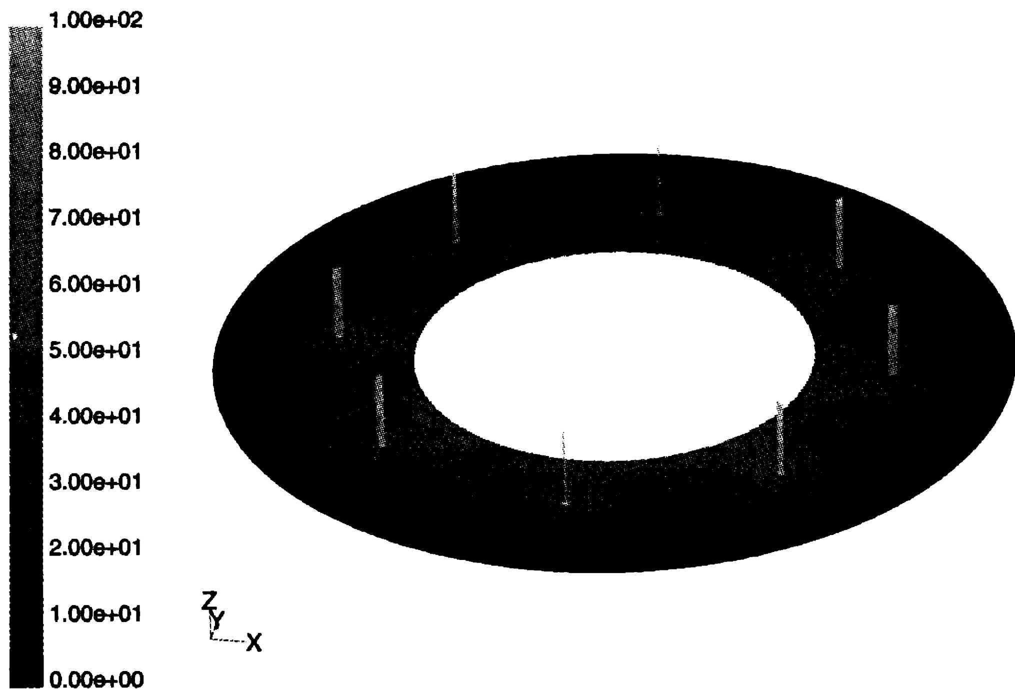


(a)

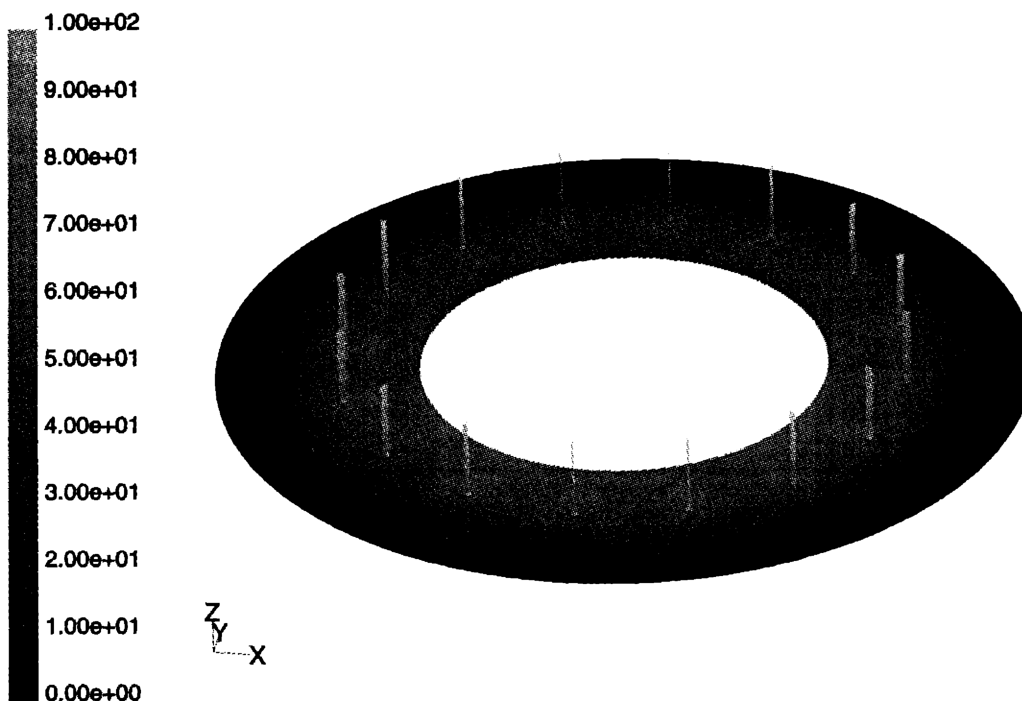


(b)

**Figure 5-10 Static pressure contour of bearing with (a) 8 capillary restrictors, and (b) 16 capillary restrictors. Both has 2 μm gap and 100 psig supply pressure. The 16 resitrictor model has more axisymmetric pressure contours and higher average pressure. To save calculation time, the center portion of the bearing was not simulation. The unit of pressure is psig.**

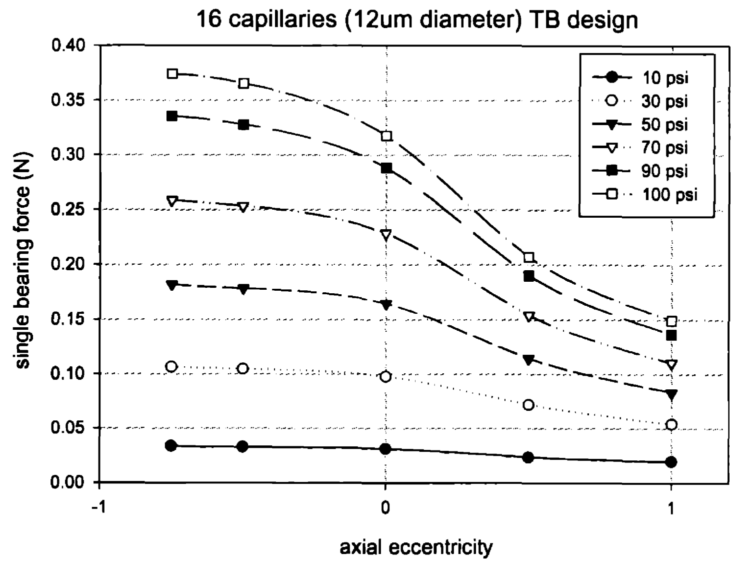


(a)

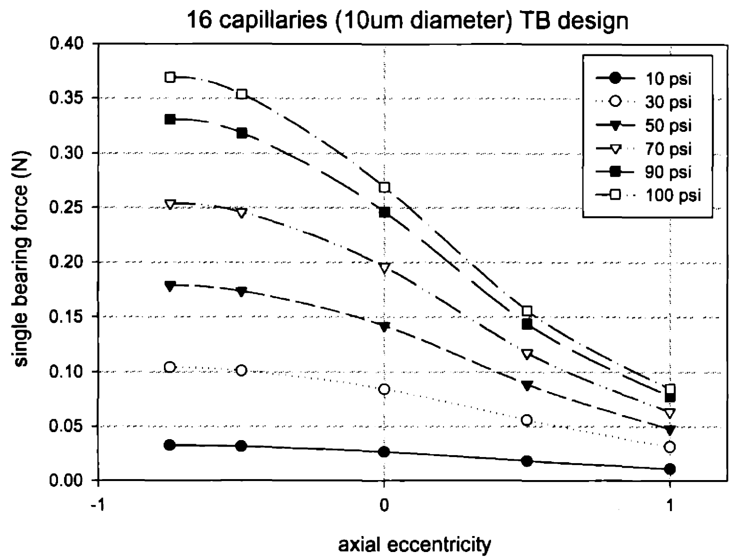


(b)

**Figure 5-11 Loading - position relationship of thrust bearings with 16 capillaries, and 2 μm bearing gap. Both show further improvement in the maximum loading compared to 8 capillary design. However, only for the 10 μm capillary case, the slope of the force-gap curves increases significantly over the 12 μm, 8 capillary design.**

### *Section 5.2 Pressure-flow characteristics*

Experimental performance evaluations are needed to evaluate the models. Generally, we need to measure several parameters to access the performance of the thrust bearings, including power loss, stiffness, and load capacity. These measurements are compared with results from calculations on the flow and pressure field. However, as indicated in Chapter 4, instrumentation difficulties on the micro bearing rig prevent us from directly implementing a force and a position sensor. We hence lack the capability of directly measuring the load acting on the rotor. Nevertheless, it does not prevent us from measuring the pressure-flow relationship and comparing it with the calculations. A good match of the flow rate raises the credibility of the model for predicting other performance factors. Since flow-resistance data gives us indirect information about bearing geometry, the tests mentioned above can also serve as additional steps to check whether the bearings are accurately built.

Pressure-flow relationships of the fabricated thrust bearing are shown in Figure 5-12, Figure 5-13, and Figure 5-14. In Figure 5-12, the experimental data are obtained from measurements of nine working samples from the fourth set of micro bearing rigs (build 4). As shown in the figure, the flow rate through the bearing is in the tens of standard cubic centimeters per minute (sccm) range. The simulation results based on the baseline model and the CFD calculation are also shown as comparison. (In the 'modified baseline model,' we add an additional parameter to increase the flow resistance to compensate the flow rate over-prediction caused by the axisymmetric flow assumption.) Each thrust bearing has a fixed gap before the laser-assisted rotor release etch because the rotor is held in the middle of the gap. After the rotor release etch, the rotor is free to travel axially and the maximum bearing gap is the sum of two pre-release-etch gaps. In these simulations, we assume the bearing gap to be the design value of 1 μm before the release-etch (pre-LAE), and post-LAE bearing gap to be 2 μm. The mismatch between the CFD result and the experimental data prior to LAE is believed to be due to the pre-LAE gap being not exactly 1 μm. If the FTB gap is about 1.1 μm before LAE and the ATB gap to be 0.8 μm before LAE, good pre/post flow matches are obtained. This gives us confidence in using the models to predict the flow rate or dimensions of the later builds.

Figure 5-13 shows the pressure-flow relationships for individual dies from build 6. In this build, there is a reduction of the aft thrust bearing gap, as indicated by the low flow rate. It is believed that the gap reduction is caused by wafer deformation in bonding as the shallow plasma etches are carefully performed to ensure an error of less than 0.1 μm (the gap is designed to be 2 μm). Post

LAE test results indicate that the capillaries are not clogged. According to the calculation, this reduction in the bearing gap will reduce the maximum loading of the bearing. After the laser-assisted rotor-release etch, we recover dies with pairs of symmetric bearings, as the sample 6-3 shows in Figure 5-13 (b). In this figure, only one device shows asymmetrical flows (6-8 in the same figure), which is possibly caused by variations in the capillary diameter across the wafer.

In build 7, a 16 capillary design replaces the old 8 capillary design to further raise the load capacity. (The results will be shown at the end of this chapter after model validation.) However, this build suffered from bonding and laser etching problems, which reduced the yield significantly. The pre-LAE flow measurements are shown in Figure 5-14. The difference in pre-LAE flow between forward and aft thrust bearing is reduced for most of the samples. However, large scatter of the flow data indicates a larger gap variation across the wafer due to poor bonding.

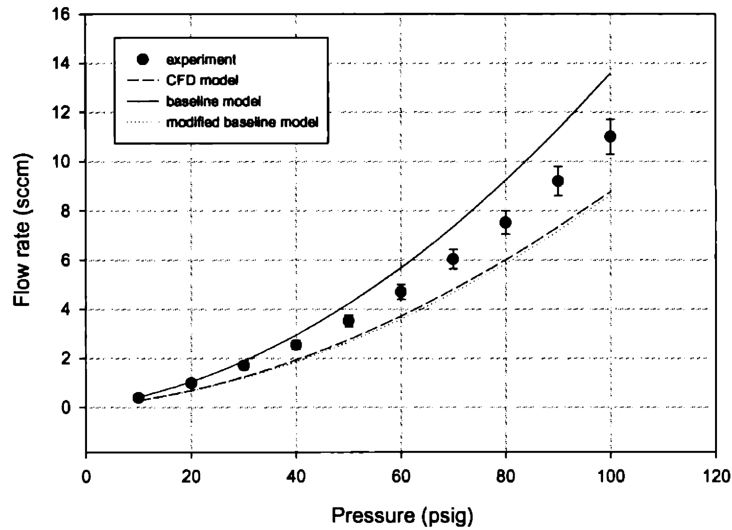


(a)

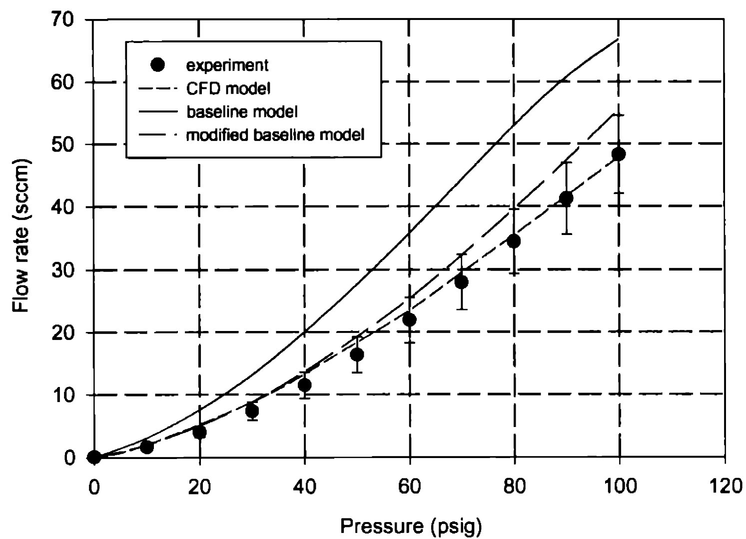


(b)

**Figure 5-12 Pressure-flow relationship of thrust bearings from build 4 as compared to simulations assuming eight 16 μm diameter restrictors. (a) FTB before LAE. (b) both FTB and ATB after LAE. Bars on the experimental data are standard deviation of measurements at each pressure.**

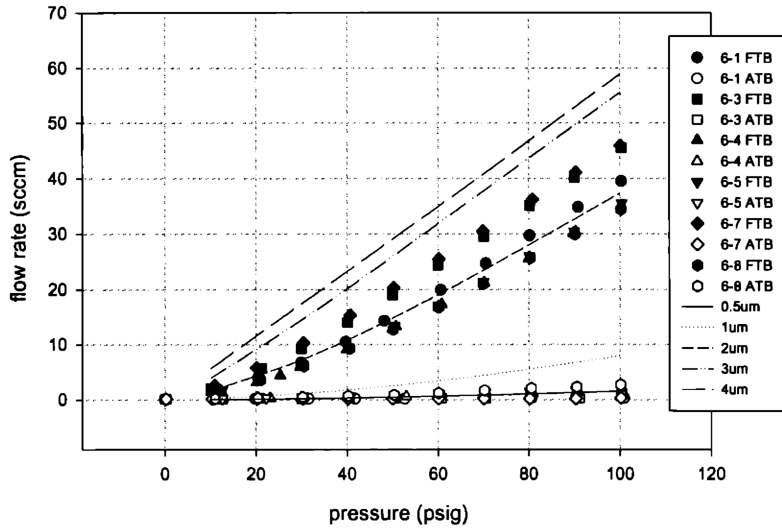


(a)

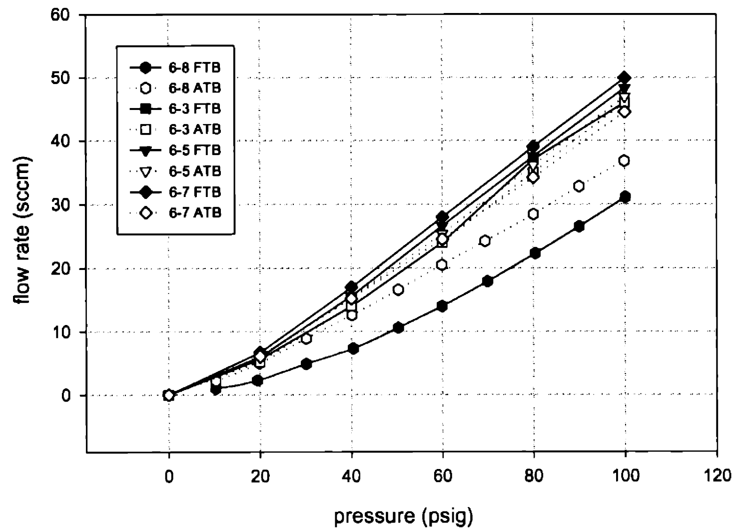


(b)

**Figure 5-13 (a) Pre-LAE thrust bearing flows from build-6. (b) Post LAE flow. (8 capillary design) The legend shows the label of each device.**

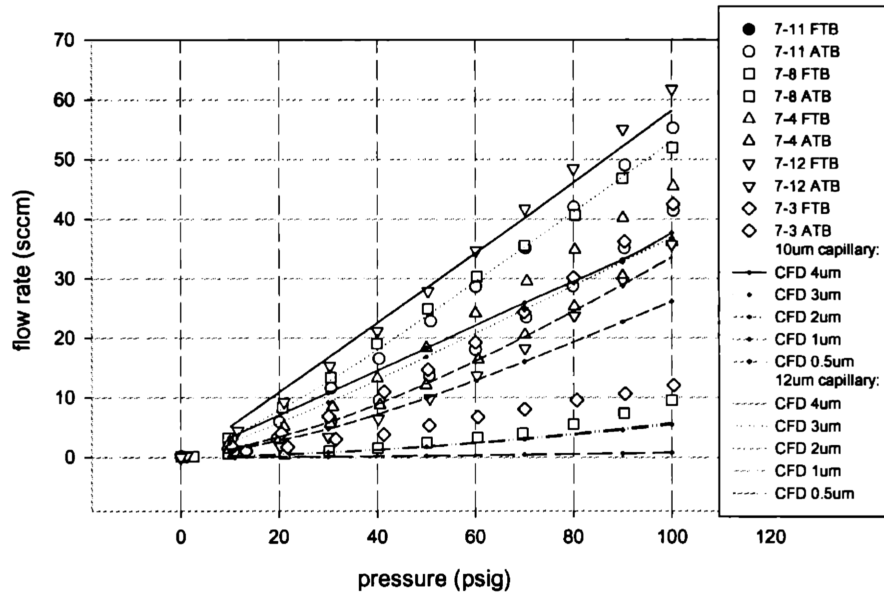


**Figure 5-14 Thrust bearing flow from build 7, 16 capillary design, pre-LAE.**

## *Section 5.3 Bonding yield characterization and dimensional deduction*

### 5.3.1 Bonding yield characterization

As stated earlier, the flow measurement can serve as a tool for deducing the dimensions of the microfabricated flow channels. Because the thrust bearing gap is defined by the shallow plasma etch and a wafer bonding, post-bonding flow measurements on the thrust bearings can provide us with information about the quality of the bond. Figure 5-15 shows a bar plot of thrust bearing flow measurements for all 12 devices across a wafer after the last bonding step and dicing but before laser-assisted etch. The bottom and top of each bar represent 5% and 95% of the data. Three lines are drawn inside each box. The middle line represents the median value of the data, while the lower and upper dashed lines represent 25% and 75% of the data, respectively. With the help of forward thrust bearing (FTB) measurements, we identified that two dies (4-2, 4-11) were not bonded properly, and that one die (4-5) has plugged holes, possibly due to exececssive compression during bonding.

The data scattering of the aft thrust bearing flows (ATB) is slightly greater than the FTB. This is due to the packaging clamping, as has been discussed in chapter 4. Repeated measurements show that the 10 dies have an average ATB flow rate of 4 to 5 sccm at 100 psig.

.

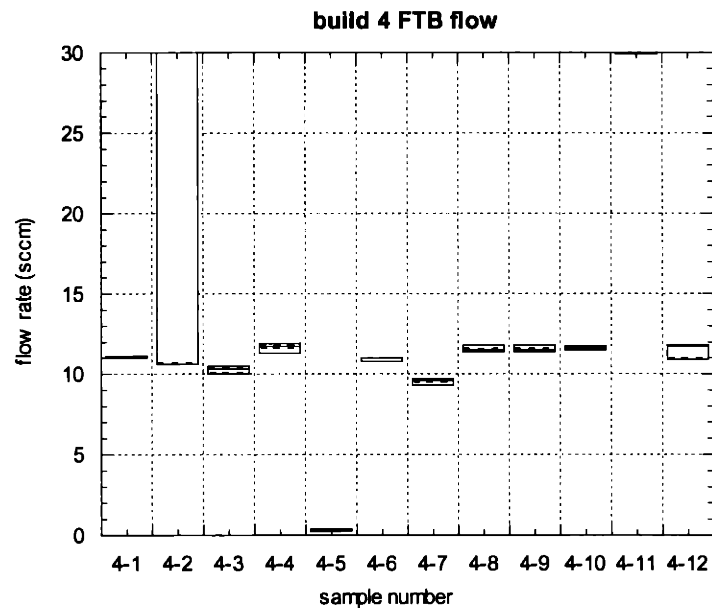


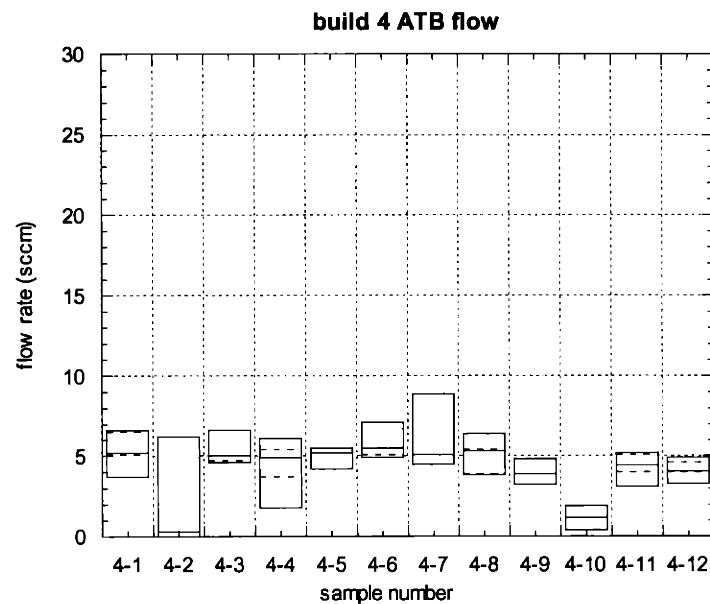


**Figure 5-15 Yield characterizaton based on the thrust bearing flow measurement. Flow measurements are taken at a source pressure of 100 psi. From the FTB data, we can exclude 4-2 and 4-11 from good dies due to the usual high flow rate, and exclude 4-5 due to plugging. All ATB flow data show lower flow rates due to bonding issues and larger scattering due to packaging. We can further exclude 4-10 viewing its low flow rate.**

### 5.3.2 Thrust bearing dimensional deduction

We can solve for the as-fabricated capillary diameter and the bearing gap based on the results of two flow measurements. Using the CFD results, we can construct a contour plot that illustrates the relationship between the flow rate, the capillary diameter and the bearing gap at a fixed pressure (Figure 5-16). Although the thrust bearing flow rate is a function of four parameters, namely, capillary length, diameter, bearing gap, and the pressure, we fix the capillary length for simplicity. After finding an numerical fit to the contour plot ($4^{th}$ order Chebyshev polynomials are used), the following is the procedure for obtaining the dimensional estimation by using these flow contours.

1. Perform flow measurements of both the FTB and the ATB before LAE at 100 psi (2 measurements).
2. Repeat flow measurements again for both FTB and ATB with the rotor pushed all the way to recover the maximum gap after the LAE rotor release. When one bearing is set to zero pressure and the other to 100 psi, either thrust bearing should see the maximum gap.
3. Use the four measurement results to solve for the capillary diameter and the gap. First, assume a maximum gap. Knowing the maximum gap and post-LAE flow rates, one can get the capillary diameter of the contour from the fit equation.
4. Since the capillary diameters do not change with rotor position, one can then use the pre-LAE flow rates and the obtained capillary diameters to calculate the pre-LAE gaps.
5. Adding together the calculated pre-LAE gaps from FTB and ATB, the sum should be equal to the maximum gap. Otherwise, change the assumed maximum gap go back to step 3.

We can extend this idea further to characterize other critical dimensions of the bearing rig, as will be explained in the next section.

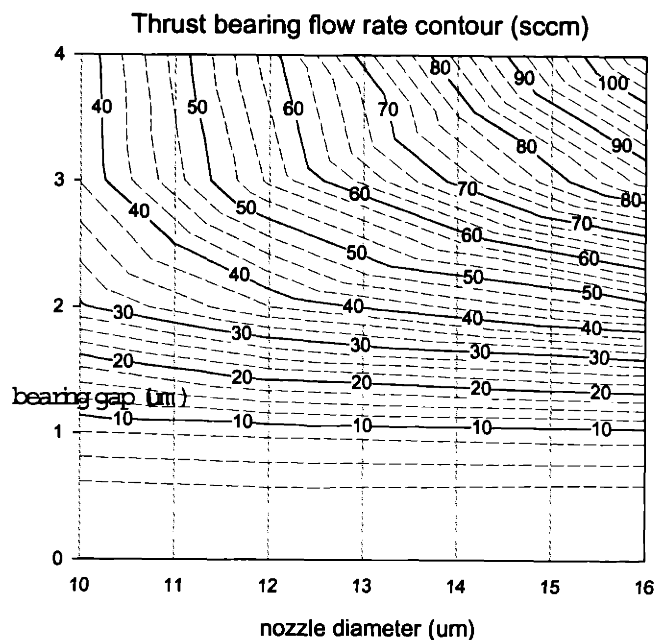


**Figure 5-16 Contour plot of flow rates as related to bearing capillary diameter and gap. These data are calculated by CFD assuming a design of 8 capillaries of 100 μm length.**

## 5.3.3 Journal bearing axial flow measurement

One way to non-destructively determine the dimensions of a micro-fabricated fludic device is to measure the flow resistances. Flow resistance is defined by the ratio of pressure drop to flow rate. The resistance is directly related to the size of the critical features.

As shown in Figure 5-17, we can identify many flow resistances inside the device. In addition to the thrust bearings, there is a journal bearing axial through flow resistance that is a function of the gap width and length, there are losses associated with the flow on the backside of the rotor, and there is resistance related to flow through the turbine blades and inlet guide vane.

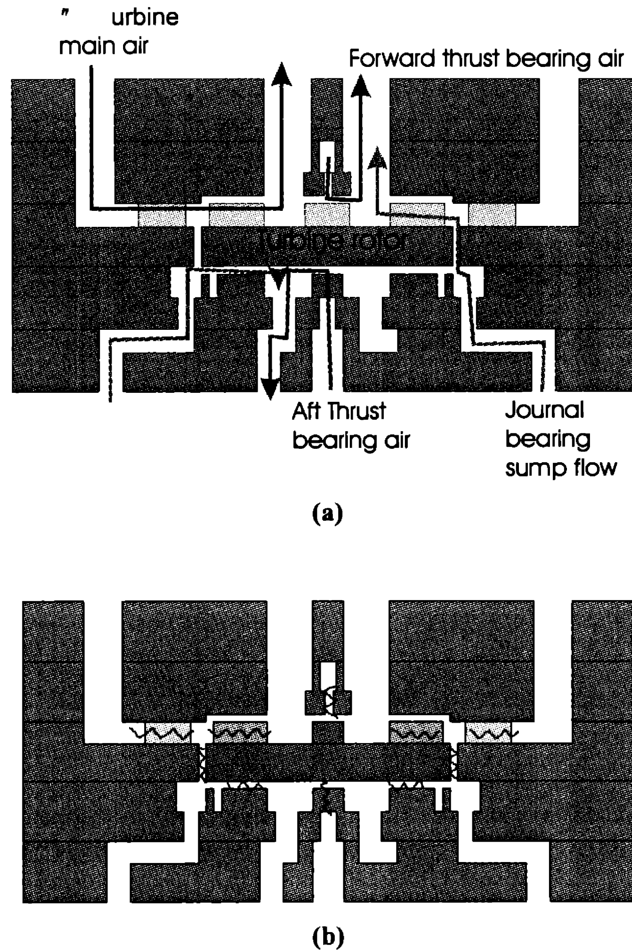


**Figure 5-17 (a) Turbine rotor flow path and (b) main flow resistances in the micro bearing rig.**

By properly plugging and venting the ports that lead to the package, we can force the air to flow in a particular direction. With a matrix of tests that involves plugging and venting different ports, the flow resistances in the device can be measured, giving important information about the devices' internal dimensions.

The most important parameter that requires in-situ dimensional checking is the journal-bearing gap because it is critical to the bearing performance. As described in chapter 2, there are three flow sumps that connect to the journal bearing gap to produce side loading and hydrostatic loading. We can take advantage of this design to measure internal flow resistance by applying equal pressure to the three sumps and measuring the flow rate. Because the bearing gap is the dominant flow resistance along the flow path (gap width is fifteen times smaller than other

internal channels along the same path), we can estimate the gap size of the tested devices by matching the measurement to simulation results.

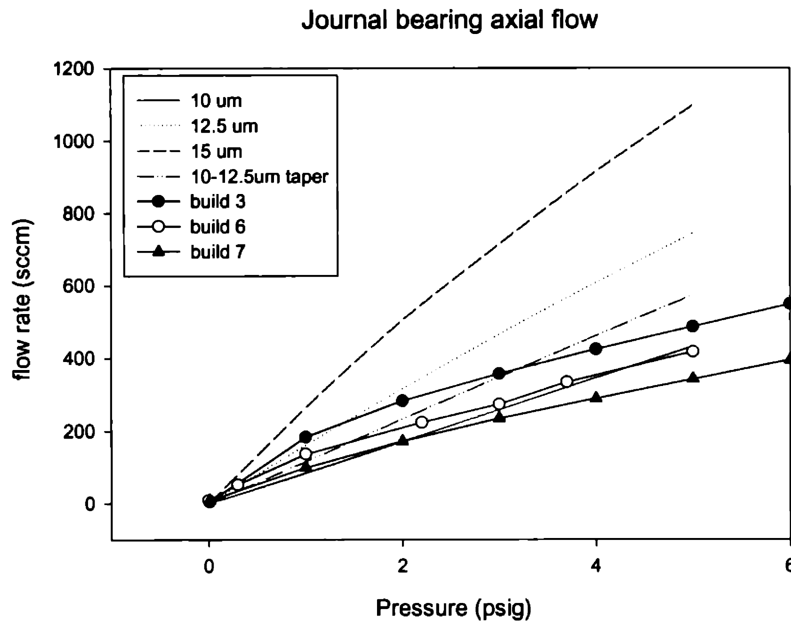


**Figure 5-18 Journal bearing axial cross flow. The flow rate is measured before the LAE when the journal bearing gap is fixed. The CFD calculations are shown in lines for comparison.**

Figure 5-18 shows the flow measurement of axial journal bearing flows for 3 different builds as compared to CFD simulation results from Fluent. The calculations are performed using an compressible axisymmetric model in Fluent. Four different cases are simulated as references, including straight 300 μm long gaps that are 10, 12.5, 15 μm wide, and one with a 2.5 μm taper that is 10 μm wide on the small side. The flow rates are measured before LAE when the rotor journal bearing gap is still fixed. Four to six devices are measured for each build and the sum of the measured flow rates from three different sumps is plotted. The experimental results imply a steady reduction in the gap size from build 3 to build 7, which was one of the goals in the later builds. The die to die measurement variation is very small, as shown in the Figure 5-19. Scanning electron micrographs of etched bearing cross-sections for each build are shown in Figure 5-20. From these SEM photos, we conclude that the model does not perfectly agree with measurements. This mismatch suggests that the model does not adequately describe the geometry

or flow process. With careful calibration of the model, this flow measurement could be a valuable non-destructive measure of the journal bearing dimensions.

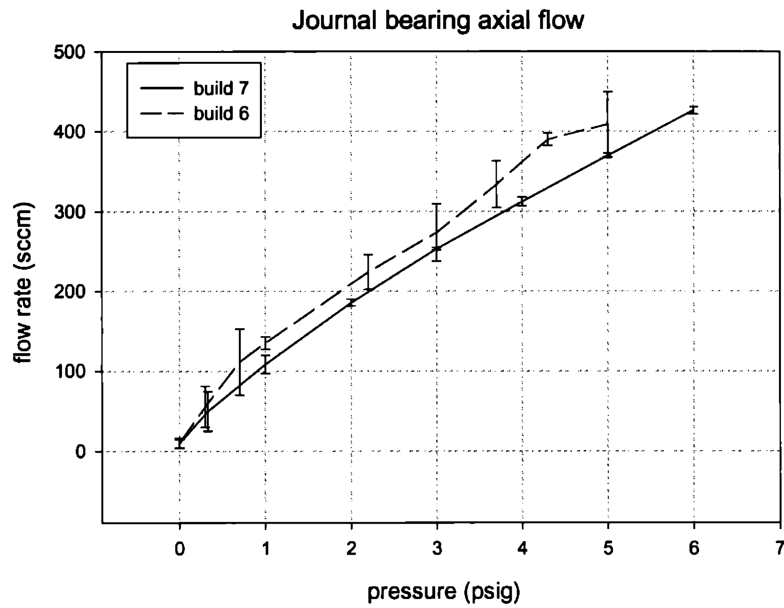


**Figure 5-19 Experimental results of the JB axial flow from build 6 and build 7. Results are based on measurements from 4 samples from each build and it shows an improvement in repeatibility across samples for this latest build. The bars represent the standard deviation of the measurements.**

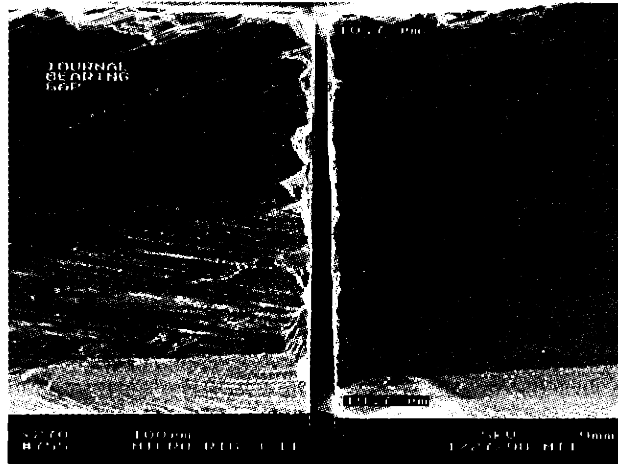


(a)

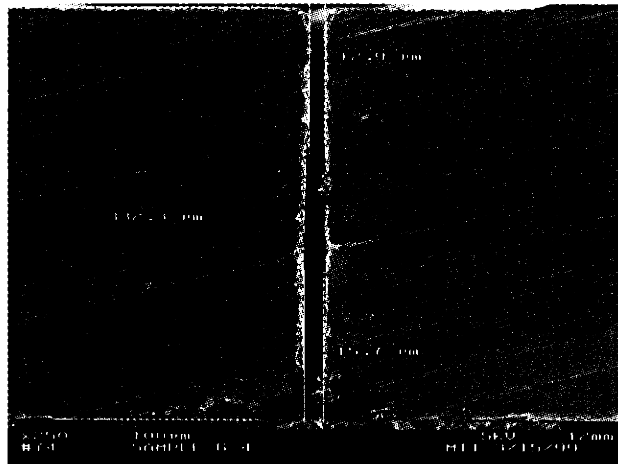

(b)

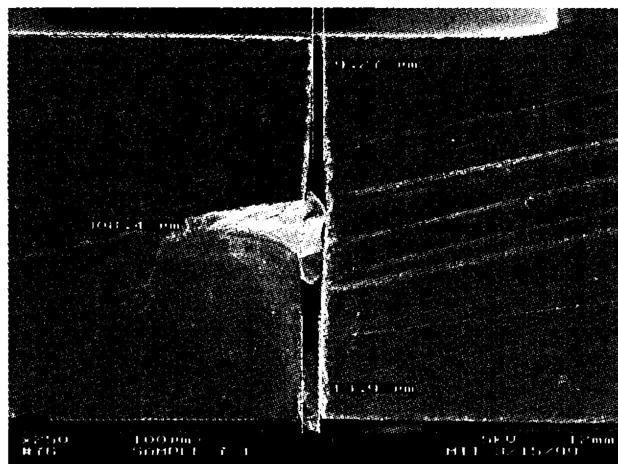

(c)

**Figure 5-20 Journal bearing gap shown by cross-sectional SEM: (a) build 3, (b) build 6, (c) build 7.**

### *Section 5.4 Rotor axial position test*

The load/torque applied to the turbine can be measured with separate sensors in large-scale devices. In these cases, the force readout and the position data provide direct information about the bearing load-capacity and the stiffness. At the millimeter size of the micro turbine the space for instrumentation is constrained, as discussed in Chapter 4.

In the previous section, we have shown a match of the flow rates between experiment and simulation. Nevertheless, the validity of the load/stiffness calculations should still be further strengthened by experimental validation. We have designed and performed a simple test to provide indirect information about the bearing stiffness and stability. Called the "rotor axial position test", the procedure is described as follows. As indicated in Figure 5-21-1, one bearing out of the thrust bearing pair (for example, the bottom bearing in the figure) is first pressurized to a fixed pressure, $P_a$. Thereafter, the other thrust bearing is pressurized, and the flow rates of both thrust bearings are monitored at the same time. Initially, the top bearing will have a flow rate near zero because the rotor is completely clamped to the top. As the source pressure of the top bearing ($P_f$) increases to push down the rotor, its flow rate will increase due to the increasing gap shown in Figure 5-21-2. The bottom flow rate will drop due to a decreasing gap even though the $P_a$ remains the same. If we keep raising $P_f$, the flow rates on both sides will equalize at a certain pressure. This pressure should be equal to $P_a$ if the pair of bearings are symmetric. Continuing to increase $P_f$ will push the rotor down, and the gap change will be reflected by a diminishing flow rate on the bottom side as shown in Figure 5-21-3.

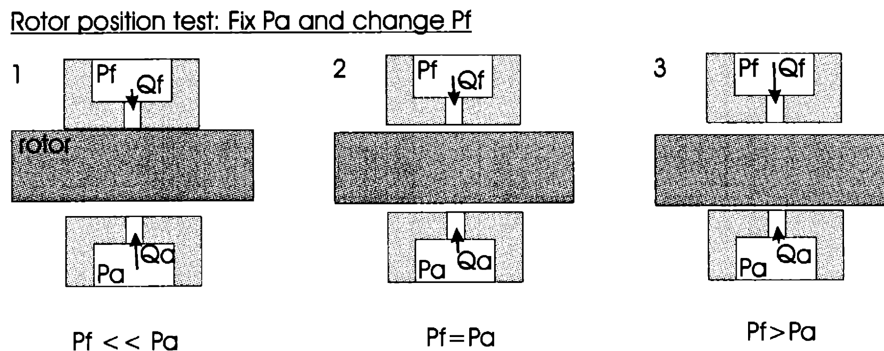


**Figure 5-21 Rotor axial positioning test.**

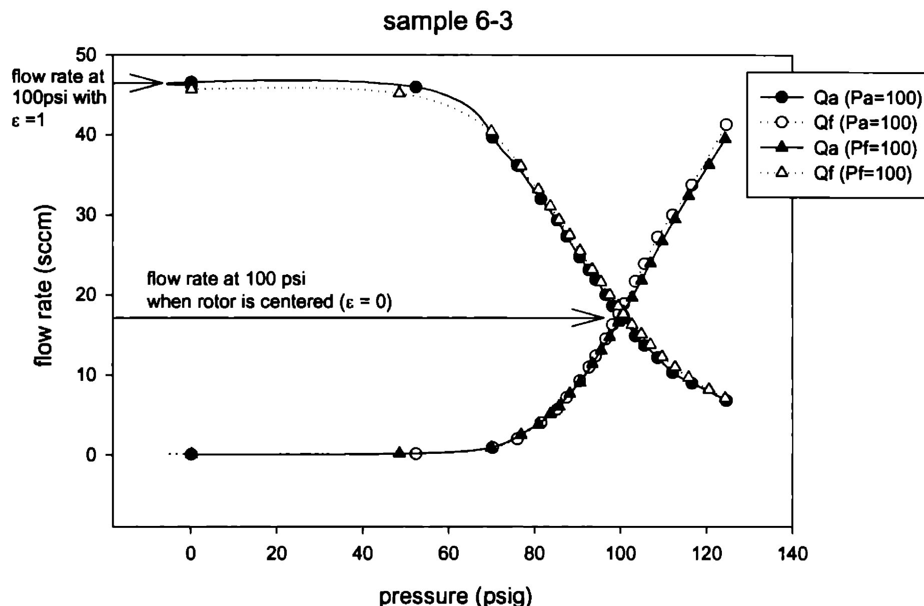


**Figure 5-22 Rotor axial positioning test result from sample 6-3. The circles represent results from a test during which the aft source pressure ($P_a$) is fixed at 100 psig, and the triangles represent results with forward source pressure ($P_f$) fixed at 100 psig. The x-axis refers to the non-fixed source.**

To check the bearing symmetry we can repeat the test above by switching the side with a fixed pressure. For example, Figure 5-22 shows the result form two tests, one with fixed aft thrust bearing pressure ($P_a$) and varying forward thrust bearing pressure ($P_f$), and one with fixed $P_f$, and varying $P_a$. The same results are obtained from this two test, proving that the bearing pair is symmetric. For an asymmetric bearing the balance point shifts (Figure 5-23). We infer in this case that the forward thrust bearing (FTB) produce higher force than the aft thrust bearing (FTB) as it takes a $P_a$ of 104 psig to balance the FTB, which is fed at 100 psig. Other than dimensional variations between two bearings, one possible reason for this asymmetry is the aft exhaust plenum back pressure, which introduces additional force on the rotor aft side such that the ATB would appear stronger. Physical contact on the journal bearing wall, resulting from tilted rotor or a particle, will also introduce an additional friction force. Among these possibilities, the author believes that friction caused by wall-contact plays the main role in introducing such asymmetry. This belief is supported by repeated tests on the same device, which have shown different asymmetries. Furthermore, the fact that the ATB is not always the stronger bearing excludes the possibility that the shift is caused by aft-side back-pressure.

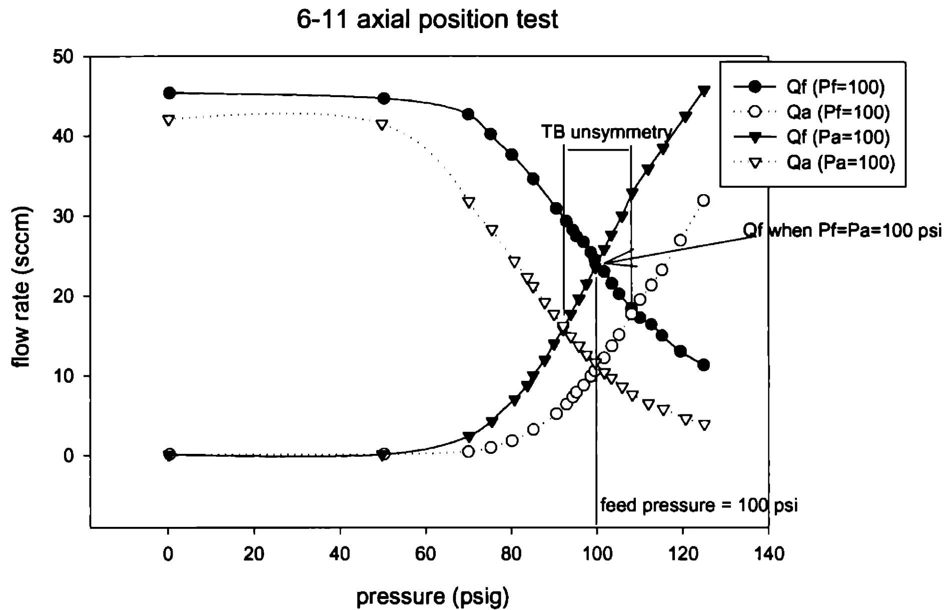


**Figure 5-23 Asymmetry results from rotor axial position test.**

Figure 5-24 shows repeated rotor axial position tests performed at different 'fixed pressure'. Five tests are shown for two devices, one from build 4, and the other from build 6. One can see that the pressure working-range, in which the flow rate is sensitive to pressure adjustment, increases significantly from sample 4-6 to sample 6-7. This improvement holds at any given fixed pressure, and can be explained by the improved bearing compensation considering the following argument. In Figure 5-24, the forward thrust bearing force is proportional to the forward thrust-bearing pressure. Hence the adjustment of forward thrust-bearing pressure changes the force applied to the aft thrust-bearing. Because the aft thrust-bearing is fed by a fixed pressure, its gap width, which also defines the rotor position, is reflected by the flow rate change. Therefore, the fact that the thrust bearing flow rate varies smoothly over a wider range of pressure indirectly suggests the bearing compensation improvement.

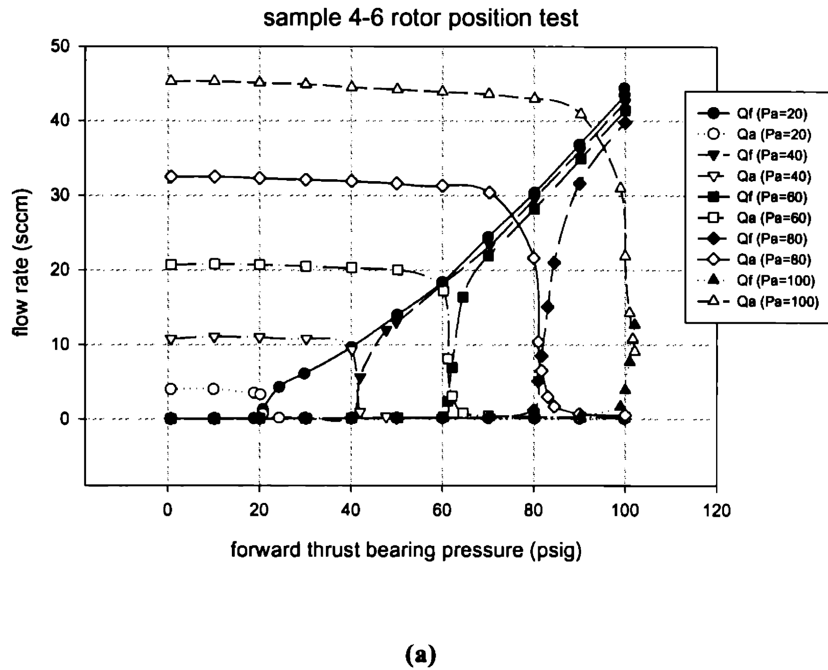


**(a)**

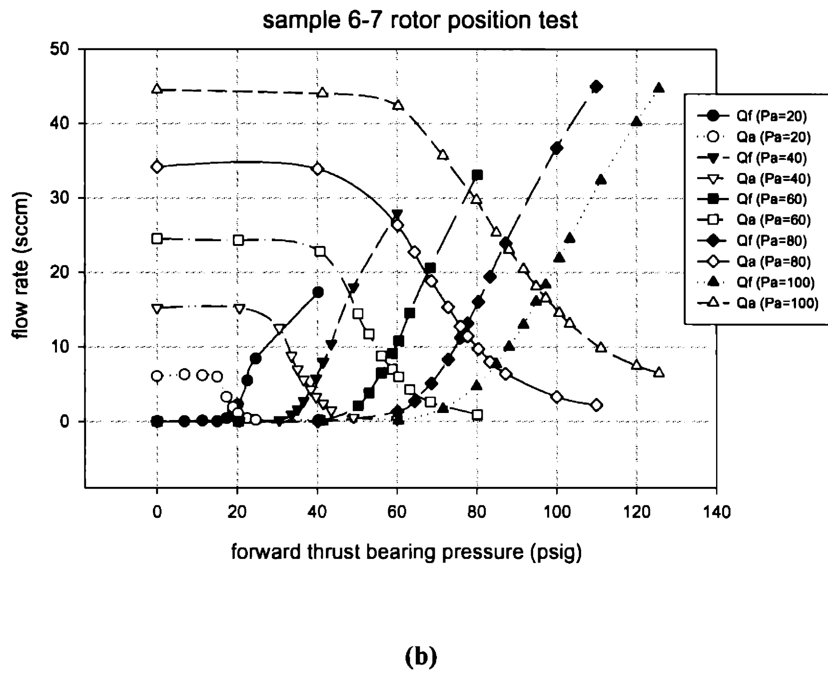


**(b)**

**Figure 5-24 Rotor axial position test from (a) sample 4-6, and (b) 6-7. Each pair of curves represents one test during which the aft thrust bearing pressure is held constant and the forward thrust-bearing pressure is adjust to move the rotor down. Five tests were done with the fixed pressure set from 20 psig to100 psig.**

The goal in performing the rotor axial position tests is to further explore the model. One test of the model is matching the rotor position test with the force calculation. Given the fixed source pressure $P_x$, the following procedure is performed to generate simulation data to match the experiments:

1. Specify a rotor position. Use this position and the known fixed pressure $P_x$ to calculate the bearing force F on the bearing that has fixed source pressure.
2. Using the rotor position and the calculated force F from part 1, we calculate the pressure $P_r$ that is required for the other thrust bearing to balance F. (The rotor is at equilibrium at any position during the test.) This calculation is performed using an equation obtained from fitting a $4^{th}$-order Chebyshev-polynomials to the CFD results.
3. Use the acquired $P_x$, $P_r$ and the specified position to calculate the flow rate on both bearings.
4. Specify a new position and go to step 1. Repeat until the rotor has traveled from one bearing to another.
5. Plot the flow rates against $P_r$ and compare the results with experiments.

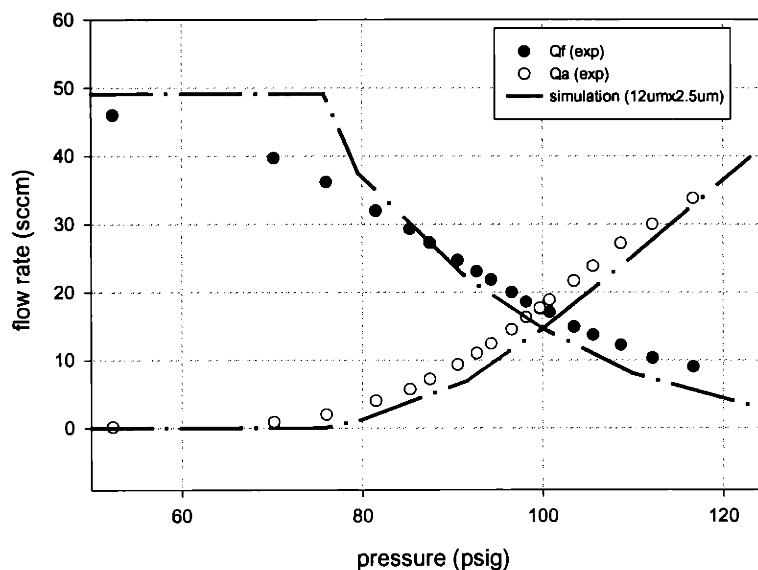


**Figure 5-25 Experiments (from Figure 5-22) vs. simulations for the rotor axial positioning test.**

Figure 5-25 shows the comparison of simulation and experiment. The slope is well captured, confirming the accuracy of the model in predicting the loading. In the calculation, a 2.5 μm total bearing gap is assumed (increasing the gap will raise the flow rate at 100 psi).

The validated CFD model can be use it to help with our design and to predict performance associated with the devices that have been built. Low stiffness and load were discovered in the first bearings, which had 16 μm diameter capillaries and 1 μm bearing gap. This result was consistent with the baseline model predictions. After evaluating the trade-off of performance and fabrications capability, we changed the design to 12 μm capillaries and 2 μm bearing gap. Later, we doubled the number of the capillaries to further raise the load capacity, and reduced the diameter of the capillaries to 10 μm. The expected improvement in load capacity and stiffness is shown in Figure 5-26. Figure 5-26 shows the load capacity and stiffness versus bearing gap for four designs: eight 16 μm diameter capillaries, eight 12 μm capillaries, sixteen 12 μm capillaries, and sixteen 10 μm capillaries. A boost in the load capacity can be obtained without losing stiffness. This is achieved by doubling the number of capillaries from 8 to 16, reducing the capillary diameter to 10 μm, and increasing the total gap to 4 μm.

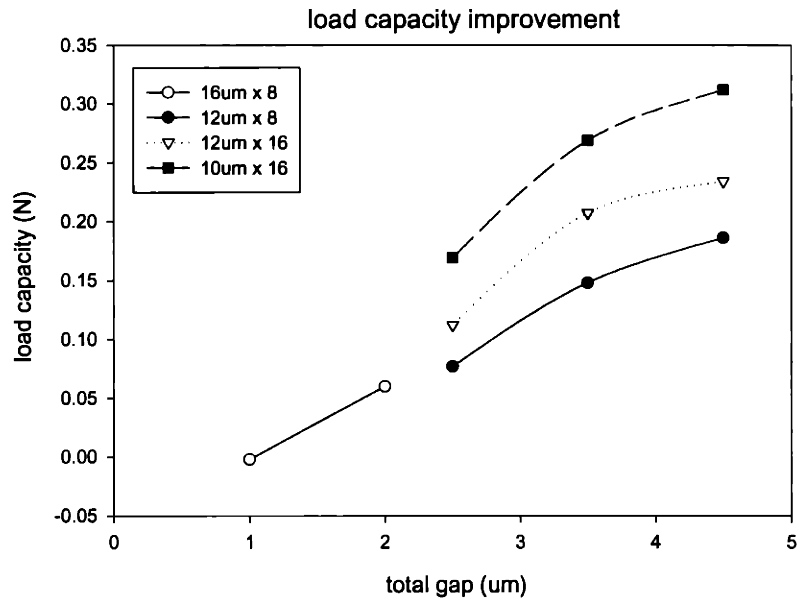


(a)

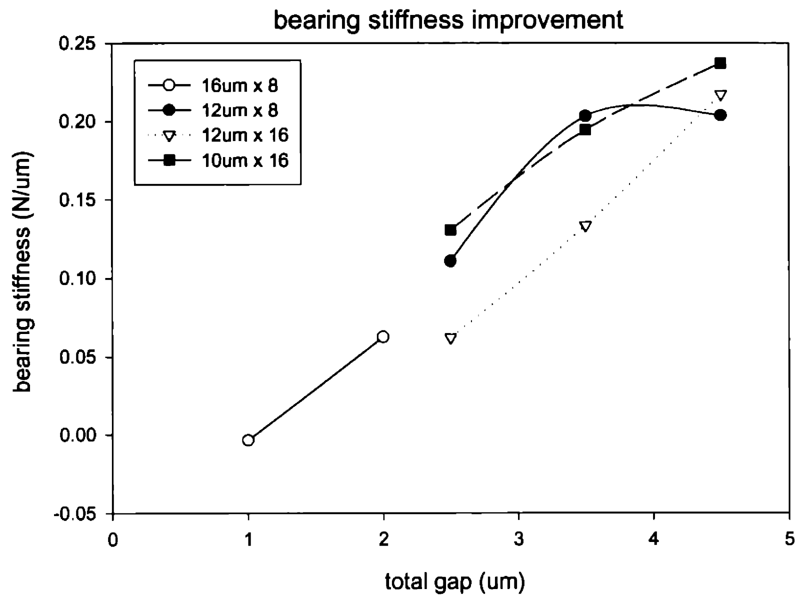


(b)

**Figure 5-26 Bearing performance improvement in (a) load capacity (N); (b) stiffness (N/μm) as indicated by CFD calculations for a pair of opposed bearings. Effects of increasing the gap, the number of capillaries, and reducing capillary diameter are shown.**

### *Section 5.5 Summary*

In this chapter, we first present two models that are used to help understand the thrust bearing performance. The baseline model is a valuable tool for quick parametric studies, and the CFD model provides detailed information about 3D flow field and pressure distributions. These models are validated through comparisons to experimental flow measurements, and then are used to improve performance of newer designs.

We also present the concept of using the internal flow measurement as a non-destructive means of characterizing bonding and journal bearing gap. This method provides a way to perform in-situ trouble-shooting on the micro-bearing rig.

A rotor axial position test is designed to provide data to confirm the accuracy of the force prediction of models. The model is then used to calculate load capacity and stiffness, parameters that cannot be directly obtained experimentally. It is concluded that later generation builds have improved load capacity and stiffness. These improvement can be associated with spin tests results, which will be shown in the next chapter.

# Chapter 6

# Rotor Spin Test

In this chapter, we will summarize the spin test results. Spin testing is an on-going effort and we have not reached the targeted speed of the micro-engine project within the time frame of this thesis. However, we have demonstrated stable micro air-bearing operation, and the results should improve in the future, together with improvement of dimensional control and instrumentation.

## *Section 6.1 Hydrostatic and hydrodynamic setup*

Even though the bearing was designed to run in hydrodynamic modes, a hydrostatic operation mode associated with this geometry was discovered from the testing of macro bearing rig (D.J. Orr. [1]) This hydrostatic operation relies on a pressure-driven axial leakage flow through the journal bearing. There is an entrance region in the gap before the flow becomes fully-developed, and the entrance length is proportional to the width of journal bearing gap. A sketch of the pressure profile is shown in Figure 6-1. The pressure drops rapidly in the entrance region and slowly afterwards. Orr has shown that a smaller bearing gap corresponds to shorter entrance length and higher average pressure. Since the net radial force acting on the rotor comes from an integration of the journal bearing pressure, this axial through-flow provides a hydrostatic stiffness to center the rotor. To take advantage of this effect experimentally, we can set a constant flow across the bearing gap by connecting the 3 flow sumps to uniform pressure that is above the inter-row pressure. In this way, a hydrostatic stiffness will be developed before the rotor starts spinning.

Due to its low-speed stiffness, the hydrostatic operation is useful for starting the rotor at low speeds. At higher speeds, the hydrodynamic mode is still favored in the current design because current models suggest that the hydrostatic force may not provide adequate load capacity. According to a first order calculation [2], the required pressure ratio across the journal bearing will be many times higher than the maximum turbine pressure ratio in order to meet the required load capacity in hydrostatic mode. A large axial force will also be produced, exceeding the loading capacity of the thrust bearings.

During a hydrostatic spin test, we set all three journal bearing sumps to equal pressure, and during a hydrodynamic spin test we set an unequal pressure between high and low sumps. In the following sections, we will summarize results from both testing modes.

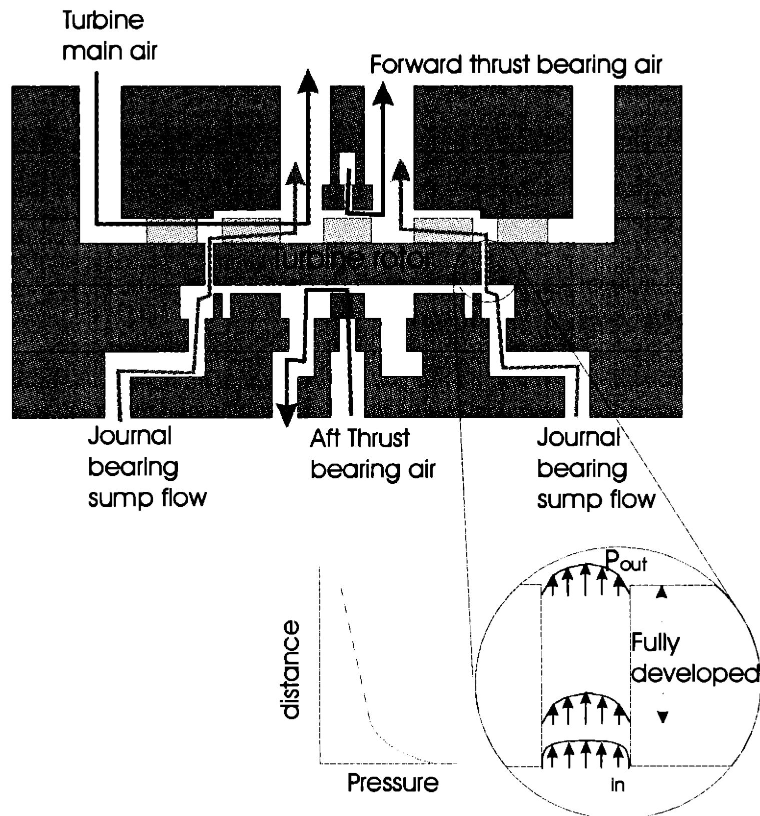


**Figure 6-1 Hydrostatic journal bearing operation based on 'entrance length'.**

### *Section 6.2 Hydrostatic testing results*

Although the hydrostatic mode should work in theory, early testing was not successful. It was difficult to start the rotor, and once started, it would crash within tens of milliseconds (Figure

6-2b). The rotor accelerated to 30-60,000 rpm within that time, but the after crash it came to a complete stop. Occasionally, the rotor seized and would not start after the crash.

Later testing has established continuous stable operation [3]. In the test shown in Figure 6-3, the maximum speed reached is about 110,000 rpm. Improved thrust bearing performance has helped simplify the testing operation allowing the operator to focus on the journal bearing stability (thrust bearing flow monitoring is still required at speeds above 100,000 rpm). Starting at low pressure (0.1 psig) has yielded the greatest success. These results suggest the validity of a stable hydrostatic operating mode. The bearing rig has operated in this lubrication mode for hours.

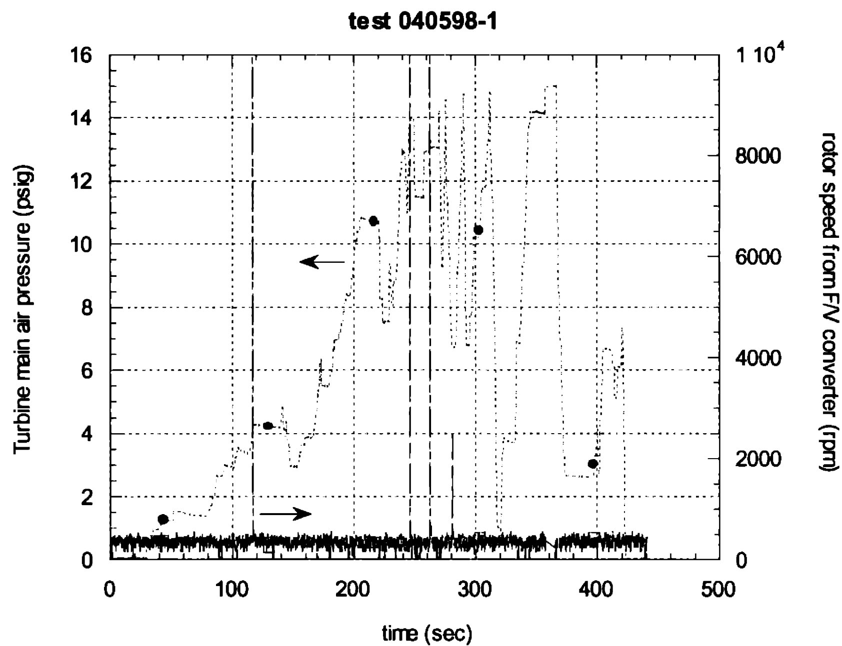


(a)

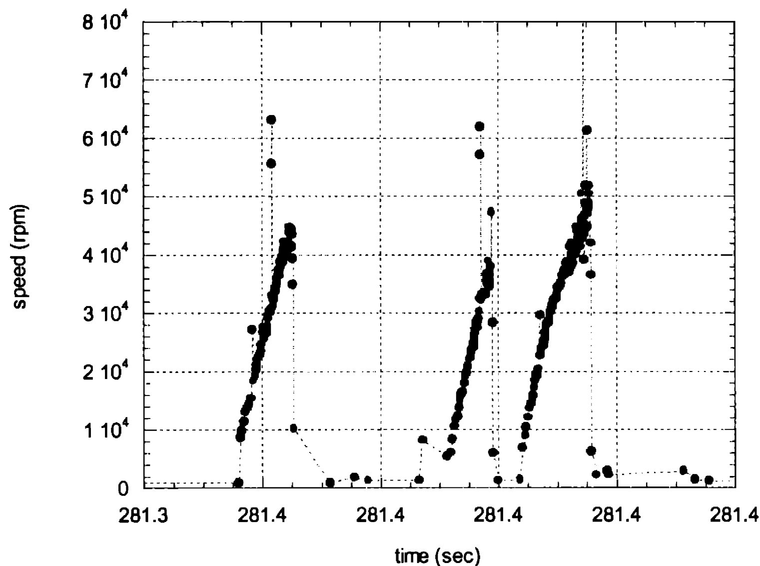


(b)

**Figure 6-2 Hydrostatic testing results. The rotor spins 4 times and is captured by the frequency-to-voltage converter as spikes in (a). Due to the quick crash, the F/V speed conversion is inaccurate. The speed is calculated by post-processing the pulse data and speed variation in the fourth spike is re-plotted in (b). The rotor accelerates three times, reaching 40,000 rpm before each crash.**

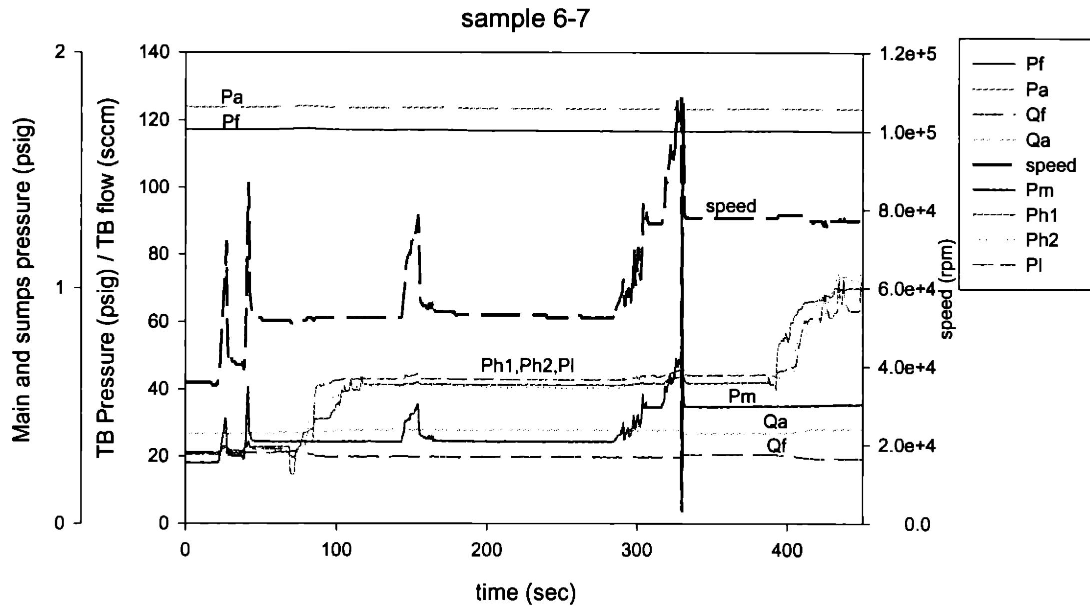


**Figure 6-3 Hydrostatic speed run of sample 6-7, the rotor accelerates to 110,000 rpm in this run, with the speed be proportional to the main pressure. The maximum main pressure only reaches 0.8 psi and the thrust bearing balance is unaffected at this pressure as shown by a steady flow rate. (courtesy of S. Jacobson) Pm, Ph1,Ph2, and Pl stand respectively for main pressure, high sump 1 pressure, high sump 2 pressure, and low sump pressure. Philtec sensor is used to measure speed in this test.**

The main turbine pressure-speed relationship has been consistent across several dies from build 6 (Figure 6-4). The input power scales with turbine pressure. Since the main dissipation mechanism of the micro-bearing rig is the drag in the bearings and the input power equals dissipation at a constant speed, the linear pressure-speed relationship suggest constant bearing loss in these tests.

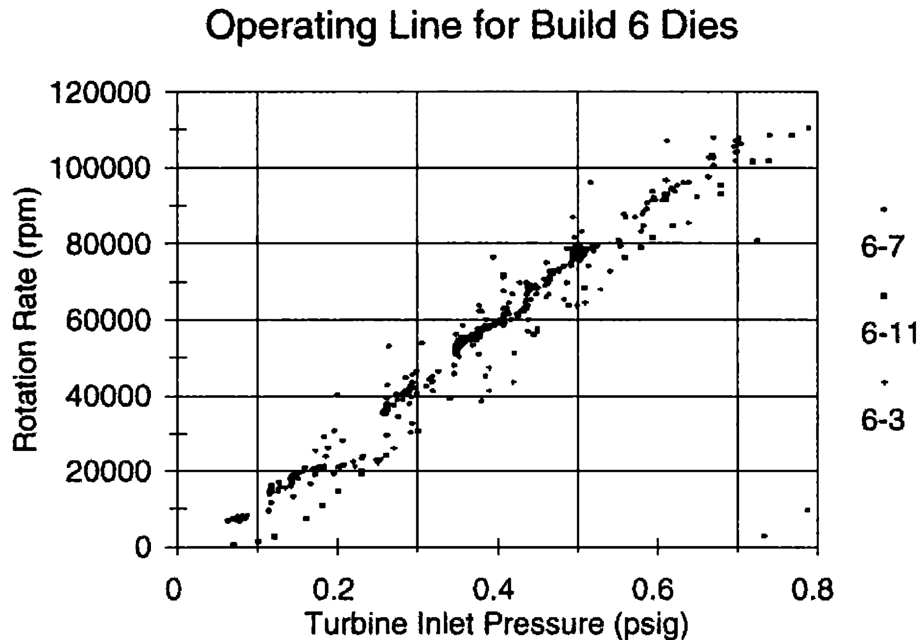


**Figure 6-4 Main pressure - speed relationships for build 6 dies. (Courtesy of S. Jocobson)**

### *Section 6.3 Hydrodynamic testing results*

Calculations by Piekos indicate that a hydrodynamic journal bearing provides higher stiffness at high speed than does a hydrostatic journal bearing. [4] As a result, early design efforts have been focused on a hydrodynamic bearing. The hydrodynamic bearing requires a side load for stabilization. For the micro bearing rig, there are several methods to introduce the side loading and each method has different implications for the axial balance.

Figure 6-5 shows an operating map (created by S. Jacobson [5]) for testing the micro bearing rig in hydrodynamic modes. The bearing number, along the horizontal axis, is a measure of rotation speed, while the load parameter (along the vertical axis) is a measure of the radial load supported by the bearing. Contours of eccentricity generated from a Reynolds equation solver (by Piekos) are shown. The plot also shows a thick gray line separating the stable and unstable operating regime for the journal bearing.

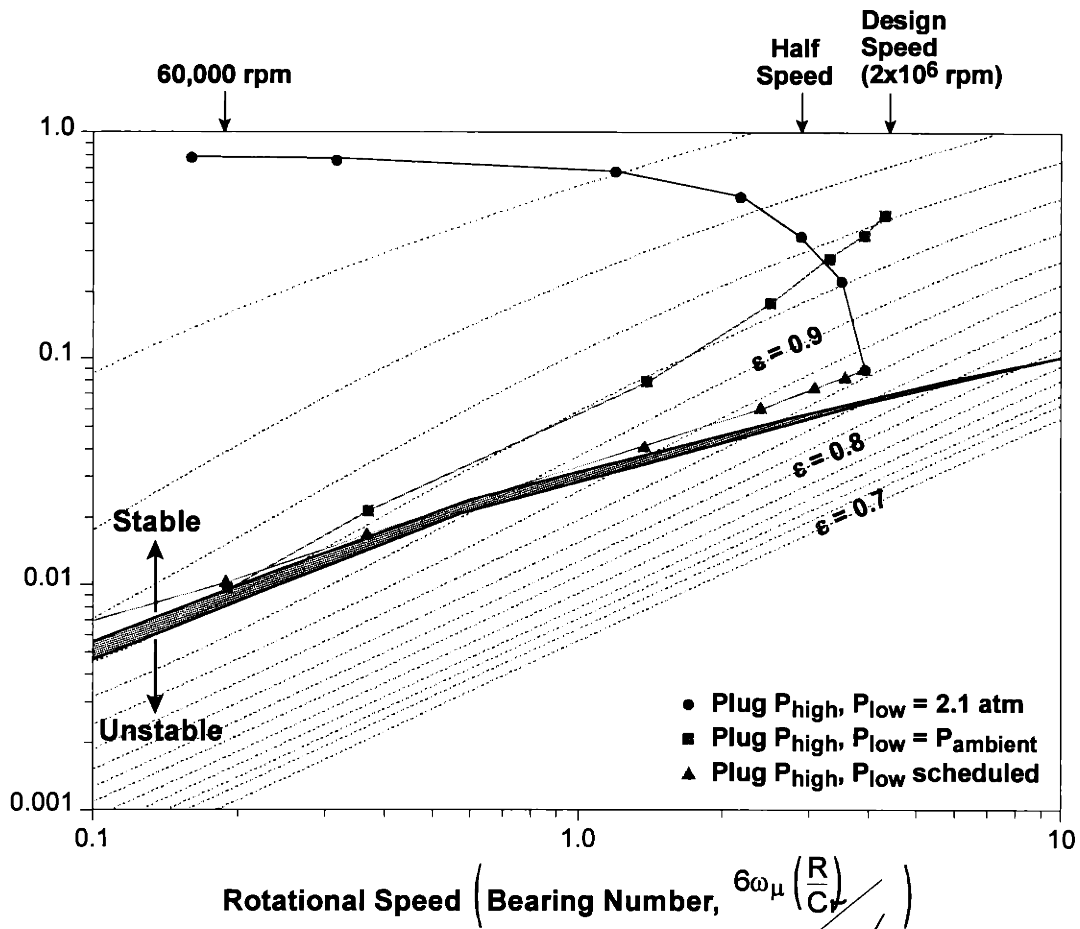


**Figure 6-5 Operating map for different hydrodynamic testing modes. The thick gray line is the calculated stability boundary. Dashed line is the constant eccentricity contour. Three methods of plumbing the sumps are shown. Each method has different threshold speed. The plug hi sump-vent low sump scheme (squares) is a simple method to get both low threshold speed (the speed at which the operating line crosses the stability boundary) and low eccentricity. (Courtesy of S. Jacobson and E. Piekos)**

Three operating lines are shown on the operating map. The circles represent a mode in which we plug the external connection to the high sumps (so their pressures are set by the fluid from the turbine inter-row station leaking through the journal bearing) and supply the low pressure sump with 2.1 atm (maximum turbine pressure). This approach sets a high side load at low speed, which can exceed the load capability of the journal bearing and thus pin the rotor at the wall. While this operating line locates the bearing in a favorable eccentricity at high speed. Another mode that can be easily implemented is shown by the squares in which we plug the two high pressure sumps such that their pressures are about equal to the turbine inter-row pressure, and vent the low pressure sump to ambient. As shown in Figure 6-5, this scheme is optimal to obtain a low threshold speed (the speed at which the operating line crosses the stability boundary),

which is about 5% of design speed. Moreover, it also introduces a lower axial unbalanced force (~0.1 N at full speed as compared to 0.3 N in the previous case). During the early tests, this is the most frequently used testing method. The drawback of this approach is that the increasing side load will push the rotor to a high eccentricity (~94%) at design speed. The third operating line in the figure (triangles) tailors the pressure applied to the low sump to provide a near optimal operating boundary, just skirting the stability line. The implementation of such an operating line is still under investigation.

The rig ran to higher speed before crashing and continuously rotate when configured to run in hydrodynamic mode in early tests. Since the thrust bearings were not optimized and had low load capacity, this is possibly related to the lower axial unbalance force associated with this mode. Without optimized thrust bearings, a large axial force can bottom the rotor on to a thrust bearing and prevent the rotor from spinning.

With the chosen hydrodynamic protocol (plug the high sumps and vent the low sump), the bearing is predicted to be unstable before reaching 5% of the design speed. The goal is to accelerate past the 5% stability threshold so quickly that the instability does not have sufficient time to crash the bearing. We chose to accomplish by ramping up the pressure quickly during starting. A continuous rotation mode was established for many devices in this way, with speeds of up to 80,000 rpm. The longest run has lasted for more than 10 minutes until the main pressure is turned-off by the author. The spin motion during this run was not stable, although the rotor never come to a full stop. The rotor underwent many acceleration/crash cycles as shown in Figure 6-6. The longest stable operation lasted about 0.5 seconds (about 500 revolutions) at 70,000 rpm as shown in Figure 6-7.

Our recent success with hydrostatic operation suggests that we applied too much pressure to start the rotor in our previous attempts. Since the friction force is too large to overcome, it makes better sense to find a method to start the rotor in the hydrostatic mode and switch to the hydrodynamic mode once reaching higher speeds. Most recent test (by Jacobson) has demonstrated a stable operation at 296,000 rpm by switching between hydrostatic and hydrodynamic mode.

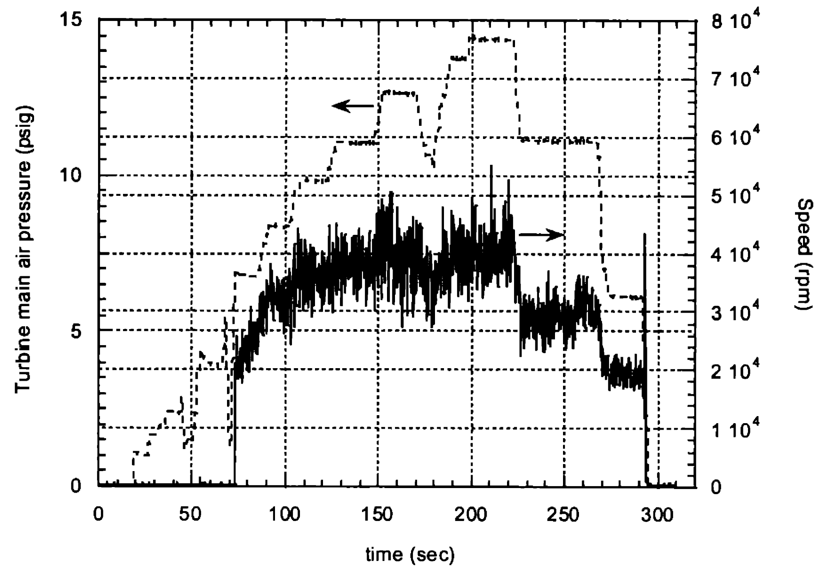


(a)

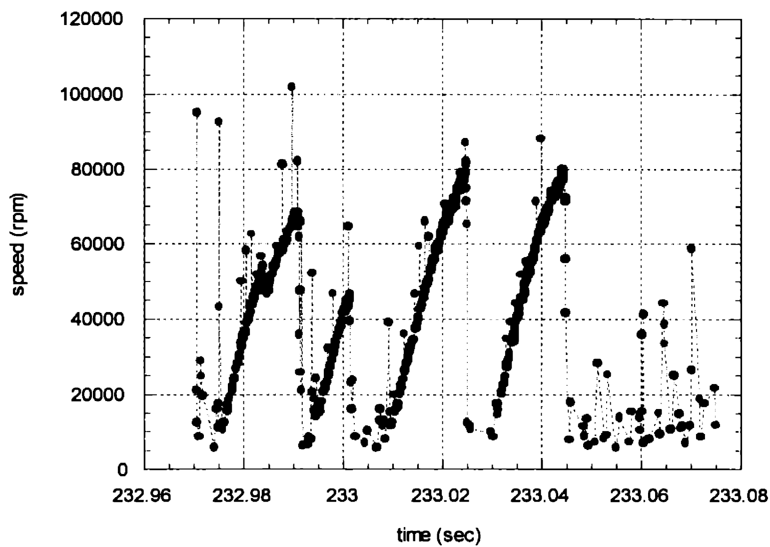


(b)

**Figure 6-6 (a) Hydrodynamic test result, the speed data is estimated by a frequency to voltage converter. (b) Close-up view showing the speed from post-processing stored blade-pass data. It shows the acceleration-crash cycles often seen in the early hydrodynamic tests.**

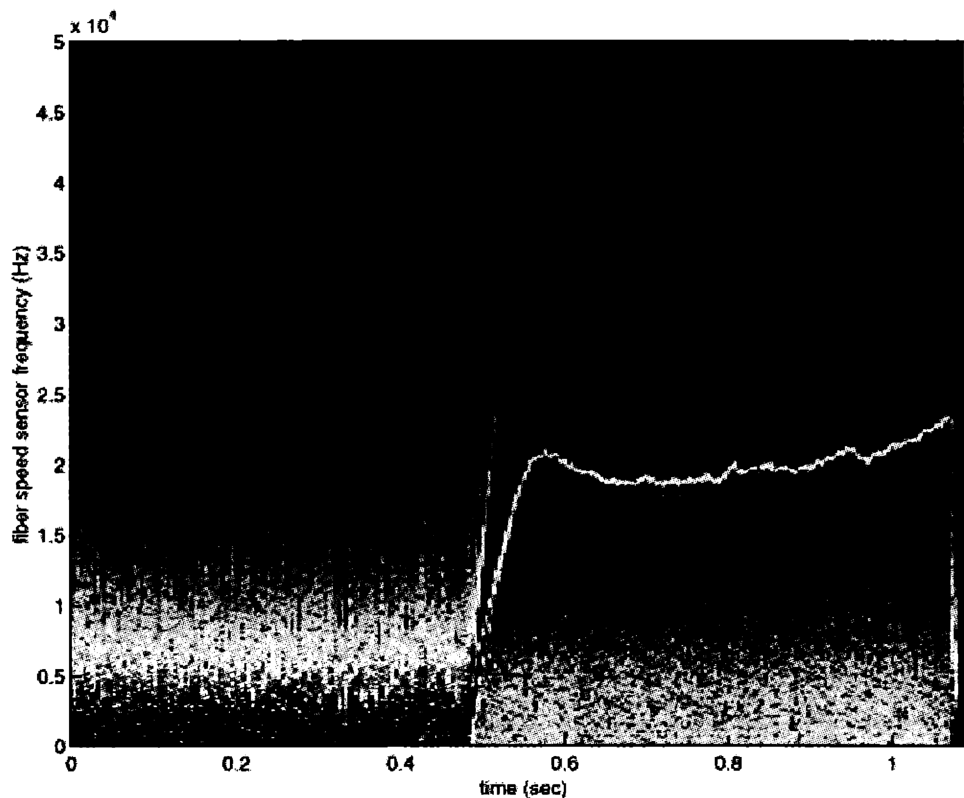


**Figure 6-7 Spectrum of speed sensor pulses (blade count). Maximum speed is about 70,000 rpm. To get the speed in rpm, we need to multiplying the blade count by 3 (there are 20 blades on the rotor).**

### *Section 6.4 Summary*

It appears that there is a strong link between the device fabrication accuracy and its performance. We have established a stable bearing operation that allow us to further explore the rotor-dynamics of micro air bearings. As of this writing, design speed (2.4 million rpm) has yet to be reached. Testing is underway to leverage improved fabrication accuracy and seek methods to further raise the bearing performance.

A new rig was designed by Frechette, incorporating new features that will improve the rotor axial thrust balance, and a new sump design that allows application of higher side load. It has so far demonstrated 500,000 rpm operation.

### *Section 6.5 Reference:*

[1] Orr, D.J. "Macro-scale investigation of high-speed gas bearings for MEMS devices." Ph.D thesis, MIT, 1999.

[2] Breuer, K., private communication, 1999.

[3] Jacobson, S., Protz, J., private communication, 1999.

[4] Piekos, E., " Numerical modeling of gas-lubricated journal bearing for micro fabricated turbomachines," Ph.D Thesis, MIT, 1999.

[5] Epstein, et. al., "The MIT microengine project – annual technical report," 1998.

# Chapter 7

# Conclusion

### *Section 7.1 Thesis contributions*

This thesis describes the development of a turbine-driven micro air-bearing rig. The contributions of this thesis include:

1. *Established a novel fabrication process to build a micro-fabricated rotating machine – the micro bearing rig.*

We use 5-wafer fusion bond and 9 DRIE steps to build the 3-dimensional structure. As this program evolved, needed equipment was acquired and many processing protocols were established. These established processes have become the backbone of many other processes used to build devices such as the micro motor-compressor and the micro demo engine. And this process architecture can be extended to build even more complicated MEMS devices.

2. *Established an instrumentation system and packaging scheme for the micro bearing rig testing.*

With a die size of 1.5 $cm^2$, the packaging includes 13 fluidic connections which operate up to 125 psig. The testing system provides all required pressure control and pressure/flow measurements in addition to the turbine speed measurement. This setup is now being used for testing of the new micro motor-compressor rig.

3. *Characterized the performance of the micro-thrust bearings and correlated first order results to device critical dimension.*

A set of flow measurement was undertaken for two purposes. First, these tests helped to deduce the internal dimensions of this complicated device non-destructively. Second, these tests provided experimental data to evaluate both a semi-empirical model and a CFD model for the thrust bearings. The model was then used to refine the rig design and to infer performance parameters that could not be directly obtained experimentally.

*4. Demonstrated stable operation of the micro bearing rig.*

A stable air bearing operating speed of 296,000 rpm was achieved with the devices designed as part of this thesis. We have greatly enhanced our knowledge of building high tolerance micro parts as part of a very complicated fabrication process, a key for successful micro rig operation. While only 12.5% of the final goal, tests running at this operating speed still provide much information about the rotor-dynamics of micro fabricated air bearings. Future devices should benefit from the knowledge gained through this thesis, allowing them to push the speed boundary to much higher levels.

## Section 7.2 Lessons learned

We learned several important lessons in the course of this thesis. First, a detailed system interaction check is the key to building a complicated device successfully; attention has to be paid to every part of the device. In our case, we only worried about journal bearing stability and neglected the thrust bearing design. This became a serious problem at the end because the side loading scheme used could produce strong axial loading and bottom the rotor to crash on to the thrust bearings.

The second lesson learned is the importance of adequate geometric specification. Due to the novelty of the process and the lack of previous work in this field, we did not know the necessary tolerances for the device. The idea was to establish a baseline process and improve the geometrical accuracy as much as we could. We found that the performance of the micro bearing rig scales with its dimensional accuracy. With the combined efforts of fabrication, design improvement, and testing, we have built devices that have tighter tolerances and work at hundreds of thousands of rpm. With a few more iterations, we shall establish the world's first database of micro bearing geometrical specifications.

Third, the rotor start-up features should be included in the design. It is very easy for a 4 mm diameter rotor to move a few microns and lean on the wall. Strong hydrostatic thrust bearings can float the rotor axially, but the rotor can be pinned to the journal wall unless a hydrostatic journal bearing is built. External sources can be used in the development phase, but the final device will need to include a feature to free the rotor at the beginning.

### *Section 7.3 Future work*

There are several issues that require further attention. In the fabrication area, the project will benefit from continuing endeavors to establish a deep-RIE process that can produce a taper-free, smooth, high-aspect-ratio silicon trench. When used to etch the journal bearing, the elimination of tapering will improve stiffness, and the improvement in surface quality will reduce particle generation and fracture probability. We also need to establish better wafer-to-wafer gap control for multiple-wafer fusion-bonding. Because thrust bearing gaps are defined by the fusion bonding, their design will benefit from an increased understanding of the fabrication tolerances.

We can also improve the instrumentation further, particularly position sensors. Since successful integration of rotor position sensors is essential for studying the rotor dynamics, it has been difficult to extrapolate information about the rotor operation. There is ongoing work focusing on this subject, and we shall soon see the merging of this sensor with the bearing rig.

Several other bearing designs were proposed in case we found major obstacles in increasing the speed. Spiral hydrodynamic thrust bearings have been designed and fabricated and are ready to replace the hydrostatic ones at any time. Wave journal bearings that can suppress whirl and reduce the required side load have also been designed. The fabrication processes for these is being developed. We are also considering hybrid journal bearings that are easy to operate at either spin-up or high-speed.

# Appendices

## *A. Process Flow*

### Prototype process flow

From October in 1995, a first-phase program was started to build a silicon based micro turbine prototype. The function of this project is multi-purposed:

1. To analyze the capability of STS ICP etcher.
2. To identify potential fabrication problems and new techniques.
3. To obtain experimental data of micro turbine performance to evaluate the design codes.
4. To verify/find a working bearing design.
5. To establish the instrumentation.

The process flow for the prototype is shown below.

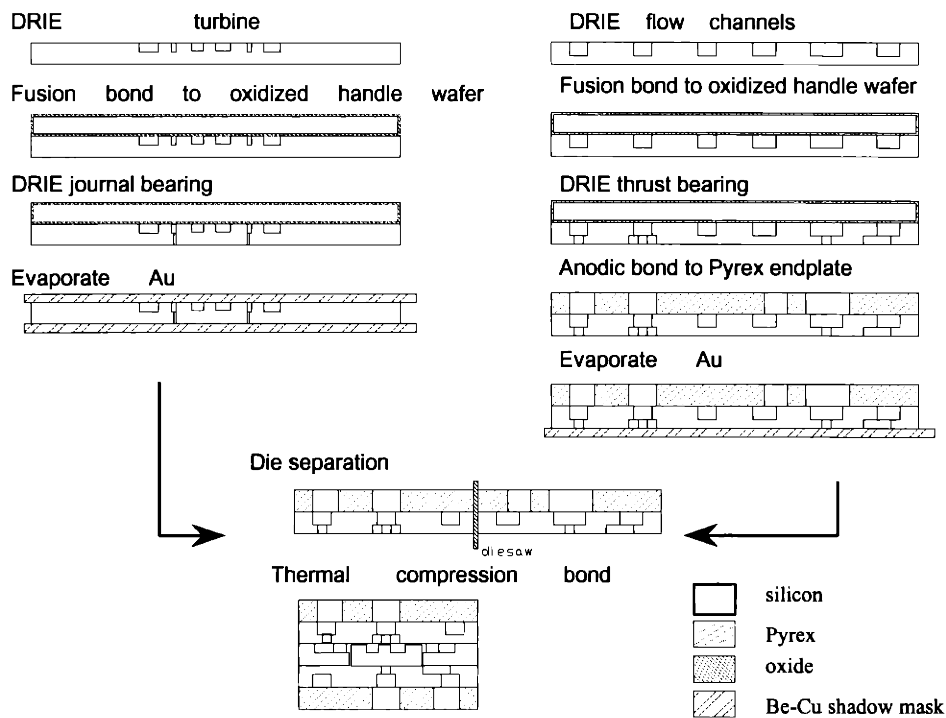

The detailed process steps are listed as follows:

Starting material for each 5 wafer stacks:

500 um thickness, double-side polished 4" silicon wafer*2,
500 um thickness, single polished 4" silicon wafer*2,
500 um thickness, 4" pyrex wafer*1.

**Turbine Wafer:**

1. HMDS on double-polished silicon device wafer.
2. Double coat standard resist/prebake
3. Pattern triangle rotor edge marks for speed/position sensor. (MASK 1)
4. Postbake 30mins. (120C)
5. Chlorine etch (ICL etcher 3)
6. Ashing (ICL asher)
7. HMDS.
8. Spin coat AZ 4620 (1750rpm*8sec/3000rpm*60sec/7000rpm*3sec).
9. Prebake 60 mins.
10. IR aligned contact patterning turbine blades: ks1 for 5 sec. (MASK 2)
11. Develop /postbake at 90C for 10 mins
12. Coat wafer backside with 1um standard photoresist.
13. Postbake another 20mins at 90C.
14. 3 mins descum in old ICL asher.
15. DRIE turbine (STS 1672): time etch to 200um.
16. Piranha clean strip resist.
17. Oxygen plasma ashing
18. RCA clean single polished (SP) silicon handle wafer.
19. Grow 1micron thermal oxide on handle wafer.
20. HMDS / coat standard resist (1um).
21. Pattern channels. (MASK 3)
22. BOE etch oxide to define channles
23. Piranha clean photo-resist.
24. RCA clean turbine wafer and oxidized handle wafer
25. Contact device and handle wafer in normal ambient: annealed at 800C for 30mins.
26. HMDS/ coat AZ 4620 on backside of turbine wafer. (1500rpm*60sec)
27. Prebake 60 mins.
28. Contact patterning journal bearing (4um mask)
29. Postbake 30mins at 90C.
30. Journal bearing etch (STS 1715): time etch till reach turbine (~300um).
31. Piranha clean.
32. HF handle wafer release etch/ pick up rotors.
33. Attach shadow masks on both sides with UV epoxy.
34. E-beam evaporate Au/Ti (5000A/200A) on both sides.
35. Remove the shadow mask with Acetone/ultrasound.
36. Resist bond to a dummy single-polished wafer.
37. Cover surface with standard resist, prebake.
38. Die separation.

**Endplate Wafer:**

39. HMDS on another double-polished wafer.
40. Coat standard resist (1um).
41. Pattern thrust bearing gap. (MASK 4)
42. Develop and postbake.
43. Plasma etch 1um (ICL etcher 1 recipe 19)
44. Ashing.
45. HMDS
46. Double coat standard resist.
47. Pattern tip clearance and generator gap. (MASK 5)
48. Develop and postbake.
49. Plasma etch 4.5um (ICL etcher 1 recipe 19)
50. Ashing.
51. HMDS
52. Coat AZ4620.
53. Prebake 60mins.
54. IR alignment and expose flow channels (MASK 6)
55. Develop and postbake.
56. Deep etch (STS 1672) to 400um.
57. Piranha strip resist.
58. RCA clean with patterned handle wafer
59. Contact device and handle wafer and anneal at 800C for 30mins.
60. HMDS
61. Coat AZ4620.
62. Prebake 60mins.
63. Contact patterning bearing restrictors. (MASK 7)
64. Develop/postbake.
65. Deep etch until through-wafer (~100um). (STS 1715)
66. Piranha strip resist.
67. HF release handle wafer (24 hours).
68. Piranha clean.
69. Ultrasonic drill pyrex wafers. (out-sourced) (MASK 8)
70. Aligned pyrex wafer with silicon wafer using ks1, fix with UV epoxy.
71. Anodic bonding (400C, 400V): 2 minutes.
72. Attach shadow mask on silicon side.
73. Evaporate Au/Ti.
74. Remove shadow mask.
75. Protect surface with standard resist, prebake.
76. Die separation.
77. Post diesaw clean on both pyrex/silicon die and turbine die: Ultrasonic/Acetone*2, Ultrasonic/methanol*2, Ultrasonic /DI*2, UV ozone 20mins.
78. Thermal compression bond 3 stacks (2+1+2) together.

| Recipe # | SF6 flow (sccm) | SF6 time (sec) | SF6 overlap (sec) | C4F8 flow (sccm) | C4F8 time (sec) | C4F8 overlap (sec) | APC angle | Etch platen power | Pass platen power |
|---|---|---|---|---|---|---|---|---|---|
| 1672 | 130 | 12 | 1 | 30 | 7 | 1 | 65 | 9 W | 5 W |
| 1715 | 80 | 12 | 0 | 52 | 7 | 0.5 | 70 | 12 W | 5 W |

**Table 6 Recipies provided by STS with STS ICP etcher.**

| Recipe | Power | SF6 | CCl4 | He | Pressure |
|---|---|---|---|---|---|
| 19 | 50W | 95 sccm | 3 sccm | 120 sccm | 500mTorr |

**Table 7 Recipes for Lam 480 Plasma Etcher (ICL etcher-1)**

| Recipe | Tube | Dry oxide | Wet oxide | Thickness |
|---|---|---|---|---|
| 224 | A3 | 10 mins | 140 mins | 1um |

**Table 8 Thermal oxide process (for handle wafer)**

During fabrication and testing, we discovered several problems, including,

1. Low yield caused excessive wafer handling related to die-level thermal compression bonding.
2. Inter-wafer gap control issue.
3. Pressure source sharing between main air and forward thrust bearing.
4. Packaging leakage.

These issues motivate a redesign of the process to build an improved device as mentioned in chapter 3. The detailed process steps are explained in the next section.

## Full wafer level process steps:

Starting material for each 5 stacks: 450 um thickness, double-side polished 4" silicon wafer*4
500 um thickness, double-side polished 4" silicon wafer*1
500 um, 4" Quartz wafer *2.

**Define global alignment marks:**

1. HMDS all silicon wafers.
2. Resist coat all silicon wafers.
3. Prebake.
4. Contact expose global alignment marks. (MASK1)
5. Develop and postbake.
6. Plasma etch 0.5-1.0 um. (etcher-1, recipe 19)
7. Strip resist.
8. HMDS.
9. Coat resist on back side of all wafers.
10. Prebake.
11. Contact expose back side global alignment marks. (MASK2)
12. Develop and postbake.
13. Plasma etch 0.5-1.0 um. (etcher-1 recipe 19)
14. Strip resist.

**Forward endplate (FEP) process:**

15. HMDS on a 450um wafer.
16. Coat standard resist, prebake.
17. Contact pattern thrust bearing gaps. (MASK 3)
18. Develop and postbake.
19. Silicon plasma etch (AME 5000).
20. Strip resist.
21. Double coat standard resist, prebake.
22. Contact pattern tip clearance. (MASK 4)
23. Develop and postbake.
24. Silicon plasma etch (AME 5000).
25. Strip resist.
26. HMDS.
27. Coat AZ4620. Spin: 3000rpm/60 sec.
28. Prebake 60 minutes.
29. Contact pattern flow channels on back side. (MASK 5)
30. Deep RIE with STS ICP (Recipe: MIT 52).
31. Piranha clean.
32. Ashing.
33. Deposite PECVD sacrificial oxide on deep etched side. (Novellus or Oxford): 100 nm.
34. Densify PECVD oxide, 1000C for 1 hour in $N_2$.
35. HMDS.
36. Photoresist bond silicon wafer to quartz wafer.
37. Coat AZ4620. (spin: 3000rpm/60sec).
38. Prebake 60minutes.
39. Contact expose thrust bearing nozzles. (MASK 6)

40. Develop/ postbake.
41. Deep RIE with STS ICP (Recipe: MIT 59).
42. Piranha clean/handle wafer separation.
43. Acetone rinse.
44. BOE strip sacrificial oxide
45. Piranha clean.
46. Ashing.

**Turbine rotor plate (RP) process:**

47. HMDS the 500um thickness silicon wafer.
48. Coat AZ4620 (spin: 3000rpm/60sec).
49. Prebake 60minutes.
50. Contact expose turbine blades. (MASK 7)
51. Deep RIE (MIT 69)
52. Piranha clean.
53. Ashing.

**FEP/RP pair process:**

54. RCA clean both wafers.
55. Aligned fusion bonding (EV450 aligner and AB1-PV bonder).
56. Post-bonding anneal. (1100 C, 30 minutes)
57. HMDS.
58. Resist bond quartz handle wafer.
59. Coat AZ 4620.
60. Prebake 60 minutes.
61. Contact expose journal bearing. (MASK 8)
62. Deep RIE (MIT 56)
63. Piranha resist clean/ handle wafer release.
64. Acetone rinse.
65. Ashing.

**Forward foundation process:**

66. HMDS.
67. Resist bond to quartz handle wafer.
68. Coat AZ 4620 (spin: 1000rpm/60sec)
69. Prebake 60 minutes.
70. Contact expose flow passages. (MASK 9)
71. Deep RIE (MIT 59).
72. Piranha clean/handle wafer separation.
73. Acetone rinse.
74. Ashing.

**Aft endplate (AEP) process:**

75. HMDS on a 450um wafer.
76. Coat standard resist, prebake.
77. Contact pattern thrust bearing gaps. (MASK 10)
78. Develop and postbake.
79. Silicon plasma etch (AME 5000).
80. Strip resist.
81. Double coat standard resist, prebake.

82. Contact pattern generator gap. (MASK 11)
83. Develop and postbake.
84. Silicon plasma etch (AME 5000).
85. Strip resist.
86. HMDS.
87. Coat AZ4620. Spin: 3000rpm/60 sec.
88. Prebake 60 minutes.
89. Contact pattern flow channels on back side. (MASK 12)
90. Deep RIE with STS ICP (Recipe: MIT 52).
91. Piranha clean.
92. Ashing.
93. Deposite PECVD sacrificial oxide on deep etched side. (Novellus or Oxford): 100 nm.
94. Densify PECVD oxide, 1000C for 1 hour in $N_2$.
95. HMDS.
96. Photoresist bond silicon wafer to quartz wafer.
97. Coat AZ4620. (spin: 3000rpm/60sec).
98. Prebake 60minutes.
99. Contact expose thrust bearing nozzles. (MASK 13)
100. Develop/ postbake.
101. Deep RIE with STS ICP (Recipe: MIT 59).
102. Piranha clean/handle wafer separation.
103. Acetone rinse.
104. BOE strip sacrificial oxide
105. Piranha clean.
106. Ashing.

**Aft foundation plate (AFP) process:**

107. HMDS a 450um wafer.
108. Coat AZ4620. Spin: 3000rpm/60 sec.
109. Prebake 60 minutes.
110. Contact pattern contact ports on back side. (MASK 14)
111. Deep RIE with STS ICP (Recipe: MIT 52, depth: 100 um).
112. Piranha clean.
113. Ashing.
114. HMDS.
115. Photoresist bond silicon wafer to quartz wafer.
116. Coat AZ4620. (spin: 3000rpm/60sec).
117. Prebake 60minutes.
118. Contact expose flow channels-2. (MASK 15)
119. Develop/ postbake.
120. Deep RIE with STS ICP (Recipe: MIT 52, depth: 350um).
121. Piranha clean/handle wafer separation.
122. Acetone rinse.
123. Piranha clean.
124. Ashing.

**Bonding process:**

125. RCA clean Aft endplate and aft foundation plate wafer.
126. Aligned fusion bond Aft endplate (AEP) and aft foundation plate (AFP) with EV450 aligner and AB1-PV bonder.
127. Post bonding anneal AEP/AFP (TRL tube B2, 1100C 30 minutes).

128. RCA clean Forward foundation plate, bonded RP/FEP wafers, bonded AEP/AFP wafers.
129. Aligned fusion bond FEP/RP to AEP/AFP, then to FFP with EV450 aligner and AB1-PV bonder.
130. Post bonding anneal (TRL tube B2, 1100C 30 minutes).
131. Die separation.
132. Pre-laser HF etch (1:1 HF/DI mixture, 20 minutes).
133. O2 plasma clean (Plasma-quest ECR).
134. Laser assisted sacrificial tab etch.

| Power | $SF_6$ | $CCl_4$ | He | pressure |
|---|---|---|---|---|
| 50 W | 95 sccm | 3 sccm | 120 sccm | 500 mtorr |

**Table 9 Lam 480 (etcher-1) recipe 19.**

| Step | Power (W) | Mag field (Gauss) | Pressure (mTorr) | Time (sec) | $O_2$ (sccm) | $Cl_2$ (sccm) | HBr (sccm) | $NF_3$ (sccm) |
|---|---|---|---|---|---|---|---|---|
| 1 | 0 | 60 | 100 | 25 | 15 | | | |
| 2 | 100 | 60 | 100 | 15 | 15 | | | |
| 3 | 0 | 50 | 200 | 15 | | 20 | 20 | 10 |
| 4 | 350 | 50 | 200 | set | | 20 | 20 | 10 |

**Table 10 AME 5000 (magnetron) shallow plasma etching parameters.**

| $SiH_4$ | $N_2$ | N2O | Power | Pressure | Temperature | Deposition rate |
|---|---|---|---|---|---|---|
| 0.3 SLPM | 1.5 SLPM | 9.5 SLPM | 1.1 kW | 2.6 Torr | 400 C | 5350 A/min |

**Table 11 Novellus sacrificial oxide recipe.**

| $SiH_4$ | N2O | Pressure | Power | Deposition rate |
|---|---|---|---|---|
| 17% | 6% | 80 mTorr | 25W | 395 A/min |

**Table 12 Oxford sacrificial oxide recipe**

| Recipe # | $SF_6$ flow (sccm) | $SF_6$ time (sec) | $SF_6$ overlap (sec) | $C_4F_8$ flow (sccm) | $C_4F_8$ time (sec) | APC angle | Etch coil power | Etch platen power | Pass platen power |
|---|---|---|---|---|---|---|---|---|---|
| 52 | 105 | 14 | 0.5 | 40 | 11 | 65 | 600 | 12 | 6 |
| 56 | 105 | 14 | 0.5 | 40 | 11 | 65 | 800 | 12 | 6 |
| 59 | 105 | 14 | 0.5 | 40 | 11 | 65 | 750 | 12 | 6 |
| 69 | 105 | 14 | 0.5 | 40 | 11 | 65 | 750 | 10 | 6 |

**Table 13 Recipies developed at MIT to be used for deep etching.**

| Step | Description |
|---|---|
| 1 | Pour resist to cover 2/3 of the wafer surface |
| 2 | 1750 rpm, 7 seconds |
| 3 | 1000-3000 rpm (6-10 μm), 60 seconds |
| 4 | 7000 rpm, 3 seconds. |

**Table 14 Thick resist (AZ4620) spin process**

| RF Power | Microwave Power | O2 | Pressure | Time |
|---|---|---|---|---|
| 50 W | 400 W | 30 sccm | 5 mTorr | 5 minutes |

**Table 15 Plasma-quest pre-LAE clean**

### *B. Packaging Design*

First generation packaging design is shown below. Both the top and bottom plates are machined out of PMMA (plexiglass). The top plate has a optional exhaust on the left for measuring exhaust flow rate and pressure. The right port bring in air for the turbine and forward thrust bearing. A recess is cut into the bottom plate to hold the die (1cm$^2$) Fluidic port to the high sump, aft thrust bearing, low sump and aft exhaust are drilled from the sides of the plates. Four bolts hold the package together.

This design suffers cross leakage between ports because it relies on unrelieable direct contact between package and silicon die for sealing. However, we were able to demonstrate the spin capability using this simple package.

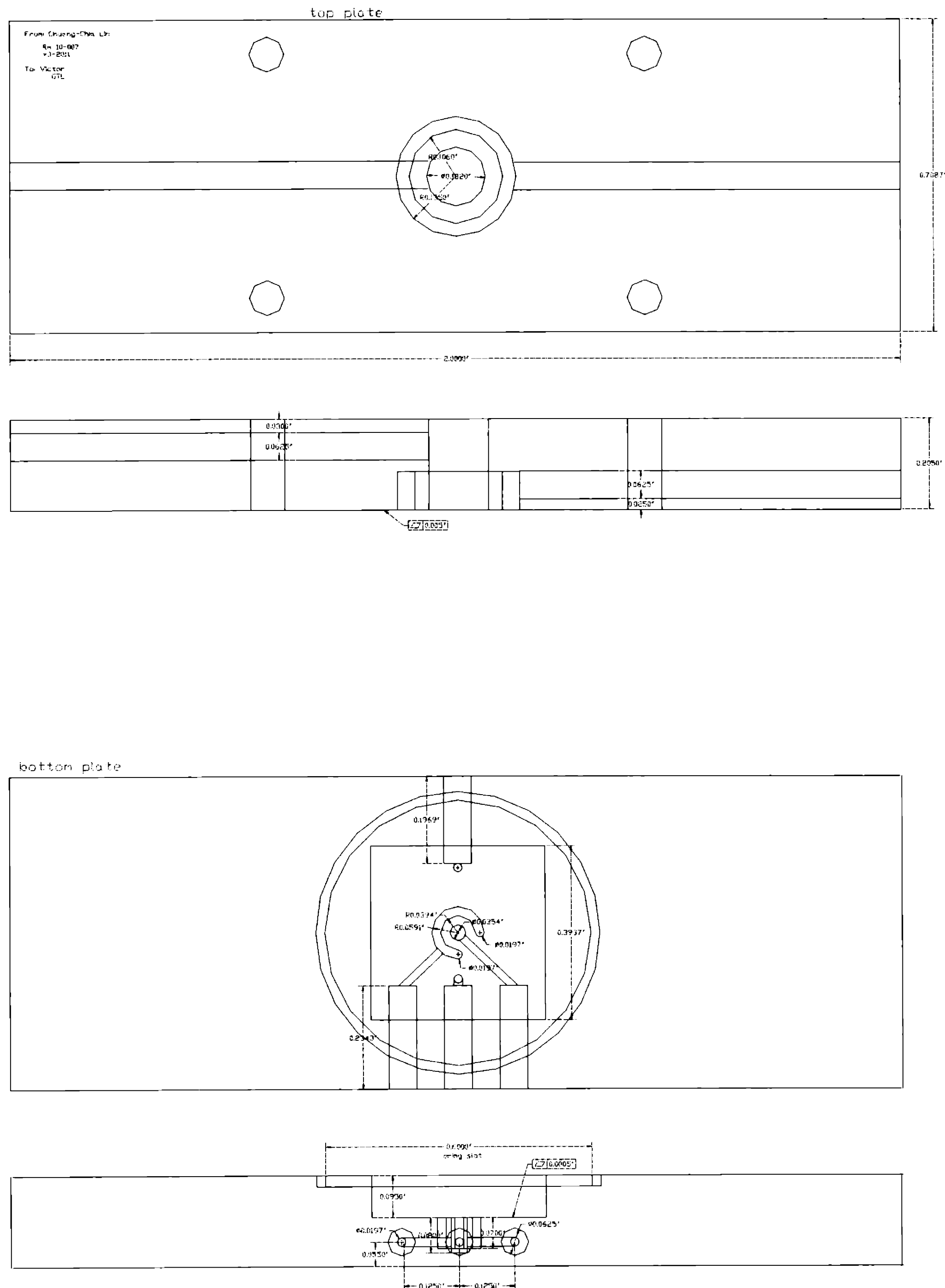


**Figure 8-1 First packaging design for prototype testing.**

The redesigned three-piece package is shown in the following pictures. The top and bottom plates are made of Plexiglas (PMMA). Stainless steel tubes are glued to the side ports using 3-minutes epoxy. O-rings and latex rubber gaskets are used to for proper sealing.

**Figure 8-2 Top cover plate**

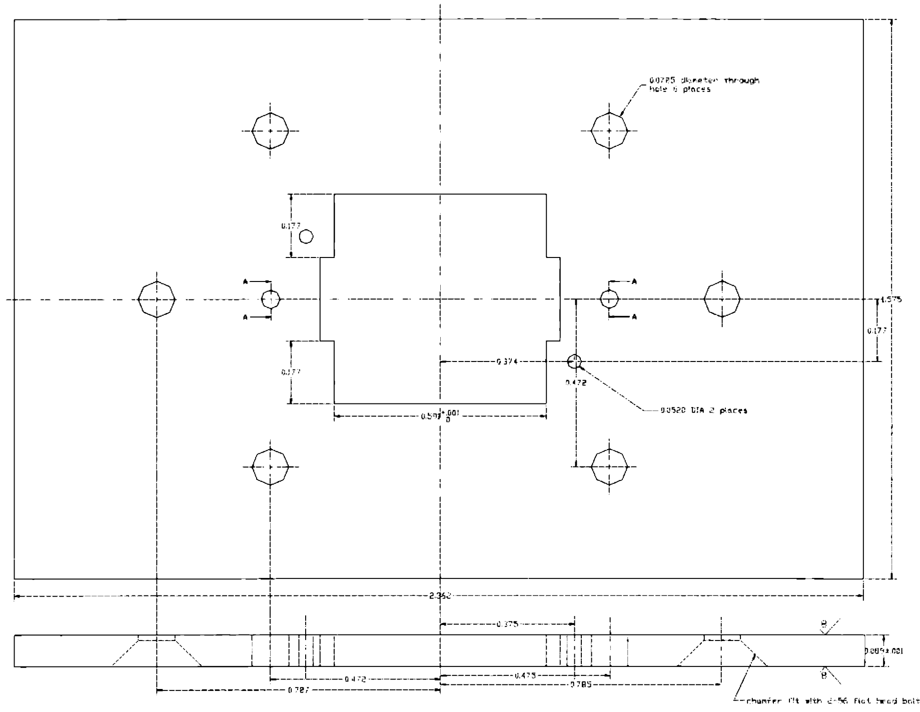


**Figure 8-3 middle plate**

**Figure 8-4 Bottom plate.**

### *C. Baseline thrust bearing model*

This model is developed by S. Jacobson to help with the design purpose. It includes three serial flow resistances: the capillary resistance $R_{cap}$, the inherent resistance $R_{inh}$, and the radial outflow resistance $R_{rad}$, to fully characterize the total flow resistance in the bearing. The pressure drop through each of the resistance is the product of the flow rate to the resistance:

$$\Delta P = R\,\dot{m}\,, \tag{8-1}$$

where $\dot{m}$ is the mass flow rate, and $R$ represent any flow resistance. Because the mass flow rate is the same for all three flow resistance, an initial mass flow rate was assumed and pressure drop through each resistance was calculated based on this flow. The flow rate is adjusted according to the calculated total pressure drop. The calculations keep iterating until the total pressure drop matches the specified pressure difference. After convergence, the pressure across each of the flow resistance is obtained and the bearing force is calculated accordingly.

The capillary restriction pressure loss is incorporated into the model based on empirical loss coefficient published in a handbook. [1], and expressed in terms of the product of dynamic pressure and loss coefficient:

$$\Delta p_{cap} = R_{cap}\,\dot{m} = \xi\left(\tfrac{1}{2}\rho_{cap}V_{cap}^{2}\right), \tag{8-2}$$

where $\rho$ and $V$ stand for density and velocity, and the subscript cap stands for the position (capillary) where $\rho$ and $V$ are calculated. The velocity is calculated based on the assumed mass flow rate. The loss coefficient $\xi$ is,

$$\xi = \begin{cases} \xi_{\phi} + \zeta(1.5+\tau) + \dfrac{f\,l}{D} & \mathrm{Re} < 2300 \\ 1.5 + \tau + \dfrac{f\,l}{D} & \mathrm{Re} > 2300 \end{cases} \tag{8-3}$$

where

$$\begin{aligned} \xi_{\phi} &= 3.29 - 1.62x + 0.22x^{2} \\ \zeta &= 0.46146 - 0.26486x + 0.20305x^{2} - 0.06602x^{3} + 0.01325x^{4} - 0.00105x^{5}, \\ x &= \log(\mathrm{Re}). \end{aligned} \tag{8-4}$$

And $l$ stands for the length of the restrictors, and $D$ is the diameter of the restrictors. And,

$$\tau = \begin{matrix} (2.4 - l/D)10^{-\phi} & l/D < 2.4 \\ 0 & l/D \geq 2.4 \end{matrix}$$
$$\phi = 0.25 + \frac{0.535(l/D)^8}{0.05 + (l/D)^7} \tag{8-5}$$

parameter $f$ is defined by,

$$f = \begin{matrix} 64/\mathrm{Re} & \mathrm{Re} < 2300 \\ 1.02(\log(\mathrm{Re}))^{-2.5} & \mathrm{Re} \geq 2300 \end{matrix} \tag{8-6}$$

where Re is the Reynolds number, Re in the capillary is defined by,

$$\mathrm{Re} = \frac{\rho_{cap} V_{cap} D}{\mu}, with$$
$$\mu(T) = 2.2 \times 10^{-5} \left( \frac{T}{373} \right)^{0.67} \tag{8-7}$$

where $T$ is temperature in Kelvin. There are two different models that are used for calculating the inherent restrictors, one based on experimental results by Mechanical Technology Incorporated [2], and the other purposed by Dr. Jacobson. Only the results of MTI model is used in this thesis. In the MTI model, the pressure loss is also expressed as a product of dynamic pressure and loss coefficient,

$$\Delta p_{inh} = K_{mti} \left( \tfrac{1}{2} \rho_{inh} V_{inh}^2 \right). \tag{8-8}$$

The velocity $V_{inh}$ is the averaged flow velocity after turning, calculate when divide $\dot{m}$ by $\pi D g$. And $K_{mti}$ is an empirical loss coefficient based on experimental results from Carfagno & McCabe [3] and Vohr [4].

$$K_{mti} = 0.179 + 0.31\left(\frac{\mathrm{Re}}{2000}\right) - 0.122\left(\frac{\mathrm{Re}}{2000}\right)^2 + 0.282\left(\frac{\mathrm{Re}}{2000}\right)^3 \quad (8\text{-}9)$$

The Reynolds number in this equation is the local Reynolds number at the exit of the capillary.

The radial outflow resistance is modeled by numerical integration of compressible axisymmetric radial flow assuming a uniform pressure exists at the radius where the restrictors are located. The solution for the pressure drop is,

$$\Delta P_{rad} = \sqrt{-\frac{12\mu RT\dot{m}}{g^3\pi \ln\left(\frac{r_o}{r_i}\right)}}, \quad (8\text{-}10)$$

where $g$ is the bearing gap, $r_o$ is the radius of bearing pad and $r_i$ is orifice location. Iterations that match the flow rate are performed in a spreadsheet program until the total pressure drop matches the specified pressure difference. The bearing loading capacity is obtained by integrating the pressure in between the pad. Stiffness is obtained by perturbing the bearing gap and calculating the ratio of force variation and displacement.

### *Reference*


[1] Idelchik, I.E., "Handbook of Hydraulic Resistance", 3rd ed., CRC Press 1994, p202.

[2] "Design of Gas Bearings", Mechanical Technology Incorporated, p 5.1.11.

[3] Carfagno, S. P. and McCabe, J.T., "Summary of Investigations of entrance Effects om Circular Thrust Bearings," Franklin Institute Research Laboratories Technical Report I-A2049-24.

[4] Vohr, J.H., "An Experimental Study of Flow Phenomena in the Feeding Region of an Externally Pressurized Gas Bearing," Paper presented at the ASME 1966 Spring Lubrication Symposium in New Orleans, LA, June 1966.